The Hong Kong Polytechnic University

Electrodeposition of Ni-SiC Composites by Different Shaped Current Waveforms and Magnetic Field

By

Hu Fei

A thesis submitted to The Hong Kong Polytechnic University in partial fulfillment of
the requirements for the Degree of Philosophy

Department of Industrial and Systems Engineering
The Hong Kong Polytechnic University

Hong Kong
December 2005

CERTIFICATE OF ORININALITY

I thereby declare that this thesis is my own work and that, to the best of my knowledge and belief, it reproduces neither materials previously published or written, nor materials that has been accepted for the award of any other degree or diploma, except where due acknowledgement has been made in the text.

____________________________ (Signed)

________HU Fei________ (Name of student)

Abstract

The electrolytic co-deposition of particles with metals has been a research topic for more than a decade since composite materials have many enhanced properties such as hardness and wear resistance relative to monolithic metals. There are many researchers to improve the deposit quality of electro-composites by adjusting the bath composition and using pulse current. However, there is a need to develop electro-composites with tailored properties and have a better understanding of the deposition behaviour. In the present study, two additional process variables, magnetic field and current waveforms are introduced to manipulate the microstructure and enhance the deposit quality of electro-composite, and their effect on the deposition mechanisms are examined.

The electro-codeposition behaviour of the Ni-SiC composite under different shaped waveforms is investigated. The amount of embedded SiC particles is shown to be related to the current waveforms and the average current density. The Guglielmi's model is extended to predict the volume fraction of SiC particles in the codeposition process under waveforms with arbitrary shape. It is found that the amount of SiC embedded in the nickel matrix is related to the peak current density of the waveforms. With the consideration of the influence of SiC particles on the free energy for creation of new interface and the growth of new grains, an analytical equation for average nucleation rates of the four waveforms is also derived, and the results are in consistence with the experimental findings.

Based on the electrochemical impedance spectra of the Ni-SiC electro-codeposition system, an equivalent circuit model (EC) is formulated to examine the charge transfer process and the double layer effect. It is shown that the use of a shaped waveform results in an improvement in morphology and hardness of the composites as compared with those obtained by direct current electrodeposition. Under the same average current densities, the highest instantaneous peak current for charge transfer is obtained under the ramp-up waveform, as compared to those obtained under triangular and ramp-down waveforms. The findings of the model are in agreement with the experimental results. The present study also applies the equivalent circuit model to explain the effect of duty cycle and frequency on deposition behaviour of composite in pulse electro-codeposition. The findings of the model are also in consistence with the experimental results.

The effect of magnetic field on surface morphology, SiC content and crystal orientation of the Ni-SiC electro-composite is further examined. It is found that the magnetic field modifies the surface morphology and the orientation of the composites, and significantly increases the SiC content. This phenomenon can be attributed to the change of charge transfer reactions and the mass transport process through the magnetohydrodynamic effect. The findings of the project are of significance in better understanding the electro-codeposition mechanisms and in improving the quality of electro-composites.

Acknowledgements

The candidate would like to express her sincere gratitude and appreciation to her chief supervisor, Prof. K.C. Chan, for his generous guidance, encouragement and invaluable advice during the research project. The candidate also wishes to express her sincere thanks to Mr. S. Y. Lau for his technical support in using some laboratory equipments and Mr. M. N. Yeung for his technical help in taking some SEM photos.

Thanks are also due to the candidate's colleagues and friends in the Hong Kong Polytechnic University for their encouragement and helps.

Finally, the candidate would like to thank the administration and technician staff in the Department of Industrial and Systems Engineering, for their provision of administration and technical supports.

List of Publications

Published:

1. **F. Hu** and K.C. Chan, Deposition behaviour and morphology of Ni-SiC electrocomposites under triangular waveform, Applied Surface Science, 243 (2005) 251-258.
2. **F. Hu** and K.C. Chan, Electrocodeposition behaviour of Ni-SIC composite under different shaped waveforms, Applied Suface Science, 233 (2004) 163-171.
3. **F. Hu** and K.C. Chan, Equivalent circuit modeling of Ni-SiC electrodeposition under ramp-up and ramp-down waveforms, Material Chemistry and Physics, in press.
4. **F. Hu** and K.C. Chan, Effect of magnetic field on electrodeposition of Ni-SiC composites, Journal of Solid State Electrochemistry, in press.

Conference:

5. **F. Hu** and K.C. Chan, Equivalent circuit modeling electrodeposition of Ni-SiC nano-composites, presented at the 206th Meeting of the Electrochemical Society, Honolulu, USA(2004).

Submitted:

6. **F. Hu** and K.C. Chan, Effect of pulse frequency on electrodeposition of Ni-SiC composites, submitted to Trans IMF.

7. **F. Hu** and K.C. Chan, Effect of duty cycle on electrodeposition of Ni-SiC composites, submitted to Surface Engineering.
8. **F. Hu**, K.C. Chan, S.Z. Song, X.J. Yang, Enhancement of corrosion resistance of electro-codeposition Ni-SiC composites by magnetic field, submitted to Journal of Solid State Electrochemistry.

List of Symbols

A, B : the electrodeposition constant

c_{ion} : the bulk concentration of ions

c_p : the concentration of particles

C : the concentration

D : the diffusion constant

D_p : the particle diffusivity

D_i : the diffusion coefficient of the electroactive ions

d : density of the metal

e : charge of an electron

E : the reversible potential

E_0 : the standard potential for the given metal

F : Faraday constant

ΔG_1 : the free energy of creation of new interface

ΔG_2 : the free energy of the growth of new grains

ΔG_c : the critical free energy

h : the height

H : the empirical factor that accounts for hydrodynamic effects

i : the current density

i_0 : the exchange current density

i_p : peak current density

j_p : the rate of particle deposition

j_p^n : the number of particles that reach the electrode per unit time

J : the nucleation rate

k : the rate constant

k_p : the reaction rate constant of the particle capturing process

K : related to the amount of energy needed for nucleation rate

m : the duty circle

M : the atomic weight

n : the number of electrons

N_P : the number of particles crossing the diffusion layer at the cathode per unit time and surface area

p_i : the probability to reduce one ion at current density i

P : the probability of a particle to become incorporated.

$P_{(k/K,i)}$: probability for the incorporation of a particle

r : radius

r_c : the critical radius of the surface nucleus

R : gas constant

t : time

t_{off} : pause time

t_{on} : cathodic time of mandrel

T: period of one cycle

u_p : peak voltage

V_p : the volume of one particle

V_Z : the fluid flow velocity

w : weight percent of particles in the deposit

W : atomic weight of electrodeposited metal

W_P : the weight of one particle

z : valence of metal

Greek letters

α : the volume fraction

δ_i : the diffusion layer thickness

γ : the reaction rate order

η : the overpotential

η_c : the critical overpotential

ν : the vector

θ : the dimensionless current density

ρ : the density of deposited composite

$\rho_{\lim}$: the radial distance of the limiting trajectory

σ : the surface free energy

σ_1 : the free energy between the grain and the solution interface

σ_2 : the free energy between the grain and the electrode

σ_3 : the free energy between the electrode and the solution interface

υ_0 : related to the rate of reduction of ions adsorbed on the inert particles

Subscripts

rec : due to applying a rectangular waveform with relaxation time

rdn : due to applying a ramp-down waveform with relaxation time

rup : due to applying a ramp-up waveform with relaxation time

tri : due to applying a triangular waveform with relaxation time

Table of Contents

List of Tables

List of Figures

Chapter 1 Introduction

Electrodeposition is a long-established manufacturing technology. In the past decades its application in micro-fabrication technology for miniature products and tools such as phonograph record stampers, high precision aperture plates for non-compact printing, microstructures for micro machines, sensor technology, and flexible circuits for PCB has aroused much research interest. Electrodeposits are becoming key components in a number of high-tech applications related to information technology and micro-mechanics. There has been some research to improve deposit quality by adjusting the bath composition or using pulse current. For example, nickel sulphamate has been used to reduce internal stress; and different shaped waveforms have been applied to improve the deposit quality.

However, most of work focuses on electrodeposition of metals or alloys. There is a need to develop electrodeposits with greater strength, increased hardness, better wear resistance and lower coefficient of friction. Composite materials which consist of inert particles and a metal have demonstrated that they possess many enhanced properties compared to metals and alloys. The electrolytic codeposition of particles with metals has been a research topic for more than a decade for the purposes of wear resistance, dry lubrication, anticorrosion and dispersion hardening. A variety of particles have been used including (i) inert materials such as silicon carbide, titanium carbide and alumina, (ii) lubricant materials such as PTFE, (iii) metallic materials such as chromium and (iv) liquid-containing microcapsules, and they have been applied to a wide range of applications including transducers, sensors, electrocatalysis, and to photoactive materials. The advantages of co-deposition are clear, since the technique offers an elegant way to combine the characteristics of different metallic and non-metallic materials in a controlled fashion.

In the electrodeposition of composites, the rate of particle entrapment depends on a number of factors including those relating to (i) processing parameters (e.g. current density), (ii) electrolytic solution (e.g. composition) and (iii) particles (e.g. size). By manipulating the processing parameters, some researchers have demonstrated that it is possible to produce different types of graded composites. Electrolysis with an imposed magnetic field, i.e., magnetoelectrolysis, has also been demonstrated that it can lead to a more uniform deposit morphology relative to conventional electrolysis. Nevertheless, more research work is required in order to give us a better understanding on the effect of current waveforms and magnetic fields on the distribution of particles, and of the deposition mechanisms of electro-composites. Regarding the theoretical investigation of the electrodeposition of composites, although several models have been established to explain its deposition mechanisms, the theoretical understanding of the codeposition process in agitated electrolyte is still considered to be relatively limited and there is a need to further investigate the mechanism of the process.

In this thesis, with the aim of developing composites with better mechanical properties, investigations will be carried out to examine the deposition behaviour and mechanisms of the composites in coelectrodeposition. Without adjusting bath composition or the volume percentage of particles during the process, two additional process variables, magnetic field and current waveforms, will be introduced in order to manipulate the microstructures and to enhance the deposit quality. The specific objectives of the project are:

1) to investigate the electrocodeposition behaviour of composites under different shaped current waveforms;

2) to study the effect of a magnetic field on the distribution of particles and on the quality of the deposit of electro-composites; and

3) to theoretically analyze the mechanisms of electrocodeposition under various processing conditions.

Chapter 2 Literature Review

2.1 Overview of Electrodeposition

2.1.1 Introduction

The electrolytic deposition of metals has made significant progress in past decades to meet the requirements of various industries. Eight major industries are related to the electrodeposition process: aerospace, automobile manufacturing, biomaterials, chemicals, electronics, energy, metals and telecommunications. Electrodeposition extends the use of applications by covering inexpensive and widely available base materials, with plated layers of different metals which have superior properties, and the electrodeposits would have been prohibitively expensive. It is known that electroplating is not a simple dip and dunk process, but most probably one of the most complex unit operations because of the unusually large number of critical elementary phenomena or process steps which control the overall process. Electrodeposition involves surface phenomena, solid state processes, and processes occurring in the liquid state, thereby drawing on many scientific disciplines such as electrochemical engineering, solid state physics, metallurgy and material science, and electronics.

Although the technique progressed rapidly in 1970's, fundamental changes in processes, in equipments and in materials have seldom come fast. A lot of these changes arise due to growing emphasis on quality, steep rise in the prices of chemicals and fuel and in the high cost of waste disposal. Therefore, a better understanding of the deposition behaviour and mechanisms of electrodeposition has to be achieved in order to lower the cost.

2.1.2 Background Theories of Electrodeposition

An electrodeposition process involves an electrochemical cell which consists of four major components: the anode, the cathode, the electrolyte, and an electronic conduction path between the anode and cathode. The anode is where oxidation, or loss of electrons, occurs, while the cathode is where reduction, or a gain of electrons, occurs. Typically, the cathode reaction will look as follows for metal plating.

$$M^{n+} + ne^{-} \rightarrow M \qquad (2.1)$$

The above reaction represents the overall deposition process, but does not take into account any intermediate steps. The main steps are 1. the migration of ions to the cathode surface and 2. the subsequent transfer of electrons. The metal ions are surrounded by water molecules or other complex agents, and migrate from the bulk solution by convection, diffusion, or because of the electric field. At the cathode surface the solvated metal reach a kink site or stable nucleus where it is energetically favourable for a charge transfer to occur and hence the metal becomes incorporated onto the metal lattice surface [1].

However, for many electrochemical cells, the actual cathodic reaction involves the evolution of hydrogen instead of the production of a metal, according to the following equation:

$$2H^{+} + 2e^{-} \rightarrow H_2 \qquad (2.2)$$

The electrolyte acts as the charge-carrying medium, and maintains charge equilibrium in the solution while the electrical conduction path between the anode and cathode is required to allow the electrons to flow.

2.1.2.1 Faraday's Laws

When an external current or overpotential is applied on the electrolytic bath, the metal will be deposited on the cathode and the anode will be dissolved. The amount of metal which is deposited on the cathode or dissolves from the anode is determined by the quantity of electricity that has passed. The rules giving the relationship between the amount of metal deposited or dissolved and the number of coulombs that have passed were first derived by Faraday in 1833, and hence they are generally known as Faraday's laws [2]. The weight of metal deposited at the cathode, or dissolved from the anode is proportional to the quantity of electricity,

$$W = \frac{I \times t \times M}{z \times F} \tag{2.3}$$

where z is the valence of the ions from which it is deposited on the cathode, or which is formed when the anode dissolved.

However, not the whole current that passes is devoted to the plating; other reactions may accompany the deposition of the metal on the cathode. The cathode efficiency is defined as the fraction of actual deposit weight/thickness and the theoretical deposit weight/thickness [3]. In most acid electrolytes the cathode efficiency rises with the current density tending to a maximum. At lower values of current density, the local variations in primary current distribution can be accentuated by the greater cathode efficiency at the higher current density regions. At higher current densities the variation in efficiency is reduced and so the effect is not so pronounced. Therefore the cathode efficiency can to some extent oppose the effect of secondary current distribution, and so a slightly lower cathode efficiency can improve the macrothrowing power [4].

2.1.2.2 Electrode Potentials

If any metal is placed in a electrolyte solution, a reaction at the electrodes occurrs, electrons are interchanged between the electrode and chemical species within the electrolyte that are close to the electrode. If the system is at a dynamic equilibrium and reversible, the potential is given by the Nernst equation [5].

$$E = E^0 + \frac{RT}{zF}\ln[M^{2+}] \tag{2.4}$$

In a sense, the electrode potential reflects the relative ability of a substance to enter into a chemical reaction either by gaining or losing electrons. Those reactions with the most positive potential are most likely to undergo reduction, while those reactions with the most negative potentials are most likely to undergo oxidation.

2.1.3 Polarization

Once current begins to flow in the electrochemical cell, the electrode potential of the system shifts. The cathode becomes more negative, and the anode more positive. The potential shift is referred to as polarization [6]. During reactions at an electrode the path taken by the moving ions requires energy, the amount of which relates to the potential of the ions within the cell known as partial polarization. The total overpotential is the sum of the three partial polarizations known as concentration, activation, and resistance overpotential.

Polarization experiments measure the relationship of the overpotential and current density. The equilibrium potential can be directly read from the logarithm of current versus potential plots. The slopes of the cathodic Tafel line and the anodic Tafel line give the cathodic and anodic Tafel slopes, respectively. By extrapolating the Tafel line to the equilibrium potential, the exchange current can be determined, as shown in Figure 2.1.

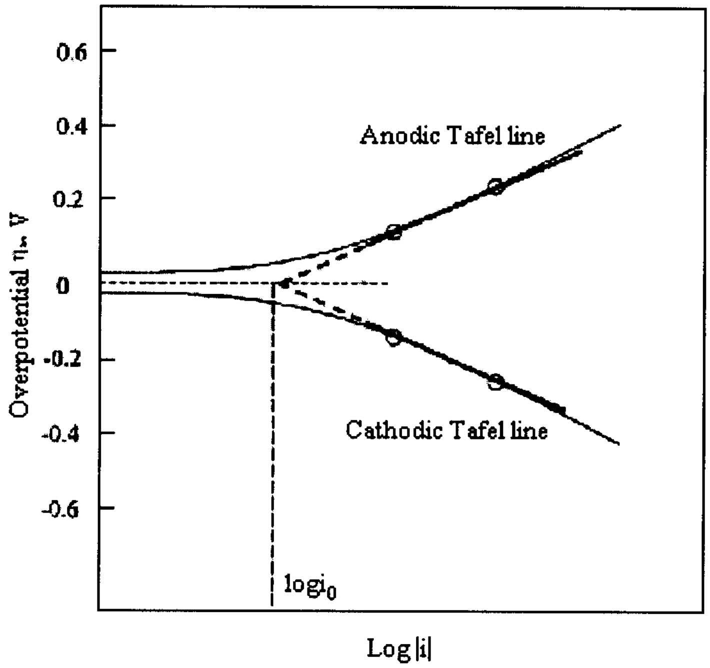

Figure 2.1 The relationship of current density and overpotential

2.1.3.1 Concentration Overpotential

The concentration overpotential arises as a result of concentration changes at the surface of the working electrode [7]. Assuming the electrodeposition system is running under an applied current, the electrode reaction proceeds very rapidly. In the case of anodic dissolution, the metal dissolves so quickly that there may be insufficient ligands to solvate the metal ions and thus a limiting current is reached. At the cathode, if deposition occurs too quickly the metal ions cannot diffuse from the bulk solution to the surface fast enough and a cathode limiting current density occurs. In both cases a diffusion layer is set up between the electrode surface and the bulk solution. In anodic dissolution the metal concentration is infinitely large because the concentration of ligands is zero, and in cathodic deposition the metal ion concentration is zero. From the Nernst Equation (2.4), the concentration of metal ions leads to infinitely positive and negative potentials as the limiting current density is approached. The departure from the linear Tafel plot is known as the concentration overpotential, and the process is diffusion controlled. The limiting current density can be increased in three ways: by increasing the concentration of the solution, by agitation, and by raising the temperature.

2.1.3.2 Activation Overpotential and the Tafel Equation

Unlike concentration overpotential, activation overpotential has significant effect for both the cathode and the anode. Activation polarization is a reaction-controlled phenomenon instead of a diffusion controlled phenomenon. In the cathodic reaction metal ions must lose their salvation sheath, gain electrons and hence be deposited upon the surface. The free energy for these reactions can be expressed in terms of Morse Curves [4]. For each reaction to take place, a certain energy barrier must be overcome. The activation energy is usually provided by the electrode potential, thus the electrode must polarize in order to provide sufficient energy for the reaction to take place. The anode tends to become more positive and drives the metal ions off faster, and the cathode becomes more negative allowing the reacting species in the electrolyte to receive the electrons more rapidly.

The activation overpotential is dependent upon the number of ions present in solution. The relationship between activation overpotential and the current density can be shown by the Tafel equation [8],

$$\eta = a + b \log i \tag{2.5}$$

where

$$b = \frac{2.3RT}{\beta zF} \tag{2.6}$$

Thus the activation overpotential has a linear relationship with $\log i$.

2.1.3.3 Resistance Overpotential

As the solutioin is not of infinite conductivity, it presents a barrier to the ions moving through it. This barrier is in the form of an ohmic drop in the solution between the working electrode and the reference electrode.

$$\eta_r = IR_r \tag{2.7}$$

where R_r is the resistance of the solution.

2.1.4 Electrodeposition

The typical current-potential behaviour for electrodeposition of metal is illustrated schematically in Figure 2.2. From the graph it can be seen that at potentials positive to the rest or equilibrium potential, anodic dissolution will occur. However, as the potential becomes more negative, the current reverses, and metal deposition occurs. As the potential continues to become more negative, eventually the limiting current density for the deposition process is reached. If the potential is made even more negative, hydrogen evolution and metal deposition will take place simultaneously. Thus, in order for an efficient deposition process, it is often best to operate near the limiting current density to prevent the evolution of hydrogen.

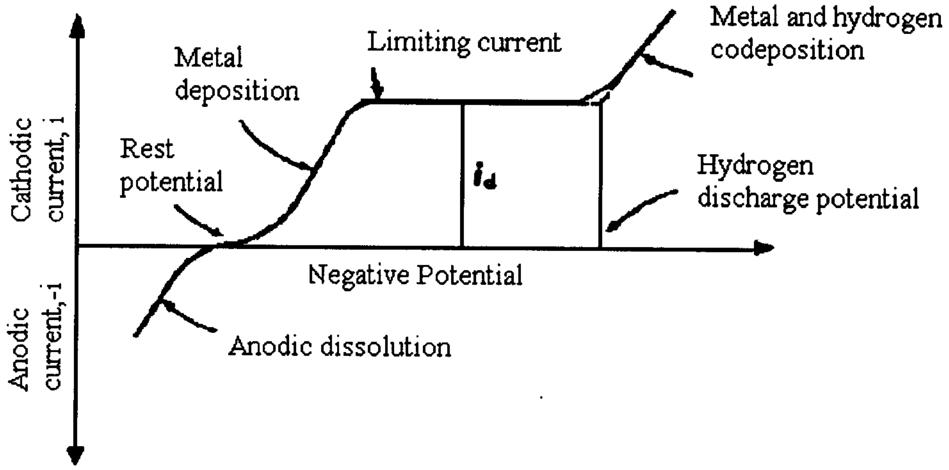

Figure 2.2 Schematic diagram of the typical current-potential behaviour for metal electrodeposition

The form of deposits depends largely on two factors; first, the rate of formation of crystal nuclei by discharging of the ions, and second, the rate of nuclei grows into large crystals. If the conditions favor the former one, the deposit will tend to consist of fine-grained crystals, and the deposits will be smooth and relatively hard. On the other hand, if the circumstances are such that the nuclei increase in size rapidly, the deposits will consist of relatively large crystals and be rough.

Nuclei are formed at favorable sites. Such sites are determined by their surface energies and the magnitude of the applied cathodic overpotential. Thirsk et al. [9] developed equations to describe the early stages of nucleation. They related the number of nucleation sites to the magnitude of the current and the time of deposition. The main equations are summarized below [10]:

For two-dimensional growth after instantaneous nucleation:

$$I = 2zF\pi MhN_0k^2\frac{t}{\rho} \tag{2.8}$$

For two-dimensional growth after progressive nucleation:

$$I = zF\pi MhN_0k^2\frac{t^2}{\rho} \tag{2.9}$$

For three-dimensional growth after instantaneous nucleation:

$$I = 2zF\pi M^2N_0k^3\frac{t^2}{\rho^2} \tag{2.10}$$

For three-dimensional growth after progressive nucleation:

$$I = 2zF\pi M^2AN_0k^3\frac{t^3}{3\rho^2} \tag{2.11}$$

These equations are only valid for the initial stages of nucleation until the crystals overlap. By analyzing the initial part of a current/time plot for a deposition process to determine the time constant, the type of nucleation process taking place can be identified. The technique makes use of the potential step method. The value of N_0 can also be found by SEM micrographs taken at the initial stages of deposition.

The texture and microstructure of the deposits are strongly influenced by the nucleation rate [11]:

$$I = k\exp\left(-4H^3\sigma^3 \Big/ 27z^2e^2\eta^2kT\right) \tag{2.12}$$

where z is the number of electrons transferred to the cathode by one atom or molecule, e is the electron charge, σ is the surface free energy, k is the rate constant and H is the shape factor which is equal to $(4\pi r^2)\times 2^{-1/3}$ (assuming a semi-spherical nucleus shape).

2.1.5 AC Impedance Spectroscopy

The response of electrodes to small amplitude alternating potential signals of widely varying frequency is called AC impedance spectroscopy. The AC impedance spectroscopy can determine a number of fundamental parameters relating to kinetics and mechanisms of an electrochemical process.

The impedance $Z(\omega)$ of an electrode surface may be evaluated from its time dependent current response $I(t)$ to a sinusoidal alternating potential signal $V(t)$ of an angular frequency ω by:

$$Z(\omega) = \frac{V(t)}{I(t)} \tag{2.13}$$

$$V(t) = V_0 \sin\omega t \tag{2.14}$$

$$I(t) = I_0 \sin(\omega t + \theta) \tag{2.15}$$

where t is the time, θ is the phase angle between $V(t)$ and $I(t)$.

The impedance, $Z(\omega)$, can be also expressed in terms of a real component, $Z^{'}$, and an imaginary component, $Z^{''}$

$$Z(\omega) = Z^{'} + jZ^{''} \tag{2.16}$$

where $j = \sqrt{-1}$.

The phase angle can be calculated by:

$$\theta = \arctan(\frac{Z^{'}}{Z^{''}}) \tag{2.17}$$

The impedance behaviour of an electrode may be expressed in Nyquist plots of $Z^{'}$versus $Z^{''}$or in Bode plots of $\log|Z|$ and $\log\theta$ versus frequency f in Hz, where

$$\omega = 2\pi f \tag{2.18}$$

These plots for a simple electrode surface are shown in Figure 2.3. The Nyquist plot shows a semi-cycle, with decreasing frequency in the clockwise direction. At very high frequency, the imaginary component disappears and the electric double layer capacitance, behaves like a shot circuit, and leaves only the ohmic resistance. At very low frequency, the capacitor of the double layer behaves like an open circuit, and leaves a sum of ohmic resistance and the faradaic reaction resistance or polarization resistance. The Bode plots give similar results. At intermediate frequencies, the capacitance of the double layer dominates the total impedance, and gives a maximal phase angle and a slope of -1.

An electrode surface undergoing an electrochemical reaction is typically analogous to an electric circuit consisting of resistors and capacitors. For example,

R_s is the ohmic resistance between the working electrode and the counter electrode. If a film forms and covers the cathode during the electrodeposition, it must be bigger than it is in the case of electrodeposition without the presence of the cathode film. The faradaic reaction resistance R_{ct} is inversely proportional to the exchange current density. Under the equilibrium conditions,

$$R_{ct} = \frac{RT}{nF} \cdot \frac{1}{i_0} \tag{2.19}$$

where i_0 is the exchange current density.

Through measuring the ohmic resistance and faradaic reaction resistance by AC impedance spectroscopy, the reaction mechanism at the electrode surface will be clarified.

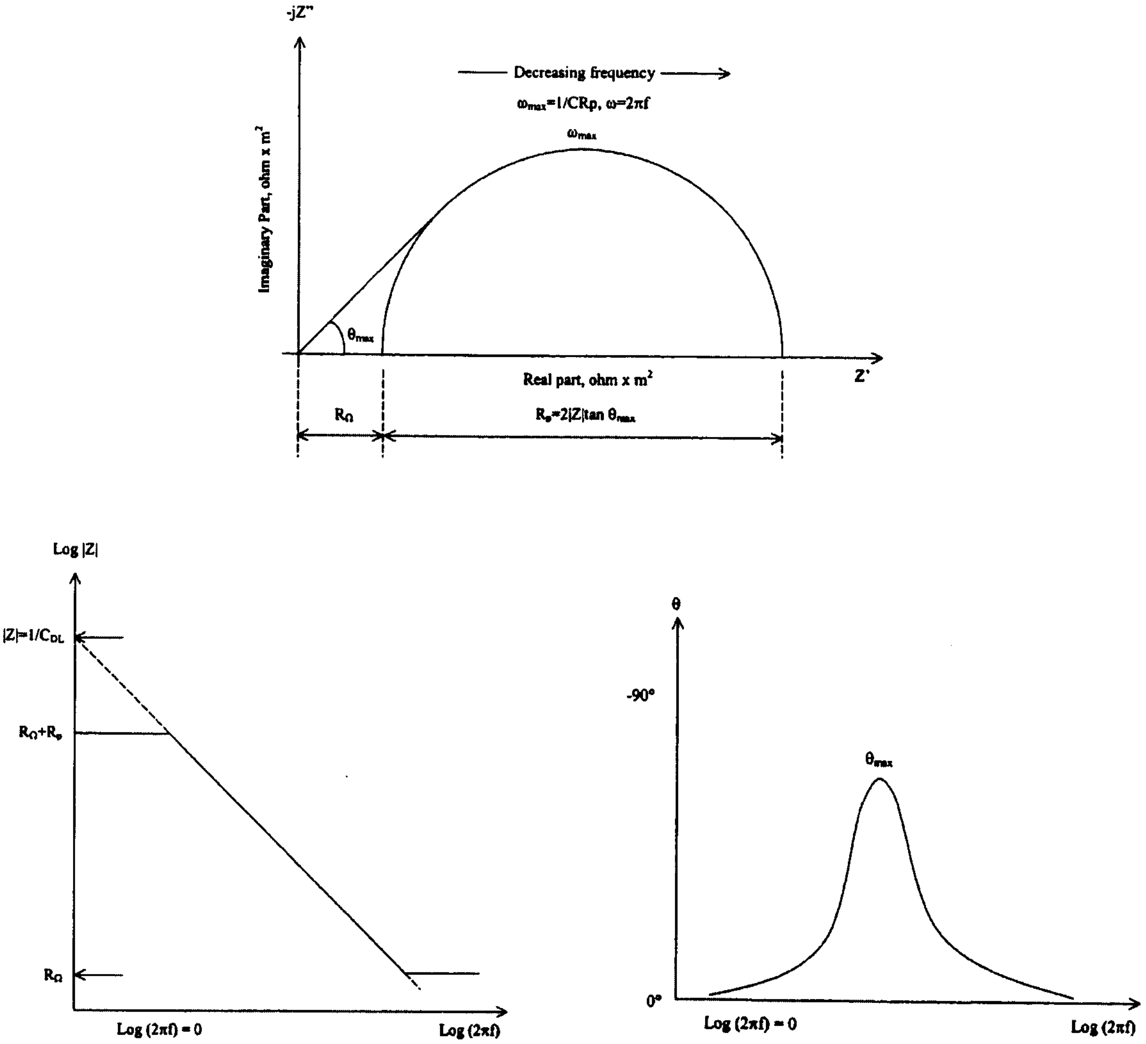

Figure 2.3 The impedance plots for a simple electrode surface

2.2 Electrodeposition of Composites

The general mechanism of electrocodeposition is regarded as involving the following stages [12~15]:

1) The ionic adsorption of particles which are suspended in an electrolyte [16].

   The extent and nature of the adsorbed ions determine the size and magnitude of the charge carried by the particles.

2) The transport process of the solution.

   The mode and intensity of agitation are common determining factors for the particle content in the deposit, and improved agitation is helpful to obtain a better composite layer.

3) The loose adsorption between particles and electrode.

   Loose adsorption is a reversible electrolytic contact, which is closely dependent on the charge size and charge magnitude of particles, the specific gravity of particles, and the contact time between particles and the electrode. High electrode velocity (for RDE) can overcome the attractive force of loose adsorption between particles and the electrode, and can carry the adsorbed particles away from the electrode surface.

4) A strong adsorption process, which traps particles into the metal matrix.

The incorporation of particles can be distinguished into two main groups [15]. In the case of “physical dispersion” plating baths, an important contribution to the theory for codeposition of dispersed particles in metallic matrix was derived by Guglielmi in 1972. His model was a two-step model that combined effects of adsorption and electrophoretic attraction, and arrived at a plausible explanation for the relationship between the current density and the volume fraction of the particles in the electrolyte and the deposit. Roos and Celis [17, 19, 22] performed an extensive study of the incorporation by assuming five consecutive deposition stages. Under the control of the hydrodynamics, a theoretical model could be used to approximately predict the weight percentage of inert particles as a function of current density in a range of $0\sim6\,\mathrm{Adm}^{-2}$. A statistical model further resolved the probability of a particle becoming incorporated, and an expression for the weight percentage of embedded particles was provided as a function of current density. The main parameter of the model was a transition current density at which the metal ion reduction changed from charge transfer control to mass transport control [18].

The second strategy describing the incorporation of inert particles involves the use of surfactants at the particle surface. These surface agents were originally used for wetting and stabilization for fluoropolymers. Later, cationic substances were also proved very useful for the dispersion of materials in plating baths. The use of a judicious mixture of nonionic and cationic surfactants to achieve independent control of the surface charge on the particles and their degree of dispersion in the plating was introduced in 1970s, and the addition of surfactants is now generally used in the electrocodeposition process.

The modeling of the composite plating process is hindered by the two-phase characteristics of the interactions of solids and liquids as well as by the many-body aspect of the mathematical description of the two-phase flow [13, 19]. Our theoretical understanding of the process of codeposition of inert particles in a metal deposit is limited, and existing theories do not provide a convincing description of the process kinetics, therefore, it is necessary to develop models which consider charge transfer, mass transport, adsorption, and surface charge properties prevailing at the surface of the inert particles [15, 20].

2.2.1 Co-deposition Theories

2.2.1.1 Guglielmi's Models

The Guglielmi's model agrees that the surface charge, which is manifested by the zeta potential, is the principal factor in determining the feasibility of the codeposition. And the main influence on the codeposition rate of particles lies in the strength of the force of attraction in and near the diffusion layer. As a result, the particle is held at the surface until the metal coating around mechanically entraps the particle [13].

It is a two-step model in which the combined effect of adsorption and electrophoretic attraction is responsible for the entrapment of particulate matter in a growing electrodeposit. In the first step, a layer of loosely adsorbed particles with a rather high coverage is transported to the Helmholtz's double layer by mechanical agitation. Then particles charged in the high potential gradient are transported to the cathode surface by electrophoretic attraction and are adsorbed on the cathode surface by Coulomb force which exists between particles and adsorbed anions to produce a strong adsorption of the particles onto the electrode. The purpose of the rationale is to arrive at a plausible explanation for the effect of current density on the observed volume fraction of the embedded particles. The model of the electrodeposition process was the first to be put forward that can be experimentally verified.

Based on Langmuir's adsorption isotherm theory and Faraday's laws, Guglielmi deduced the codeposition model:

$$\frac{\alpha}{1-\alpha}=\frac{nFd\upsilon_0}{Wi_0}\cdot e^{(B-A)\eta}\cdot\frac{kC}{1+kC} \tag{2.20}$$

When high voltage was applied on the electrolyte, the surface overpotential could be described by the Tafel equation, which is written as: $i/i_0 \approx e^{A\eta}$, then

$$\log tg\phi = \log\frac{Wi_0^{B/A}}{nFd\upsilon_0}+\left(1-\frac{B}{A}\right)\log i \tag{2.21}$$

From the equation, the parameters W, i_0, n, F, d, A and i can be determined by the process of metal deposition. B and k are related to the particle deposition, so the particle volume fraction in the deposit is influenced by the value of υ_0. Celis and Roos deduced that υ_0 is related to the rate of reduction of ions adsorbed on the inert particles [19]. Although several researchers have experimentally validated the model, some important process variables, such as size, type and pretreatment of the particles, composition, temperature and pH of the plating bath, as well as hydrodynamic effects are not considered in the model.

2.2.1.2 A Statistical Model/ Model of Buelens

Celis and Buelens et al. developed a statistical model to predict the probability of a particle becoming incorporated into a metal matrix [13, 22]. It hypothesized that a particle would be embedded only if a certain fraction of the adsorbed ions on the particle's surface was reduced. And two processes played a fundamental role in the codeposition mechanism: (i) the adsorption of ions onto the particle and (ii) the reduction of these adsorbed ions at the cathode surface. Codeposition in the statistical model is a five-step process [22]:

1) A double layer of adsorbed species is formed around each particle in the electrolyte,
2) Stirring carries particles, to the limit of the hydrodynamic layer,
3) Under the influence of an electric field, only the positively charged particles will be diffused to the cathode surface. The adsorbed particle above all negative ions will be diffused back into the bulk of the electrolyte solution,
4) Free or adsorbed electroactive species are reduced at the cathode,
5) The particle is included in the deposition when the adsorbed ion species on it is reduced at the cathode surface.

Using the statistical mechanism, a model was capable of predicting the weight percentage of incorporated particles. A certain amount of ions adsorbed on the particle must be reduced at the cathode and the particles correspondingly became incorporated. This was one possible way to account for the transition between loosely and strongly adsorbed particles, which is described in Guglielmi's model. The proposition yielded the probability $P_{(k/K,i)}$ for the incorporation of a particle based on the reduction of q out of Q ions, bound to its surface, at current density i

$$P_{(k/K,i)} = \sum_{j=q}^{Q} \frac{Q!}{j!(Q-j)!}(1-P_i)^{Q-j}\, p_i^{\,j} \tag{2.22}$$

where p_i is the probability of reducing one ion at current density i. The rate of particle deposition was given by

$$j_p = P_{(k/K,i)} H V_p j_p^n \tag{2.23}$$

where j_p^n is the number of particles that reach the electrode per unit time, H is an empirical factor that accounts for hydrodynamic effects and V_p is the volume of one particle. The number of particles j_p^n that collide with the electrode can be derived from the reduction rate of ions

$$j_p^n = j_{ion} \frac{c_p}{c_{ion}} \left(\frac{i_{tr}}{i}\right)^{\alpha} \qquad 2.24)$$

where c_{ion} and c_p are the bulk concentration of ions and particles and c_{ion} is directly proportional to the metal deposition rate. The equations were valid when the reduction rate of ions was the rate-determining step.

Thus, the weight percentage of particles in the deposit was defined as follows:

$$w(\%) = \frac{W_P N_P P}{\frac{M_m i}{nF} + W_P N_P P} \times 100 \qquad 2.25)$$

where W_P is the weight of one particle, N_P is the number of particles crossing the diffusion layer at the cathode per unit time and surface area, and P is the probability of a particle of becoming incorporated.

The statistical model was found to be valid for two experimental codeposition systems, namely, copper-aluminum oxide, deposited from acidic sulfate baths, and gold-aluminum oxide, deposited from additive-free potassium cyanide baths. But the model still cannot directly predict the particle content from the experimental conditions, and some factors needed to be determined by correlating them with practical results.

2.2.1.3 Model of Valdes

Valdes considered the incorporation of Brownian particles, and the effects of hydrodynamic convection, electromigration (electrophoretic transport) and diffusion migration among the transport mechanisms are considered in the model. The particles were thought to move the cathode surface through the above forces [25]. Among the forces, the electrophoretic and diffusiophoretic motion is caused by the polarization of the double layer surrounding a charged particle in respect to an electric field and a concentration gradient. And the electrophoretic transport is determined by the sign and value of the zeta potential of the particle. Diffusiophoresis drives particles towards regions of higher electrolyte concentration, irrespective of whether there is a sign of surface charge of the particle.

The electrodeposition of Brownian particles on a rotating disk electrode (RDE) was modeled by solving a steady-state convective diffusion equation in three ways: the Perfect Sink (SINK) model, the Surface Force Boundary Layer Approximation (SFBLA) model and the Electrode-Ion-Particle-Electron Transfer (EIPET) model.

The SINK model referred to infinitely fast particle deposition kinetics, which bypassed the problem of a lack of understanding about particle/electrode interactions at the electrode/solution interface [13]. It was assumed that all particles approaching within a critical distance of the surface were irreversibly and instantaneously captured. In case of codeposition on a rotating disk electrode (RDE), the transport of colloidal particles in an electrolytic dispersion was treated by considering a differential mass balance. The codeposition model was mass transport controlled, and the flux of particles was given by

$$j_p = \frac{D_p^{2/3} D_i^{1/3} c_p}{\delta_i} \tag{2.26}$$

where D_p is the particle diffusivity, D_i is the diffusion coefficient of the electroactive ions and δ_i is their diffusion layer thickness.

In the SFBLA approach, the electrophoretic and diffusiophoretic were considered, and the flux of particles was given by

$$j_p = \frac{c_p}{\dfrac{\delta_i}{D_p^{2/3} D_i^{1/3}} + \dfrac{1}{k_p}} \tag{2.27}$$

where k_p is the reaction rate constant of the particle capturing process. The model could only be applied when an energy barrier existed due to the superposition of attractive and repulsive forces.

In the EIPET condition, the electrochemical reduction of electroactive ions adsorbed on the particle provided the essential surface binding interaction which was responsible for particle deposition on the cathode. The flux of particles was given by

$$j_p = \frac{c_p}{\frac{\delta_i}{D_p^{2/3} D_i^{1/3}} + \frac{1}{k_p[1 + \theta(i_{\lim} / i_0)(1-\theta)^{-\gamma}]}} \tag{2.28}$$

where i_0 is the exchange current density, θ is the dimensionless current density $(i / i_{\lim})$ and γ is the reaction rate order. EIPET couples particle deposition to the reduction of metal ions, and the deposition of particles also obeys Bulter-Volmer kinetics.

2.2.1.4 The Trajectory Model

There are a number of models developed for Brownian particles, which are smaller than 1 μm. But in most cases particles that are industrially codeposited are larger than that size. Fransaer et al [26] developed a more precise description for the codeposition of non-Brownian particles, and they established the electrolytic codeposition model for spherical particles incorporated into a metal matrix on a rotating disk electrode (RDE). The model was based on a trajectory analysis of particles, including convective mass transport, geometrical interception, and migration under specific forces, coupled to surface immobilization reactions. The codeposition process was regarded as two sub-processes, namely the reduction of metal ions and the concurrent deposition of particles. Two types of relevant forces were discerned including forces of fluid mechanical origin and other external forces. They are those exerted by the fluid on the particle, and the forces that act on the particle itself. The forces are classified as those that tend to maintain particles attached to the surface and those that tend to remove them. Several parameters, in particular the surface chemistry, the size of the particles, the flow rate and the current density are also taken into consideration [21].

With the fluid flow field around the electrode and considering the forces mentioned above, the number of particles that were in contact with the electrode was calculated. The particle flux to the rotating disk consisted of all particles whose trajectories fell within the limiting particle trajectory, was defined as the particle trajectory that divided incoming particles with terminal contact from those which passed by. The volume Flux j_p of particles colliding with the disk per unit time was given by

$$j_p = \frac{4}{3}\pi^2 a_p{}^3 c_p V_Z \rho_{\text{lim}}^2 \tag{2.29}$$

where c_p is the volume concentration of particles in the bath and V_Z and ρ_{lim} are respectively the fluid flow velocity and the radial distance of the limiting trajectory at the axial distance where the particle trajectories coincide with the undisturbed streamlines. It was found that the rate at which particles were brought to the electrode was governed almost entirely by the convection instigated by the rotating disk and the dispersion forces.

The trajectory description takes into account the effect of rotation speed, radial position and current density on the number of particles. If the ratio of the normal to the tangential force acting on the particle is favorable, a particle remains on an electrode and is engulfed by the growing metal. In the center of a RDE, tangential forces are absent and the rate of codeposition is controlled by mass transport of particles towards the electrode.

The trajectory model is capable of explaining why polytetrafluoroethylene and other polyfluorocarbon compounds, despite their lower dispersion force, have appreciable codeposition. Thallium, rubidium and cesium promote codeposition because these ions adsorbed to the surface of the particle, with weakly bound hydration sheets, lower the salvation force around the particle. Moreover, the effects of additives that increase codeposition can be attributed to the hydration force.

2.2.2 Experimental Investigation

The electrolytic codeposition of particles with metals has been a research topic for more than a decade, as the technique of codeposition offers an elegant way to combine the characteristics of different metallic and non-metallic materials in a controlled property. In general, the microhardness [23, 27, 28], tribological property [24], internal stresses, anti-corrosion properties [29], and wear resistance are enhanced by the presence of the second-phase particles [30, 31].

A significant amount of research has been conducted on electrodeposition of metals, alloys, and composites, and most of the work focuses on maximizing the amount of particle incorporation or on improving a specific property of the codeposited film, i.e., better microhardness, lower wear rates, excellent corrosion or oxidation resistance. This chapter reviews the effect of process variables on the properties of composites.

2.2.2.1 Effect of Particle Characteristics

2.2.2.1.1 Composition and Crystallographic Phase

Particles can be characterized by their composition and crystallographic phase, as well as by their size, density, and shape. Particles have a dramatic impact on the amount of incorporation obtained for a particular bath composition. For instance three times more TiO_2 than Al_2O_3 has reportedly been incorporated into a nickel matrix, under the same deposition conditions [32].

The effect of particle crystallographic phase is important to electrodeposition. While one phase of a specific composition may readily incorporate from a particular bath composition, another phase of the same composition may incorporate to a much lower extent or not at all. For instance, the alpha alumina particles were found to incorporate from an acid copper bath while the gamma phase incorporated was less than one tenth the amount of alpha [32]. Similarly, hydrophobicity/hydrophilicity of the particle surface, for the oxidation of the SiC surface, could also diminish the rate of particle incorporation within a nickel matrix [18, 33].

2.2.2.1.2 Particle Size

Decreasing the particle size resulted in a decrease in the amount of incorporation. A higher volume percent of codeposited SiC was achieved with larger particles, and a lower codeposition was obtained with smaller particles [34]. Similar trends were also found in Ni-Cr, Cu-P, $Ni\text{-}Al_2O_3$ systems [35]. However, other researchers reported that the particle size had a negligible influence on the amount of incorporation for $Ni\text{-}Al_2O_3$ [36] and SnNi-SiC [37]. Even a decrease in the amount of incorporation with increasing particle size was observed for a $Ni\text{-}Al_2O_3$ system [38]. When SiC particles are larger than $0.1\,\mu m$, a SiO_2 layer would be produced on the SiC particles which is weakly bonded to the nickel substrate and will create pores and cracks at the interface [39]. The reduction of particle size would also perturb the growth of the nickel matrix, and resul in small grain sizes and random orientation of the composites coatings [40].

The increasing incorporation of particles with increasing particle size was believed to relate to the Coulomb force. Since nickel ions will be adsorbed on larger particles which results in a strong Coulomb force, particles which are too large have a tendency to sink due to their gravitation, which decreases the amount of codeposition [41].

The concept of number density points out that the direct comparison of volumetric percentages of particles of different sizes leads to a misapprehension of codeposition [42, 43]. For a given number density of particles in the plating solution, the number density of particles in the coating increases with decreasing particle size [43]. Number density of particles further proves that the smaller particles will result in an improved hardness, although the volume percentage of particles is low [30],

2.2.2.1.3 Particle Loading

The particle loading in suspension typically ranges from 2 to $200\,g/l$. At low loadings, codeposition is limited by the supply of particles to the electrode. As the particle loading increases, the incorporation level increases correspondingly. But at a high loading, the increase in incorporation is not proportional to the increase of particle loading. The incorporation of particles was found to increase with increasing particle concentration in the bath [44, 48], and towards a saturation value [45], or even a lowly decrease [46]. The trajectory analysis proposed by Fransaer et.al [26] quantitatively predicted that the quantity required to codeposit $5\,\mu m$ particles was calculated to be 10 times smaller than that of $20\,\mu m$ particles. For the Ni-SiC electrodeposition system, it was reported that the highest volume percentage of SiC was obtained at a particle content of $50 \mathrm{g/l}$ when varying microsized particle contents from 13 to $150 \mathrm{g/l}$ [41]. For other systems [47] the optimum concentration for maximum incorporation was $60 \mathrm{g/l}$, beyond the optimal concentration. Particles appeared to agglomerate in the bath and a decreasing trend of SiC incorporation was observed.

2.2.2.1.4 Other Effects

The suspension of particles also influences the electrochemical behaviour. A higher current density was observed for a given cathodic potential in the presence of particles [48]. Yeh and Wan [12] found that SiC particles promoted a greater area for the adsorption of $\mathrm{Ni}^{+}_{\mathrm{ads}}$ intermediate which was in the form of $\mathrm{SiONi}^{+}_{\mathrm{ads}}$ on the surface, and the chemical caused an increase in pseudocapacitance. The addition of particles to the electrolyte was reported to enhance the ionic transport from the bulk to the cathode surface by their adsorbed ionic layer, and thus activates the nickel reduction [49]. The SiC particles were also a medium for hydrogen ions transfer, and they would enhance hydrogen evolution at lower pH [50]. Particles in the electrolyte, as generally known, acted as nucleation centers, which led to a decrease of the crystal size within the limiting current density [51~53]. Until now, no investigations on the influence of particle shape on codeposition have been reported. However, the particle shape affected the adsorption of ions on the particle surface and also affected the suspension stability [48].

2.2.2.1.5 Improved Properties

The amount and size of particles define two kinds of reinforcing mechanisms in metal matrix composite materials, namely dispersion-strengthening and particle-strengthening [43, 54, 55]. The dispersed particles in the matrix will obstruct the movement of dislocations and resist the plastic flow of the matrix, thus improving hardness [45, 56].

For many practical applications, wear resistance is a major property, and codeposition of ceramic particles on a metallic matrix is a common way to increase wear resistance [47, 57]. The wear resistance as a function of particle loading was observed in a Ni-P alloy matrix. Weight loss decreased with increasing particle contents, and reached a minimum value with twenty percentages of particles in the coatings. This could be explained by the fact that an excessive quantity of SiC particles accumulated on the surface, and formed a soft constituent [45].

The Ni-SiC composite coatings also gives a better corrosion resistance in a 0.6M NaClsolution than pure nickel electrodeposited ones. The corrosion current density of Ni-SiC ($5 \times 10^{-8} Acm^{-2}$) decreased by two orders of magnitude as compared to pure nickel coatings. The improved corrosion resistance was quite independent of the size and amount of embedded SiC particles. The improved corrosion resistance of Ni-SiC coatings containing submicrometric SiC particles was linked to a change in grain morphology and texture of the coatings, which evolved from columnar grains to small and equiaxed grains [34]. Coatings like zinc with

SiO_2 or copper with Al_2O_3 also showed a corrosion resistance two to three times higher than that of pure metal coatings [29, 58].

2.2.2.2 Current Density

When the current density increased, the amount of particle incorporation in the deposits was found to increase for the Ni-TiO_2 system with a relatively slow agitation [32], and SiC particles for the Ni-P-SiC system [45]. But it decreased for diamond in the Ni-Diamond system [23], $MoSi_2$ particles in the Cu-$MoSi_2$ system [59], and Au in the Au-Cu system [60]. A maximum in codeposition as a function of current density was observed for the Ni-TiO_2, ZnNi-SiC systems [47], Ni-SiC system. However, a minimum in codeposition as a function of current density was found for the Cr-Al_2O_3 system when the particle loading exceeded $100 g/l$. A shift of the codeposition maximum to a higher current density was observed when the agitation rate increased for the nickel matrix TiO_2 particle system, Au-Al_2O_3 and Ni-Al_2O_3 systems.

Stojak et al [32] stated that the particle incorporation behaves as a function of increasing current density, and it could be divided into several general regions. Firstly, the incorporation increases sharply and reaches a maximum value, and this is followed by a sharp decrease in incorporation; then a range where incorporation is relatively constant, and lastly another decrease occurs, for mass transport limited conditions are the determining factor. The regions wherein the incorporation sharply increases or decreases with current density are sensitive to particle size, crystallographic phase, and even to the electrodeposition process itself.

Some authors [47] proposed that the codeposition behaviour was determined by the reaction mechanism (charge-transfer or mass-transport controlled process). Up to the current density maximum, codeposition was controlled by charge transfer, which was in favour of increased current density. An increase in current density thus resulted in more rapid deposition of metal ions and more particles were embedded in the coatings. Beyond this point the process changed to mass transport control. A different explanation, however, proposed that solvation or structural force was the adhesion force governing particle incorporation. The maximum in the particle incorporation as a function of the current density curve was due to a minimum in the solvation force at the potential of zero charge (PZC) of the depositing metal [47].

Kim et al [61] presented the reason for high incorporation at low current densities. He suggested that particles were transported from bulk to the Helmholtz' double layer by mechanical agitation, and metal ions were moved to the cathode surface by electrophoresis. The adsorption of particles was driven by the Coulomb force, and then buried by deposited metal. At high current density, nickel ions dissolved from the anode were transported faster than SiC particles by mechanical agitation, which resulted in a low volume percentage of the co-deposited SiC. At low current densities, nickel ions dissolved from the anode moved slowly, so there was not sufficient time for them to be adsorbed on particles. As a result, the Coulomb force between anions adsorbed on particles and the cathode became weak, leading to a lower volume percentage of the codeposited SiC [41].

Meanwhile, the microhardness could be ameliorated by alternating the current conditions [27, 56, 62]. When fixed at 50℃ and a current density of $0.6\,\mathrm{Adm}^{-2}$, bright, adherent, fine-grained and almost defect-free nickel deposits with moderately high hardness could be obtained [63]. And the hardness increased with an increase in peak current density in the range of $2\,\mathrm{Adm}^{-2}$ to $15\,\mathrm{Adm}^{-2}$, but the hardness tended to decrease when the current density was above $15\,\mathrm{Adm}^{-2}$ [64].

2.2.2.3 Composition

A nickel sulphamate plating solution noticeably decreased the internal stress compared to typical Watt's Bath. But higher concentrations of ammonium or sulfate ions would increase the internal stress [65~67]. Moreover, the halide ions in solution also have a great influence on the internal stress [68]. At iodide concentrations greater than 0.1M the deposited nickel exhibited a fine granular texture of disordered crystal orientations. The internal tensile stress deposited from the iodide baths tended to rise with increasing iodide concentration to values considerably higher than those observed at similar concentrations of $NiCl_2$ or $NiBr_2$. But the sulphamate plating bath should avoid high temperature because the production of hydrolysis, ammonium and sulfate ions would cause an increase of the internal stress [69].

2.2.2.4 Effects of Additives

To improve the incorporation of inert particles, some specific ions and surfactants are used. These change the surface charge of the inert particle. Certain surfactants are selected which influence the structure of the composites layer adversely, to modify the surface charge of the particles through adsorption, or to favor the dispersion of particles in the bath [70, 71]. The disadvantage of using surfactants is that they may adsorb on particles and incorporate with metals, and result in stressed or brittle deposits [15].

Brighteners and wetting agents are usual surfactants in electrodeposition. If they influence the electro-codeposition process as cationic surfactants, they correspondingly promote incorporation of particles, and they confer a negative charge on the particles by acting as anionic surfactants [48]. A cationic surfactant (AZTAB) adsorbed on SiC particles probably desorbs, and produces to a greater than 62.4% incorporation of SiC particles in the deposits [46, 72]. The addition of small amounts of monovalent cations, like Tl^+, Ce^+, Rb^+ and NH_4^+, or amines, like TEPA will improve the incorporation of particles [37, 39, 48, 73, 74].

Such surfactants as cetylpyridimium chloride, SDS, cetyltrimethylammonium bromide (CTAB), polyethylenimine (PEI) are effective to create the dispersion of particles, and they significantly decrease the agglomeration of particles. Therefore a higher amount and a greater uniformity of embedded particles can be achieved [48, 30, 49, 75~78].

The grain size of electrodeposited composites, such as Ni-SiC, Cu-Co, can be reduced to a nanosized range by using additives such as coumarin and saccharin [44, 79~82] and some suppressor compound [83], which acts as an inhibitor limiting the surface mobility of adions on the cathode surface. A decrease in grain size in the matrix results in a considerable reduction of plastic deformation and improvement of wear resistance [30, 84]. The composition and morphology of Co-Ni and Co-Fe alloys and the cathodic current efficiency are improved with the addition of substances of saccharin and sodium lauryl sulfate in Watt's type electrolyte [85, 86]. However, these additives introduce carbonaceous material or sulfur into the metal matrix, and act as solid solution strengtheners and cause intergranular embrittlement [79].

2.2.2.5 Surface Charge and pH Value

It is believed the pH value plays an important role in the electrodeposition process by changing the surface charge of the materials in the electrolysis. It has been noted that SiC powders have a positive surface charge at a pH value less than 2.2 and a negative surface charge at a pH value higher than 2.2. Surface charge obviously increases as the pH value decreases. And the addition of SiC particles to the solution will also decrease the pH value when the initial value is greater than 2.0 [12].

Fink and Prince in 1928 already realized the importance of the surface charge, and they stated that a positive surface charge enhanced particle incorporation because the particles were electrostatically attracted to the cathode [48]. A higher volume percentage of codeposited SiC was obtained by adjusting pH value [41], owing to the fact that SiC particles have a strong tendency to adsorb H^+ at the lower pH levels, and the amount of nickel ions adsorbed on the surface of the SiC increased with an increase in pH value [48]. Particles with a surface charge formed more stable suspensions, because their mutual repulsion and agglomeration could be avoided [48, 71].

The pH value also related to the grain size and the morphology of the deposit. At a pH value of 2.8, columnar grains were obtained and its average crystallite size increased from $283\,nm$ on the substrate side to $342\,nm$ on the solution side. As the pH value increases, the crystallite size decreased and became more uniform through the thickness. It has been explained that the pH enhanced the nucleation rate of nickel crystals. In general, a pH value smaller than 3.0 should be avoided since nickel sulphamate forms nickel ammonium sulfate which has less solubility [41, 87~90], and the hydrogen evolution at a low pH value is a mechanical barrier to the approach of hydrophyllic SiC to the cathode surface, and leads to a strong decrease in incorporation [50].

Conversely, a slight effect of pH value on the amount of Al_2O_3 particles incorporation was reported above the pH value of 2.0. However, decreasing the pH value below 2.0 resulted in a sharp decrease in the amount of particles incorporated, even to the point where there is no particle incorporation obtained for copper plating with SiC or Al_2O_3. Other researchers [91] found no effect of pH value on the incorporation of $BaSO_4$ within a copper matrix, in the presence of tetraethylene pentamine, although in the presence of thallous, ion incorporation for the same system was found to increase with pH value.

The increase in solution pH value close to the electrode as a consequence of hydrogen evolution promoted the codeposition of OH^- and/or O as hydrated basic nickel salts, $Ni(OH)^-$ or NiO inclusions in the deposits [68], and led to an increase of internal stress in the deposited films.

2.2.2.6 Agitation and Temperature

Electrocodeposition requires the keeping of the particles in suspension so as to facilitate their transport to the cathode surface. Increasing the bath agitation in the parallel plate electrode is found to increase the amount of particles incorporated, but too high agitation will result in a decrease of codeposition rate. Codeposition of the silicon carbide particles showed that a maximum volume percentage was obtained at $500\,\mathrm{rpm}$ for all concentrations in the bath [41, 47]. Up to $500\,\mathrm{rpm}$, the collision of SiC particles against the cathode increased, and resulted in an increase of SiC incorporation. Above $500\,\mathrm{rpm}$, SiC particles drifted away and resulted in a decrease of the SiC incorporation. Sufficient agitation for electrodeposition is necessary to maintain the particles in suspension and to transport them to the electrode surface. However, if the agitation is too intense, the residence time for the particles at the electrode surface is insufficient and the particles are swept away before they can be incorporated into the metal film [48, 92, 93].

For the effect of agitation with a RDE, three different flow regimes can be distinguished: laminar, transition and turbulent. Increasing the electrode rotation rate within the laminar regime was found to have no effect on the amount of incorporation. In the transition regime a decrease of the particle content with increasing rotation rate was observed. While in the turbulent regime a continuous decrease took place. The particle content decreased from the center to the edges of a RDE [48]. Codeposition was explained as competition between particle adhesion and particle removing forces. At low rotation speeds the fluid flow induced by the RDE was not capable of transporting all the particles to the cathode and, when the rotation speed was too high, the rate of particle removal became greater than that of attachment at certain sites on the electrode [47].

The effect of bath temperature on the amount of particle incorporation seems to vary for different codeposition systems. For Ni-Al_2O_3 system, temperature over the range of 20 to 80℃ had no effect on the percentage of particles incorporation. On the other hand the graphite content in a Cr-matrix increased with temperature up to 50℃ [48] and a maximum particle content for Ni-SiC system was obtained at 50℃ when varying temperature from 30~70℃ [46].

The use of a low plating temperature (27℃) resulted in highly stressed deposits because of a higher gas content than in those plated at the normal operating temperature of 60℃. Deposits obtained at low temperature were unsuitable for structural or electroforming applications [93].

2.2.2.7 Heat Treatment

Heat treatments always give rise to recrystallization of grains and grain growth in the deposits [63, 94]. Some structure transformations from amorphous to crystalline were observed when the grains were heat treated [45]. The microstructure change in the gradient coating could be eliminated due to the recovery and recrystallization of the nickel matrix [51]. The crystalline microstructure transformation was influenced by heat treatment temperature. After annealing at temperatures higher than 300℃, the recrystallized nuclei were observed on the (110) oriented deposits, which contain high-density dislocations and numerous twins, and an equiaxed grain structure was observed on the nickel deposits annealed at 600℃. Conversely, for (100) oriented deposits, which contained fewer lattice defects, the recovery and grain growth prevailed in the absence of pronounced recrystallization after one hour of annealing at temperature up to 600℃. The different annealing behaviours associated with the distinct textured nickel deposits could be explained by their different lattice defects. The population density of twins associated with the as-deposited nickel markedly affected the feasibility of the formation of twin-free recrystallized nuclei [95, 96].

With heat treatment up to 1000℃, particles would inhibit the growth of matrix grain, and strengthening occurred according to the Hall-Petch law. At 1200℃, a solid state reaction took place between the particles and the metal matrix, which allowed a partial loading transfer as commonly occurs in composites [97]. Some investigators revealed that heat treatment improved the bond strength of the coatings although there was a decrease in their hardness [56, 98]. After heat treatment at high temperature, $Ni(OH)_2$ in the coating was turned into Ni_2O_3 and NiO, which could wet the PSZ particles and increased the bonding strength between the PSZ and nickel. And the agglomeration of PSZ particles was sintered when heat-treated.

These are all beneficial to increase the wear resistance of the coating [99]. Similar results were found for the Ni-SiC composite films, in which the wear resistance improved about fifty times over that of a pure nickel sample, and it was attributed to the formation of a Ni_5Si_2 phase during heat treatment at 800℃ and 1000℃ [76, 100, 101].

2.2.2.8 Other Processing Factors

The nature of the substrate has a great influence on the electrocrystallization through the density of germination. Both cathodic polarization and impedance spectroscopy diagrams revealed that the electrochemical behaviours that characterized the silicon/metal interface classified the metallic interfaces into several groups, depending on conductivity [102]. Morphology and structural studies showed a decrease in the number of nuclei when a metallic layer was used. Nickel deposits on such layers have low adhesion. The adhesion loss was intensified with high internal stress when semiconductor or insulator substrates were used in microelectronic applications. Activation of the surface could be improved either by increasing activation time or by using a more concentrated solution. The latter solution, however, was not advisable for thin films. It would certainly be better to substitute a copper sputtered coating, which has shown a great number of nucleation sites in massive growth for nickel [102].

2.3 Electrodeposition under Different Shaped Waveforms

One of the advantages of electrolysis is that the reaction rate of a system can be easily controlled by applying an external current or voltage. Modern electronics has greatly enhanced this advantage by applying current or voltage as any function of time. Typical waveforms include galvanostatic pulse, potentiostatic pulses [103], square-wave pulse and other modified sine-wave pulses [104].

2.3.1 Pulse Electrodeposition

Pulse plating builds directly on the principles of single metal plating. Pulse plating has been widely applied in industry to synthesize coatings for various applications due to it advantages over direct current which include finer grain size, lower porosity, better adhesion, more uniform thickness distribution and enhanced properties [56, 75, 76, 105~107]. It is also an economical application to produce nanocrystalline materials Ni, Zn [108], Cu [109], Ni-SiC, Ni-Al_2O_3 [110], etc. These materials with grain size within $100\,nm$ are of considerable interest due to their unique and improved properties over their coarser-grained counterparts [64, 111].

The pulses can be either forward or reverse. A forward pulse can be considered to be the application of a cathodic current or voltage. Under these conditions, reduction at the cathode and oxidation at the anode will occur. The reverse pulse essentially reverses the current from cathodic to anodic. Under these conditions, dissolution of metal occurs at the cathode, and reduction of metal ions occurs at the anode. Pulse reverse plating can be employed to eliminate a fraction of plated metal thereby reducing the amount of dendrite growth, improving the thickness uniformity of the deposits layer, and increasing the particle deposit concentration [112~114]. During the anodic parts of reverse pulses, the hydrogen dissolved in the deposits will be anodically oxidized and be reduced to a lower content, and the anodic process is advantageous for convective diffusion of metal ions from the electrolyte to the surface of the cathode [115].

Normally, the pulse on-time affects the electrodeposition process on the depletion of cations at the cathode film, the thickness of the pulsating diffusion layer, hydrogen adsorption and evolution, and other adsorption processes. The pulse off-time has the effect of reducing hydrogen evolution reaction, which leads to the disappearance of the hydrogen gas cavities on the surface of the deposits.

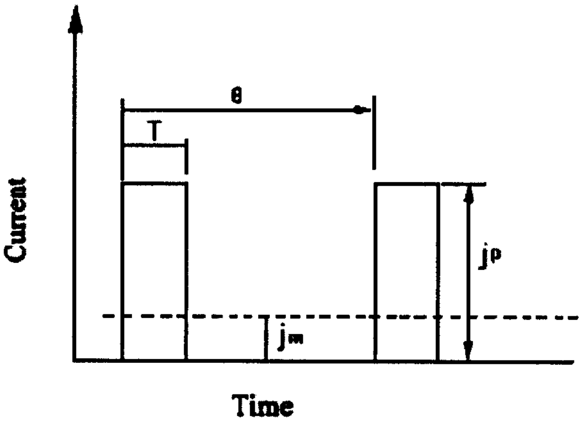

Figure 2.4 Schematic illustration of pulse plating parameters

2.3.1.1 Duty Cycle

The pulse electrodeposition process is known to be affected by its current parameters: pulse frequency, duty cycle, and peak current density [116, 117]. As shown in Figure 2.4, the relationship of these parameters determines the average current at a given peak current [118], and enables the pulse current technique to generate high instantaneous current density and hence very high potential on the cathode [118]. Changing the pulse parameters is more effective for obtaining the permissible pulse current density than stirring [119]. Moreover, pulse current changes the local current density more effectively as compared with direct current for the same amount of charge [120].

Among the current parameters, the duty cycle was reported to affect the deposit structure, grain size [121], phase distribution, alloy composition [122, 123], and the current efficiency [124, 125] due to its influence on the diffusion and mass transfer behaviour. Murali et al [126] found that the intensity of the preferential orientation (002) of the CdSe alloy increases with decreasing duty cycle. At the same average current density and deposition time, a maximum deposit thickness of WSe_2 was obtained at a duty cycle of 20% [127]. The pulse parameters were shown to affect not only the textures of the Zn-Fe deposits but also their phase constitutions at a constant average current density of 6 Adm^{-2} [128]. It was further reported that at a duty cycle of 50%, a smooth deposit surface of copper alloy with finest grain size was obtained [129, 130]. Although a number of researchers have examined the effect of duty cycle in electrodeposition of metals or alloys and found it to be significant, less work has been done on electro-codeposition of composites.

2.3.1.2 Pulse Frequency

Pulse frequency has been shown to have a significant influence on composition in bi- or ternary- alloys such as Mn/Mn-Zn, Co/Co-Ag, Mo/Ni-Cu-Mo [122, 131~133]. When the pulse frequency is low, a stationary state is achieved for mass transport during the on-time period, and the composition of the alloys can be easily obtained by the Levich equation [124]. Many researchers reported the dependence of pulse frequency on deposit hardness. For pure nickel, it was found that the deposit hardness decreased when the frequency reduced from 1000 to 100Hz. A relative constant hardness value was observed at the frequencies between 10 and 100Hz [116, 117]. But in most alloys, the hardness was found to decrease with increasing pulse frequency.

2.3.1.3 Electrical Double Layer---Capacitive Effects

The electrode behaves as a capacitor with a resistance in parallel. When pulse current is applied in the electrodeposition system, the capacitive effects will significantly influence the current efficiency, and affect the amplitude of the pulse and hence the energy of the electrodeposition reaction. The charging and discharging of the electrical double layer at the electrode requires certain times, which depends on the current density and on the physico-chemical parameters of the system. As a result, the charging time will be much shorter than the pulse duration, and the time required for discharge of the double layer will be much shorter than the off-time between two pulses [134]. Otherwise, the charging and discharging times of the double layer will be much longer than the on-time and off-time of the pulse respectively, and the pulse current is virtually a direct current, and losing the potential benefits of pulse plating in terms of changes in the electrodeposit structure [135].

Puippe and Ibl [134] calculated charging and discharging times of the double layer as a function of pulse current parameters at standard temperature.

$$t_{charge} = \frac{17}{i_p}$$

$$t_{discharge} = \frac{120}{i_p} \qquad (2.30)$$

Since the pulse current density is usually much higher than the exchange current density in pulse electrodeposition, the equations above can be used to estimate the double layer charging and discharging time.

Figure 2.5 illustrates the effects of double layer capacitance on the pulsing action. At the very beginning of the pulse, the whole current is used to charge the double layer, and hence no deposition takes place (faradaic current is zero). However, as the electrical layer becomes charged, the potential becomes more negative, and the faradaic current will increase eventually and reach the peak current. Finally the pulse terminates, and the electrical layer discharges. The importance of the capacitance nature of the electrical double layer is to ensure that the current pulses are not too severely distorted.

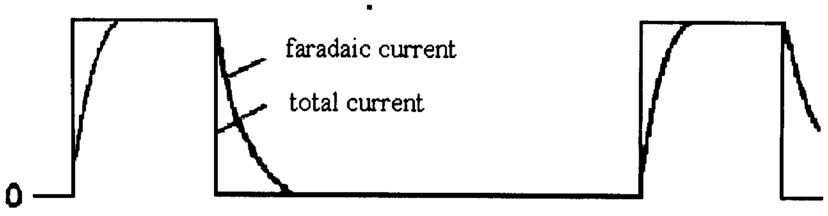

Figure 2.5 Schematic diagram showing the influence of the capacitance of the electrical double layer on the pulse current

2.3.1.4 Cathode Diffusion Layer---Mass Transport Effects

One of the major differences that arises from pulse plating is the existence of two distinct cathodic diffusion layers. Figure 2.6 illustrates the concentration profile for the two diffusion layers in pulse deposition.

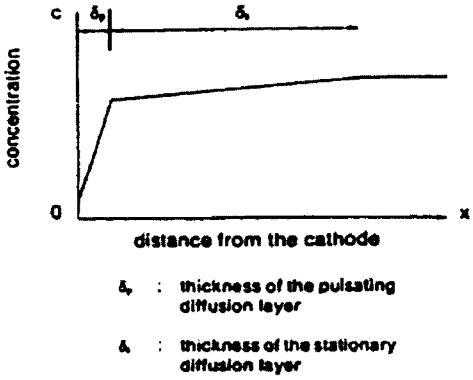

Figure 2.6 Schematic diagram of the concentration profile for the two diffusion layers in pulse deposition

In the immediate vicinity of the cathode the concentration pulsates with the frequency of the pulsating current. If the duration of the pulse is short, the diffusion layer changes too rapidly to extend into the solution and does not influence the convection region. Therefore a concentration gradient builds up in the bulk of the electrolyte. The thickness of this diffusion layer corresponds to that which would be established in direct current electrolysis. In the outer diffusion layer, cations are supplied towards the cathode during the off-time and this diffusion layer is essentially stationary [138].

The two distinct diffusion layers are related to two kinds of limitations. The depletion of the metal ions concentration in the pulsating diffusion layer limits the current density, and the depletion of concentration in the outer diffusion layer limits the average current density. Since the concentration gradient in the pulsating diffusion layer can be very high, and increases with shorter pulse length, the pulse current density can reach extremely high values, e.g. up to 10000 times the usual direct current values, without decrease of current efficiency.

To sum up, the first limitation due to the mass transport effect is that the pulse duration should not exceed its maximum, while the second is that the maximum average current density cannot exceed the DC limiting current density. It is important to emphasize that the average current density in pulse plating cannot exceed the limiting current density, as in DC plating. However, the practical current density, which is below the diffusion limiting current density, can sometimes be increased in pulse plating as compared to DC while keeping a constant deposit quality. The increase of current density will result in the improvement of deposit structures, and also the deposit properties.

2.3.1.5 Crystallization

Crystallization is a very important step in electrogrowth for it directly influences the structure of the deposits and their properties. As discussed in Chapter 2.2, new nuclei creation and crystal growth are in competition and can be influenced by current density, additives, temperature and other factors. High surface diffusion rates, low concentration of ions, and low overpotential are factors enhancing crystal growth, while conversely low surface diffusion rates, high concentration of ions, and high overpotential on the surface enhance the creation of new nuclei. In pulse plating, since the pulsed current density is usually considerably higher than the corresponding direct current density, higher overpotential and higher concentration of ions will occur during pulse deposition than during direct current deposition to result in an increased nucleation rate and therefore a finer grained structure.

Moreover, the plating bath is greatly influenced by adsorbed species at the electrode, such as organic brighteners, stress reducers and many other additives present in the bath. The adsorption isotherm of these molecules is a function of the potential, and therefore the nature of adsorbed species can be continuously modified by modulating the current. For given pulse parameters, adsorption or desorption of a species present in the electrolyte will influence surface diffusion in a different way than in direct current, thus leading to different crystallization mechanisms and therefore to different physical properties of the deposit.

Another phenomenon that is different from direct current plating is that recrystallization occurs during the off-time period. Small grains are thermodynamically less stable than large ones because of high surface energy. And in relaxation time, small grains tend to recrystallize, depending on which adsorbed species is being used.

Apart from the crystallization, when a pulse current is applied with very high pulse current densities, the concentration of ions at the interface is so high during the pulse that there is no time for ordering them into a crystal lattice, and this results in amorphous metal or alloys.

2.3.1.6 Kinetics

The electrodeposition rate can be considerably increased during the on-time of one pulse current as compared to DC. The kinetics of competitive reactions will therefore play a relevant role in the rate of competitive reactions. In metal deposition accompanied by hydrogen evolution, if the slope of polarization curves for metal deposition increases faster than that for hydrogen evolution, the current efficiency for metal deposition will usually increase as pulse current density increases.

However, adsorption and desorption effects can lead to unexpected trends in current efficiency according to considerations of steady state kinetics. For example, when rhenium is reduced from a heptavalent ion, its reduction potential is much more negative than that of hydrogen ions, and the current efficiency for rhenium is thus usually less than 10 percent. Nevertheless, in pulse plating with very short pulses, the current efficiency increases up to 60 percent. The reason is that monovalent rhenium is adsorbed at the electrode during the off-time. If the on-time and pulse current density correspond to the columbic charge needed for its reduction, the current efficiency for rhenium is substantially increased.

The kinetics of nickel electrodeposition has been investigated through impedance measurements [136, 137]. An inductive feature is commonly observed in sulfate, chloride and Watt's electrolytes. It is generally concluded that a two-reaction mechanism occurs in nickel deposition and probably involves reactions relating to the existence of intermediate adions Ni^{+}_{ads} more or less complex or solvated. The difference in the electrode polarization at a given current density between sulfate and chloride electrolytes is explained on the basis of the nickel ions' activities. The nickel activity coefficients are lower in sulfate solutions than in chloride solutions.

2.3.2 Effect of Current Waveform on Electrodeposition

Figure 2.7 shows examples of some pulse waveforms. Each waveform has its particular advantages and applications. Square waveforms can be generated at very high frequencies (up to 10kHz) and are often used when a high frequency plating cycle is desired. Asymmetric sine waves, and periodic reverse square waves can only operate at low frequencies (50~60Hz). However, they are advantageous in that they allow for faster replenishment of metal ions at the cathode/electrolyte interface when the cathode becomes the anode for a short period of time during the reverse pulse. The split sine wave produces only a cathodic current like the square wave. This is generally used for situations in which the electroplated metal will readily dissolve in the electrolyte. Thus, the application of a continuous cathodic current/voltage prevents excessive metal dissolution [138]. The four waveforms can be easily obtained.

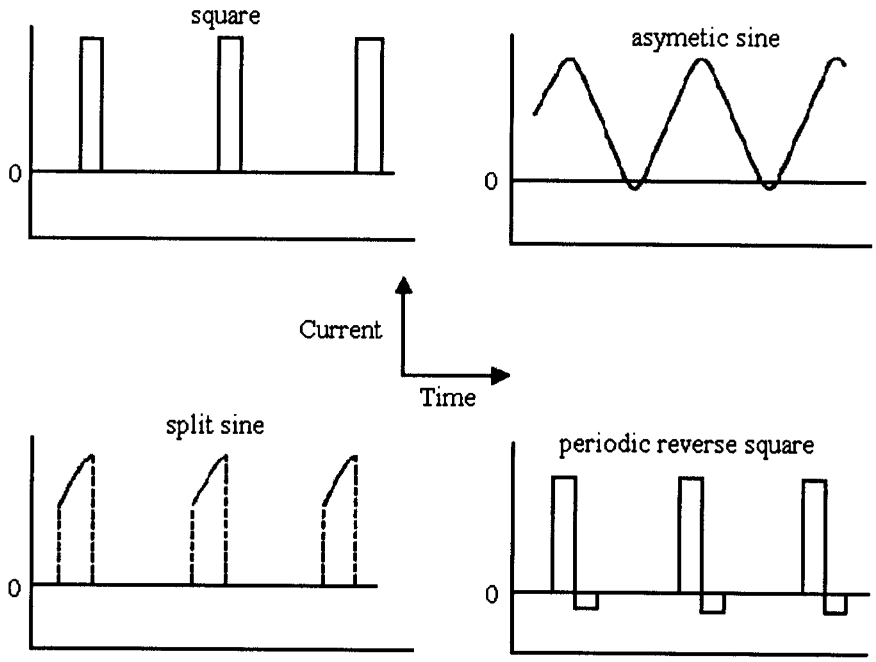

Figure 2.7 Pulse waveforms usually used in electrodeposition

Puippe [139] gave an example of current waveform which allows for superior control of the deposition process and subsequent layer quality. As can be seen from Figure 2.8, the peak current density is not kept constant, nor is the off- and on-time.

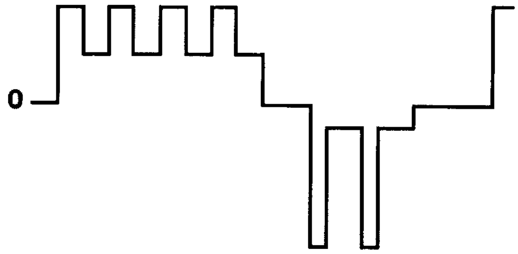

Figure 2.8 An example of current waveform applied by Puippe

In the past few years, different shaped current waveforms were investigated. The effects of different types of waveforms on the surface finish of nickel electroforms has shown that the conventional rectangular waveform is far from ideal for producing deposits. A mathematical model has been established for formulating the effects of different types of waveforms on surface finishing in pulse current electroforming of nickel. The model describes the change of concentration profile of electroactive ions, micro-current distribution and the rate of protrusion growth at cathodic surfaces. The theoretical predictions were compared with the experimental results, and a maximum discrepancy of 10% on surface roughness values was found between them. Both theoretical predictions and experimental results showed that the quality of the electroforms, in terms of surface roughness improvement, influenced by the types of waveforms were in the order of ramp-down waveform > triangular waveform > ramp-up waveform > rectangular waveform, all with relaxation time, where the ratio of the height of a protrusion to the initial height of that protrusion (h/h_0) could be written as:

$$\frac{h}{h_0} = \frac{\delta^3 \rho}{2MD(c_e - c_0)} \{-W(\beta) \cdot [2 + W(\beta)] - W(\gamma) \cdot [2 - W(\gamma)]\} \tag{2.31}$$

where

$$\beta = \frac{-1}{\delta} \tag{2.32}$$

$$\gamma = \frac{-1}{\delta} \exp\left[\frac{m\theta MD(c_e - c_0)}{\rho^2 (r+1)}\right] \tag{2.33}$$

And for different types of waveforms, the change of concentration profile of electroactive ions could be described by the following equations:

$$c_e - c_0 = \frac{2D}{\delta} \sum_{n=1}^{\infty} \left[\exp(-p^2 at) \int_0 \exp(p^2 au) i(u) du\right] \tag{2.34}$$

Another mathematical model was also established for formulating the effects of different types of waveforms on 3-dimentional electrocrystallization of nickel electroforms. The model described how the different types of waveforms influenced the rate of 3-dimensional nucleation, the rate of 3-dimentional step growth via surface diffusion path, and the rate of 3-dimentional step growth via direct transfer path at the cathodic surface.

The 3-dimensional nucleation rate was given by

$$J = \omega_{a,c} \Gamma N_0 \exp\left[-\frac{4}{27} B \frac{v_m^2 \sigma^3 \phi_{cs}}{(ze\eta)^2 kT}\right] \tag{2.35}$$

And the rate of advancement of 3-dimensional steps of growth via surface diffusion path was

$$J_{SD} = \frac{zFD(c_e - c_0)}{q_{mon} \lambda} \tag{2.36}$$

And the nucleation rate via direct transfer path at the cathodic surface was

$$J_{DT} = \frac{i_0 \kappa}{q_{mon}} \left[\exp\left(\frac{(1-\alpha) ze\eta}{kT} \right) - \exp\left(\frac{-\alpha(ze\eta)}{kT} \right) \right] \tag{2.37}$$

When grain size and hardness among waveforms were compared, both the most fine-grained structure and the highest hardness value were found when a ramp-down waveform was employed. The experimental results also showed that, compared with the conventional rectangular waveform, the hardness value could be improved by about 28% when a ramp-down waveform was used [140~145].

Chapter 2.4 Magnetoelectrolysis

2.4.1 The Effects of Magnetic Fields

Magnetoelectrolysis is the term used when describing the effect of an applied magnetic field on electrochemical processes at an electrode/solution interface. Research into the influence of a magnetic field on electrochemical reactions has been ongoing for most of the past century. Improved mass transport in cells, better deposit quality and control of corrosion are just some of the effects that can be promoted by the application of magnetic fields in electrochemical processes. However, much of the published data on the subject is characterized by apparent contradictions and lack of reproducibility, and no mechanism which can quantitatively account for all the observed effects has been established.

2.4.1.1 Electrochemical Behaviour

An external magnetic field produces various effects on electrochemical characteristics, and it has been suggested that magnetic fields have kinetic effects by inducing an overpotential, by decreasing the hydration number of cations, or by modifying adsorption at the interface [146~151]. When mass transport is controlling mode (limiting current conditions), the effect of applying a magnetic field during electrolysis is strongest due to the interactions of the field with the convective diffusion layer at the electrodes [165].

The mass transport due to the magnetic field effect can be evaluated by measuring the limiting current of various electrochemical processes. Mohanta and Fahidy [151] observed that the cathodic limiting current of copper electrodeposition increased by 30% in an external magnetic field of 0.7T. And the increasing limiting current was also reported in deposition of Ni-Fe alloy at magnetic fields ranging from 0T to 0.9T [152], and in copper deposition from 0T to 0.178T [153]. Several semi-empirical expressions of the dependence of limiting current density versus magnetic field were derived, and the limiting current density was found to increase with the increase in magnetic flux.

The complex impedance spectroscopy and radiotracer techniques were used to illustrate the effects of the magnetic field on the electrodeposition mechanism. The magnitude of the capacitive loop, which characterized the charge-transfer kinetics process, increased with **B**. However, the product of the charge transfer resistance and the electrolysis current was roughly constant in the whole **B** range. Hence, the magnetic field did not affect the charge transfer coefficient at the cathode surface [155, 156]. And the measurement of the kinetics by radioelements for the reaction $Cu^{2+} + 2e^{-} \Leftrightarrow Cu$ has also shown that the magnetic field has no influence on charge-transfer processes and on the exchange current [154]. Brillas et al [156] found, in the low frequency range, a complex reactional mechanism of electrodeposition involving several adsorption processes, and each of them being likely to be **B** influenced. As a result, they deduced that **B** was capable of influencing interfacial processes rather than transport, such as the adsorption kinetics, and the reduction of the diffusion layer thickness [156].

The codeposition behavior was less been reported but it is generally believed there exists a magnetically induced change in the structure of the adsorbed ionic layer on the particles. And the codeposition process of inert particles and metal could be controlled by regulating the magnetic flux. Nevertheless, more research is required to enable us better to understand the effects of magnetic fields on the distribution of particles and the mechanisms of electro-codeposition.

2.4.1.2 Cathodic Deposit Morphology Effects

Applying a magnetic field during electrodeposition changes the crystallization behaviour of the metal from the electrolyte. Such an effect is most pronounced at low current densities, where it can be considered that the influence of a magnetic field is larger than that of the electric field [153, 164]. The effect of magnetic fields on the texture of nickel deposits was investigated with current densities ranging from $2.5\,\mathrm{Adm^{-2}}$ to $5\,\mathrm{Adm^{-2}}$. It was found that the intensity of the orientation of (200) plane increased with the applied magnetic flux density up to 0.01T at the current density of $2.5\,\mathrm{Adm^{-2}}$. But the magnetic fields had only a slight or no effect on the texture coefficient at a higher current density of $5\,\mathrm{Adm^{-2}}$ [156]. Chiba et al. [151] observed minor variations in the quality of the preferred orientations of nickel electrodeposits at high current densities, whereas the magnetic field effect was more pronounced at low current densities. However, Yang [157] found that an imposed magnetic field of 0.54T at a low current density of $1.25\,\mathrm{Adm^{-2}}$ had no significant effect on the preferred orientations of Ni, Fe, and Co deposits. Ref. [156] also found that a magnetic field of 0.9T in a two-electrode cell exerted only a limited effect on nickel grain orientation. Contradictory observations on texture coefficient can be explained using Danilyuk's theory [153] that some values of the magnetic field accelerate the electrodeposition reaction, whereas others cause its inhibition. The presence of some organic inhibitor was also found to affect the mass transport enhancement of hydrogen ions, and therefore modify the orientation of the electrodeposits [158, 159].

Most of the reports reveal that the magnetic fields would improve the surface morphology of the deposit coating. Devos et al. [160] reported that a uniform magnetic field close to 1T parallel to the cathode surface changed the morphology of nickel deposited at constant cathodic potentials in a Watt's solution. The surface morphology of iron grains was angular with a large size distribution without the external magnetic field, but it changed to roundish grains with smother surface in magnetic fields [160, 161]. Nickel-iron deposits were also modified by an imposed magnetic field, and resulted in a smoother deposit surface with a uniform microstructure [150]. The magneto-induced convective flow of the electrolytic solution resulted in reduction or suppression of the mass transport, and consequently in the diffusion control. Thus the dendritic growth of zinc or lead, in some cases, could be totally inhibited to give smooth deposits, with an increase of efficiency in the metal deposition.

The relative strength of the magnetic effect is also strongly dependent on the mutual positions of the electrodes and the direction of the magnetic and gravity fields. It was obvious that mass transport was enhanced more when the electrodes were slightly inclined to the horizontal than to the vertical plane [165]. A series of experiments were conducted by Chiba et al [146, 150] to illustrate the magnetic effects on the nickel, copper, tin and other metal deposition. The magnetic poles were disposed as cathode side N and the anode side S. The results showed that the magnetic fields have influence on the current efficiency, texture coefficients, and anodic dissolution. Olivier et al [162] applied the magnetic field vector parallel to the surface of working electrode and found the existence of two diffusion processes. Mastushima et al found that the preferred orientation and surface morphology in iron electrodeposition were influenced by a parallel magnetic field vector. Brillas et al [156] used both set-ups to investigate the effects of magnetic fields on nickel electrowinning, and they found the magnetic field favoured the formation of grains with better defined geometrical shape. Niolic et al [163, 147] also studied both directions of magnetic fields on the nickel deposits, and they proposed that the resistance of deposits would change in the perpendicular field, which is based on the ferromagnetic characteristics of nickel. When the magnetic field was superimposed vertically to the copper substrate plane, iron crystal grains became roundish and uniform, which was due to the microscopic magnetohydrodynamic convection generated around the grains. Whereas with the magnetic field parallel to the substrate, the grains became relatively unchanged [164].

In spite of these contradictory results, it appears that nickel electrodeposition from a concentrated electrolyte is a good experimental system for the identification of the specific effects of a magnetic field on electrocrystallization, in view of the considerable amount of knowledge which has been accumulated. It is known that the overall deposition rate is governed by interfacial reactions, and nickel ions transport thus has practically no influence on the deposition process. Moreover, the specific structures and surface morphologies of all textures are identified. It is demonstrated that the direction of preferential growth is determined by a competitive adsorption of various species (especially hydrogen species) on the crystal faces of the growing nickel crystals. Therefore, the texture axis as well as the microstructure of nickel coatings are very sensitive to any modification of the state of adsorption, such as the addition of small quantities of organic compounds, or use of pulsed currents. And the nickel electrodeposition is considered to be a sensitive test for the detection of magnetic field effects.

2.4.2 Magnetohydrodynamics

The magnetic field is a powerful scientific tool for researching on the mass transport process and reaction kinetics (cathodic metal deposition and anodic metal dissolution) [165], because the influences of a magnetic field on the dissolution of metals and on electrochemical reactions are distinct [146]. It is generally agreed that the effects of magnetic fields are attributed to the magnetohydrodynamic effect, which was induced by the Lorentz force. The total force on a charged particle (electron, ion) moving in an electromagnetic field is

$$F = q(E + \upsilon \times B) \tag{2.38}$$

where E is the sum of the electric and electrostatic fields. Since the Lorentz force is capable of producing movement of charged particles, a magnetic field applied during electrolysis gives rise to convection of the electrolyte.

Based on experimental results, some empirical equations were developed to describe the relationship between mass transport limiting current, i_B and magnetic field, **B**, in electrodeposition of metals and alloys [165, 166]. Aogaki et al. showed that i_B increased with increasing **B**. An empirical equation describing the effects of a strong magnetic field on the mass transport limiting current for electrodeposition on disk platinum electrodes using chronoamperometry was developed by Legeai et al. [166]. The limiting current under a magnetic field could be expressed as a function of parameters that control the mass transport phenomenon

$$i_B = KC^{4/3}Dd^{5/3}\upsilon^{-2/3}\varepsilon^{-7/4}B^{1/3}n \tag{2.39}$$

where C represents the electroactive species concentration, D the diffusion coefficient of the electroactive species, d the working electrode diameter, υ the kinetic viscosity of the electrolyte, ε the dielectric constant of the solution, **B** the magnetic field strength, n the number of electrons involved in the redox process and K the proportionality constant.

Kinetic effects can be modeled by defining a magnetically induced potential difference. The interpretation of magnetoelectrolysis came from Kelly, who in 1977 showed that the rate of corrosion of titanium electrodes in $TiSO_4$ solution increased by a factor of 2.5 by the application of a 2T field. He used Butler-Volmer kinetics to describe the interfacial potential difference at the electrode/solution interface, and analyzed the total anodic and cathodic polarization [167]. A magneto-induced potential difference was proposed to explain the reduction of the diffusion layer and the acceleration of the charge transfer reaction.

$$i = kFc\exp\left(\frac{-\alpha nF\Delta_{M\phi S}}{RT}\right) \tag{2.40}$$

where i is the steady-state current density, α the symmetry factor, n the charge-transfer number, $\Delta_{M\phi S}$ the potential difference between the metal phase and a point just inside the electrolyte phase, and other symbols carrying their conventional significance.

Other authors [168], however, believed that the force due to a concentration gradient of magnetic ion was the driving force for the effects on the mass transport. The effects of magnetic fields on both heterogeneous electron-transfer kinetics and electrochemical equilibrium have proved more controversial, which was partly due to the difficulty of eliminating indirect mass transport effects.

Considering the hydrodynamics in magnetoelectrolysis, the vector and scalar υ and B fields are the most important variables, and j and the sum of the electric and electrostatic field E ($=E_I+E_s$) can be deduced. Fundamental equations in magnetohydrodynamics are as follows:

$$j = \sigma(E + v \times B) \tag{2.41}$$

$$curl\frac{B}{\mu} = j \tag{2.42}$$

$$-\frac{\partial\rho}{\partial t} = div(\rho v) \tag{2.43}$$

$$\rho\frac{\partial\upsilon}{\partial t}+(\upsilon\cdot grad)\upsilon+grad\rho=j\times B+\rho\upsilon\nabla^{2}\upsilon+\rho F \qquad (2.44)$$

$$E\cdot j=\frac{j^{2}}{\sigma}-j\cdot(\upsilon\times B) \qquad (2.45)$$

$$\frac{d}{dt}(\frac{\omega}{\rho})-\frac{\omega}{\rho}\cdot grad\upsilon=\frac{1}{\rho}curl\left(\frac{j\times B}{\rho}\right) \qquad (2.46)$$

$$j\times B=(B\cdot grad)\frac{B}{\mu}-grad\frac{B^{2}}{2\mu} \qquad (2.47)$$

As a result of the interactions of the field within the convective diffusion layer at the electrodes, the effect of applying a magnetic field during electrolysis is strongest when mass transport is the controlling mode (limiting current conditions). Using laser interferometry techniques, this effect can be made visible [166]. The electronic structure of reaction molecules and intermediates is the determining factor for the interaction with the field.

Chapter 3 Effect of Different Shaped Current Waveforms on Electrodeposition of Ni-SiC Composites

3.1 Introduction

Technological development in the field of composite materials has proved that the embedding of inert solid particles, such as SiO_2, Al_2O_3, SiC, WC etc. [169~171], in metallic matrices can significantly improve their mechanical, tribological, anti-corrosion and anti-oxidation properties [43, 54, 172]. In particular, during recent years, Ni-SiC composites have been widely investigated and successfully commercialized in the automotive and aerospace industry as a result of their improved mechanical and tribological properties. Recently, the codeposition of ultrafine or nanosized particles with metals has attracted much research interest [44, 56, 57, 173], as they do not only have enhanced mechanical properties, but also have potential applications in microelectrical mechanical systems. It has been demonstrated that the ultrafine Ni-SiC has a smoother surface and better bonding between SiC and Ni than that of coarse Ni-SiC composite. It is well known that the main parameters affecting the structure and properties of electrocodeposited composites include the solution electrolysis condition, and the current condition. A number of additives or surfactants such as $Na_3Co(NO_2)_6$ and cetltrimethylammonuim bromide, have been successfully used either to promote the codeposition process or to enhance the distribution of the particles [14]. Relatively less research work has been done to examine the effect of current condition [143

~146], in particular, waveform on the codeposition behaviour of the composite, though previous investigations of the authors have shown that the ramp and triangular shaped waveforms, both with relaxation time, have a higher quality of surface roughness than rectangular and ramp and triangular sawtooth waveforms, while the highest hardness value and the finest grain size were obtained using a ramp-down waveform with relaxation time.

Although the codeposition process has been developed for a long time [13, 21, 41, 174], the codeposition mechanisms are still not fully understood. Among the theoretical models for the composite electrocodeposition process, Guglielmi is the first to propose a successive two-step adsorption mechanism, and to explain the relationship between the volume fraction of codeposited particles and the volume percentage of particles suspended in the plating bath. The model has been verified by experiments in codeposition of Ni-SiC composites [19, 92]. Recently, it has been further reported by Wang and Wei [110] that the two-step codeposition mechanism is valid in the ultrafine Ni-SiC composite plating. In this part, an ultrafine Ni-SiC composite will be codeposited under different shaped waveforms, and the deposition behaviour of the composite will be theoretically analyzed based on Guglielmi’s model.

3.2 Theoretical Consideration

3.2.1 The Classic Guglielmi’s model

Guglielmi’s model proposed that the adsorbed charge, which is manifested by the zeta potential, is the principal factor in determining the feasibility of the codeposition. The model is based on two consecutive adsorption steps, the first step, being the transport of a layer of loosely adsorbed particles with a rather high coverage to the Helmholtz's double layer by mechanical agitation. The second step is the transport of particles charged in the high potential gradient to the cathode surface by electrophoretic attraction and the subsequent adsorption of the particles to the cathode surface by the Coulomb force which exists between particles and adsorbed anions to produce a strong adsorption of the particles onto the electrode.

Based on Langmuir's adsorption isotherm theory and Faraday's laws; Guglielmi deduced the following codeposition model:

$$\frac{\alpha}{1-\alpha} = \frac{nFd\upsilon_0}{Wi_0} \cdot e^{(B-A)\eta} \cdot \frac{kC}{1+kC} \tag{3.1}$$

Guglielmi has plotted $\frac{C}{\alpha}$ to C, and noted they are in a linear relationship at a given overpotential. The slope of the straight line (with an angle of ϕ) is given by

$$tg\phi = \frac{Wi_0}{nFd\upsilon_0} \cdot e^{(A-B)\eta} \tag{3.2}$$

When a high voltage is applied to the electrolyte, the surface overpotential can be described by the Tafel equation, such that: $i/i_0 \approx e^{A\eta}$. Eq. (3.2) can be rewritten as

$$\log tg\phi = \log \frac{Wi_0^{\ B/A}}{nFd\upsilon_0} + \left(1 - B/A\right)\log i \tag{3.3}$$

From these equations, the parameters *W*, i_0, *n*, *F*, *d*, *A* and *i* can be determined by the process of metal deposition; *B* and *k* are related to the particle deposition. As for the SiC particles, 1/*k* is equal to 0.12, *B*=1.51*A* [174]. The percentage of particle embedded in the deposit is related to the value of υ_0, which is dependent on the rate of reduction of ions adsorbed on the inert particles.

3.2.2 Current Waveforms

Figure 3.1 shows the four simple shaped waveforms to be investigated in the part. The parameters related to the deposition are on-time, t_{on} and off-time (or relaxation time), t_{off}. If $t_{off} = m \cdot t_{on}$, the cycle $T=t_{on}+t_{off}=(m+1)t_{on}$. The current is a function of t, as

$$I(t) = \begin{cases} i(t) & \Delta t = t_{on} \\ 0 & \Delta t = t_{off} \end{cases} \tag{3.4}$$

For a duty cycle, T, a Fourier series can be used to represent a waveform

$$\begin{aligned} I(t) &= \frac{a_0}{2} + \sum_{n=1}^{\infty}\left(a_n \cos\frac{n\pi t}{T} + b_n \sin\frac{n\pi t}{T} \right) \\ a_0 &= \frac{1}{T}\int_0^T i(t)dt \\ a_n &= \frac{1}{T}\int_0^T i(t)\cos\frac{n\pi t}{T}dt \\ b_n &= \frac{1}{T}\int_0^T i(t)\sin\frac{n\pi t}{T}dt \\ n &= 1,2,3...... \end{aligned} \tag{3.5}$$

It is obvious to note that the value of average current density I_{aver} is related to the duty cycle. When $t_{on}<<t_{off}$, $a_0=0$, $I_{aver}=0$. When $m=1$, $t_{on}=t_{off}$, I_{aver} is half of the peak current density i_p.

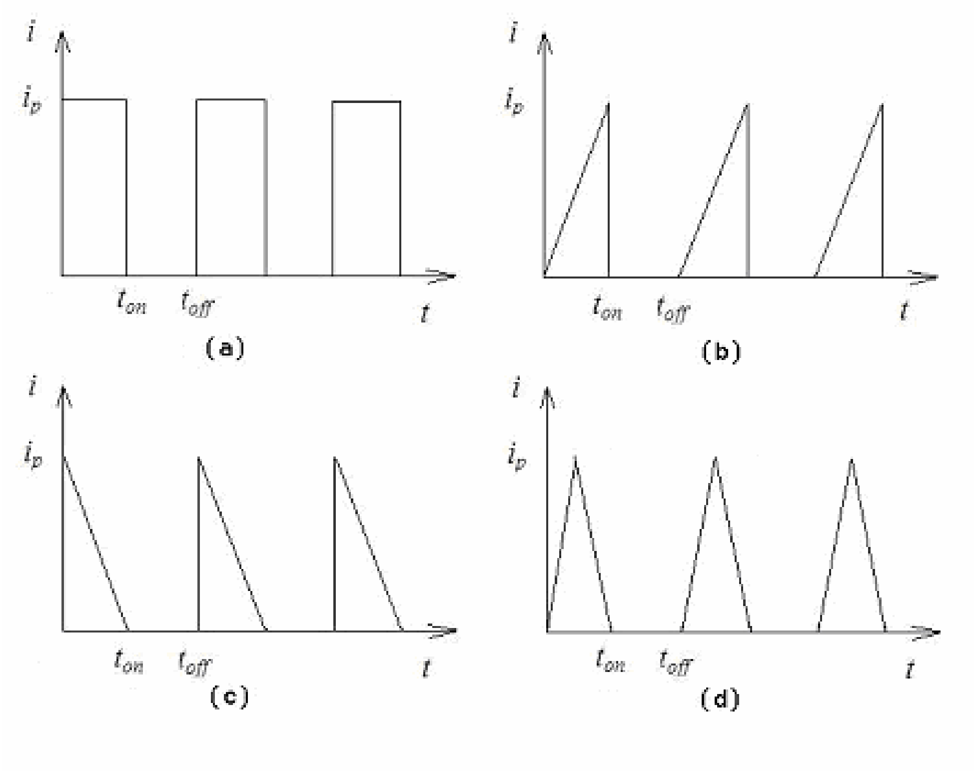

Figure 3.1 Different types of shaped waveform: (a) rectangular waveform with relaxation time; (b) ramp-up waveform with relaxation time; (c) ramp-down waveform with relaxation time; (d) triangular waveform with relaxation time

The four simple waveforms: rectangular waveform with relaxation time (I_{rec}); ramp-up waveform with relaxation time (I_{rup}); ramp-down waveform with relaxation time (I_{rdn}); triangular waveform with relaxation time (I_{tri}) can be described using the Fourier series as follows:

$$I_{rec}\left(t\right) = \frac{i_p}{m+1} + \sum_{n=1}^{\infty}\left\{\frac{i_p}{n\pi}\cdot\sin\left(\frac{2n\pi}{m+1}\right)\cos\left(\frac{2n\pi}{T}t\right) + \frac{2i_p}{n\pi}\cdot\sin^2\left(\frac{n\pi}{m+1}\right)\cdot\sin\left(\frac{2n\pi}{T}t\right)\right\} \quad (3.6)$$

$$I_{rup}(t)=\frac{i_p}{2(m+1)}+\sum_{n=1}^{\infty}\left\{\frac{i_p\left[-(m+1)\cdot\sin^2(\frac{n\pi}{m+1})+n\pi\sin\left(\frac{2n\pi}{m+1}\right)\right]}{\pi^2n^2}\cos\left(\frac{2n\pi}{T}t\right)+\frac{i_p\left[(m+1)\cdot\sin(\frac{n\pi}{m+1})-2n\pi\cos(\frac{2n\pi}{m+1})\right]}{2n^2\pi^2}\cdot\sin\left(\frac{2n\pi}{T}t\right)\right\} \quad (3.7)$$

$$I_{rdn}(t)=\frac{i_p}{2(m+1)}+\sum_{n=1}^{\infty}\left\{\frac{i_p(m+1)\cdot\sin^2(\frac{n\pi}{m+1})}{\pi^2n^2}\cos\left(\frac{2n\pi}{T}t\right)+\frac{i_p(m+1)\cdot\sin(\frac{2n\pi}{m+1})-2n\pi\cos(\frac{2n\pi}{m+1})}{2n^2\pi^2}\cdot\sin\left(\frac{2n\pi}{T}t\right)\right\} \quad (3.8)$$

$$I_{tri}(t)=\frac{i_p}{2(m+1)}+\sum_{n=1}^{\infty}\left\{\frac{2i_p(m+1)\cdot\left[\cos(\frac{n\pi}{m+1})-\cos^2(\frac{n\pi}{m+1})\right]}{\pi^2n^2}\cos\left(\frac{2n\pi}{T}t\right)+\frac{2i_p(m+1)\cdot\left[\sin(\frac{2n\pi}{m+1})-\sin(\frac{2n\pi}{m+1})\cos(\frac{2n\pi}{m+1})\right]}{n^2\pi^2}\cdot\sin\left(\frac{2n\pi}{T}t\right)\right\} \quad (3.9)$$

and are illustrated in Figure 3.2 for a i_p of 5Adm^{-2}

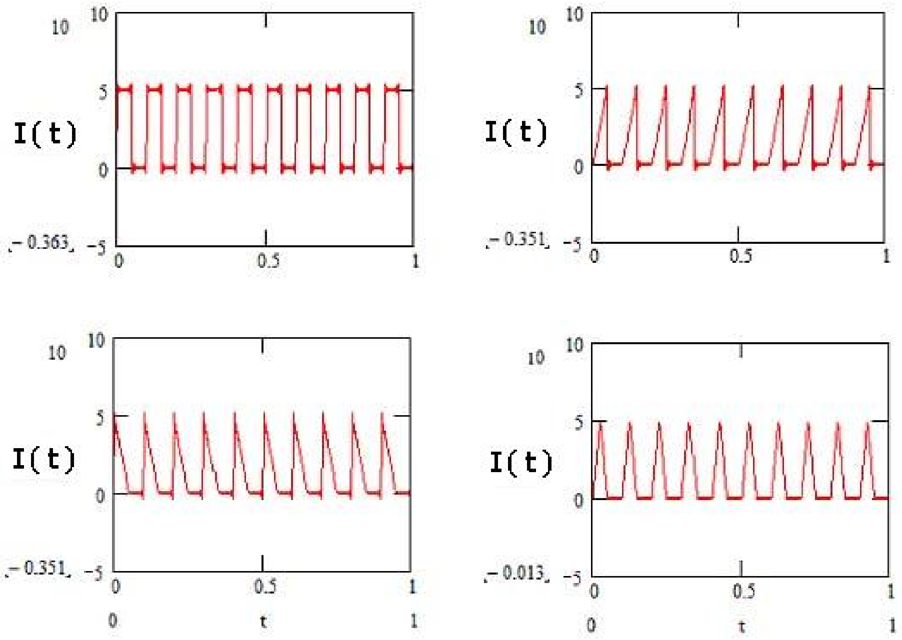

Figure 3.2 The simulation of different waveforms (i_p =5 Adm^{-2})

3.2.3 Theoretical Volume Fraction of Particles

Eq. (3.3) is applicable only when the current remains constant during electrolysis. In order to apply the same to waveforms with arbitrary shape, it is now assumed that a waveform consists of an infinite number of very short rectangular pulse currents as shown in Figure 3.3, where the currents i_1, i_2, i_3, corresponding to

α_1, α_2, α_3, etc., act successively. α_1 is obtained from $t=0$ to $t=t_1$, α_2 is obtained from t_1 to t_2, and α_3 is obtained from t_2 to t_3, etc.

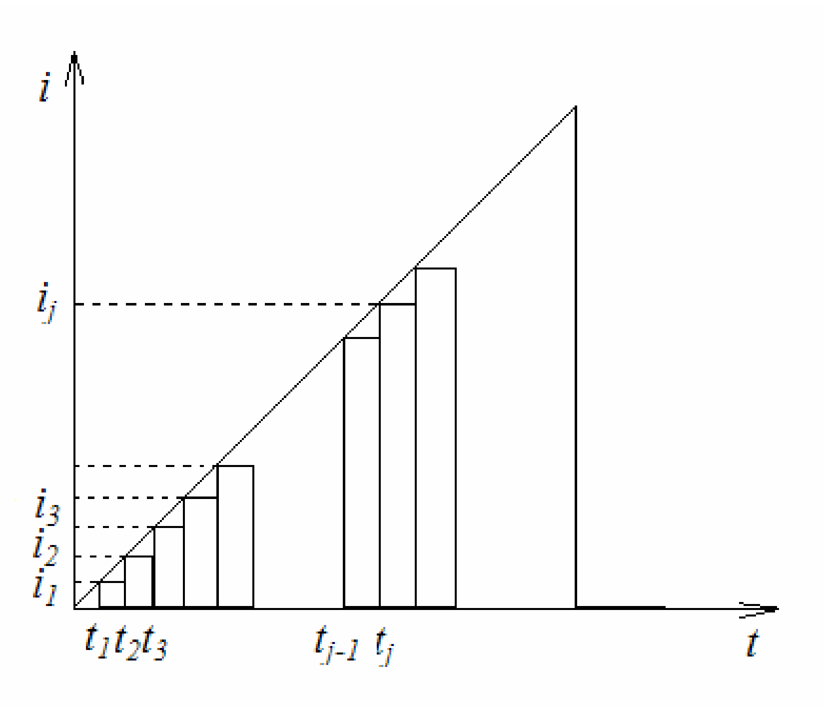

Figure 3.3 Schematic diagram of integration of the ramp-up waveform with relaxation time

Generally, in the period of $t_{j-1} < t < t_j$, the volume fraction of SiC particle deposited in the substrate is

$$\alpha_j = \frac{dV_p/dt}{dV/dt} = \frac{KC}{1+KC} \cdot \frac{nFd\upsilon_0}{Wi_0^{B/A}} \cdot i_j^{(B/A-1)} \tag{3.10}$$

The SiC volume fraction increases with current density. If the difference between any two successive constant currents is infinitely small, and the number of short rectangular pulse currents is infinite, the volume fraction of SiC becomes a differential, and summation with respect to the end of a duty becomes integration. Then the whole volume fraction of SiC in one duty cycle can be calculated as:

$$\alpha = \frac{\sum_{n=1}^{\infty} \alpha_n t_n}{T} = \frac{1}{T}\int_0^T \alpha_n dt \tag{3.11}$$

The volume fraction of SiC produced by a rectangular waveform with relaxation time in a period of *t* becomes:

$$\alpha_{rec} = \frac{1}{t}\int_0^t \frac{kC}{1+kC}\cdot\frac{nFd\upsilon_0}{Wi_0^{B/A}}\left[I_{rec}(t)\right]^{(B/A-1)} dt \tag{3.12}$$

Similarly, for the ramp-up, ramp-down and triangular waveforms with relaxation time, the volume fractions of SiC in the period of t are:

$$\alpha_{rup} = \frac{1}{t}\int_0^t \frac{kC}{1+kC}\cdot\frac{nFd\upsilon_0}{Wi_0^{B/A}}\left[I_{rup}(t)\right]^{(B/A-1)} dt \tag{3.13}$$

$$\alpha_{rdn} = \frac{1}{t}\int_0^t \frac{kC}{1+kC}\cdot\frac{nFd\upsilon_0}{Wi_0^{B/A}}\left[I_{rdn}(t)\right]^{(B/A-1)} dt \tag{3.14}$$

$$\alpha_{tri} = \frac{1}{t}\int_0^t \frac{kC}{1+kC}\cdot\frac{nFd\upsilon_0}{Wi_0^{B/A}}\left[I_{tri}(t)\right]^{(B/A-1)} dt \tag{3.15}$$

Assuming *B*=1.51*A* [174], the volume fraction of SiC between the ramp-up and the rectangular waveform, with peak current of $i_{p.}$, becomes

$$\frac{\alpha_{rup}}{\alpha_{rec}} = \frac{\int_0^t \left[I_{rup}(t)\right]^{(B/A-1)} dt}{\int_0^t \left[I_{rec}(t)\right]^{(B/A-1)} dt} = 0.662\times\left(\frac{i_{p,rup}}{i_{p,rec}}\right)^{0.51} \tag{3.16}$$

Since the volume fraction is the same for the ramp-up, ramp-down and triangular waveform, at the same peak current density the rate (=$\frac{\alpha_{rup}}{\alpha_{rec}}$) is 0.662, and at the same average current density, the rate is 0.9427.

3.3 Experimental

In the electroforming experiments, the composition of the bath solution was nickel sulphamate 330g/l, nickel chloride 15g/l, boric acid 30g/l and saccharin 1g/l. An amount of 20g/l SiC (β SiC) with a diameter of about $100\,nm$ was added. The electrolyte was agitated by a mechanical stirrer with 400rpm, while the temperature was kept at 50℃, and the initial pH of the electrolyte was 4.2, which is a typical value used in electroforming. The cathode mandrel was made of stainless steel with dimensions of $30mm \times 30mm \times 1mm$, and ground finished on grade 240 emery papers. After electroforming, the surface morphology of each specimen was examined by SEM (Scanning Electron Microscopy).

The waveforms as shown in Figure 3.1 were introduced in the electrodeposition. The frequency is 100Hz and the duty cycle is 50%. In order to compare the effect of different shaped current waveforms with the conventional pulse current with regard to the deposition behaviour, the same average current densities were used in the experiments.

The Ni-SiC films were then weighed on a high precision electronic balance in air and in distilled water respectively. The weight in air and in water can be expressed as [55]:

$$\begin{aligned} W_{air} &= \rho_{sample} V g \\ W_{air} - W_{water} &= \rho_{water} V g \\ \rho_{sample} &= \frac{W_{air}}{W_{air} - W_{water}} \rho_{water} \end{aligned} \tag{3.17}$$

where V is the volume of the sample, the density of the sample can be calculated from the weight in air and in water. The volume fraction of SiC particles (x) in the Ni-SiC film can then be calculated from the measured sample density by

$$\rho_{sample} = \rho_{SiC} \cdot x + \rho_{Ni} \cdot (1 - x) \tag{3.18}$$

The density of nickel is 8.902gcm^{-3}; the density of silicon carbide is 3.217gcm^{-3}.

3.4 Results and Discussion

3.4.1 Volume Content of SiC particles

Figure 3.4 is the volume fraction obtained by different waveforms. It can be seen that the volume fraction of SiC increases with increasing current density for all waveforms, but when the latter exceeds 10Adm^{-2}, the rate of increase in volume fraction decreases significantly. The rectangular waveform with relaxation time produces the largest amount of SiC, whereas the other waveforms yield similar SiC content in the deposit.

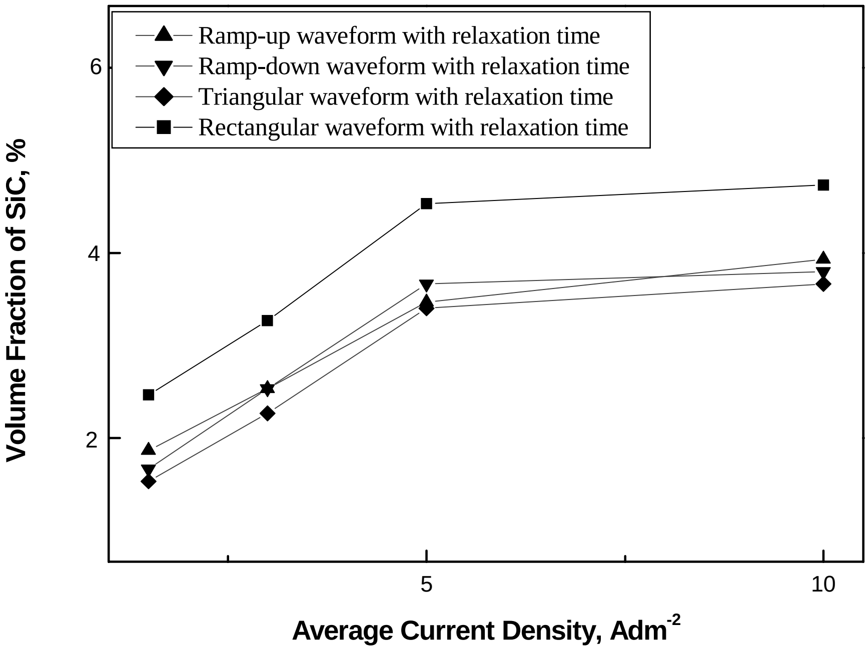

Figure 3.4 The volume fraction of SiC under different current waveforms

Figure 3.5 shows the simulated volume fractions of SiC produced by different shaped current waveforms. The volume fraction is found to increase with increasing current density for all the four waveforms, and the rectangular waveform with relaxation time has the largest amount of SiC in the deposit, while the ramp-up, ramp-down, triangular waveforms with relaxation time have similar volume fractions.

These results are consistent with the experimental findings as shown in Figure 3.4. It is interesting to note that at low peak current densities, the rate of increase (as indicated by the slope of α / i_p) is very high, but it levels off when the peak current density increases. A similar trend has also been reported by other researchers [19, 76, 174].

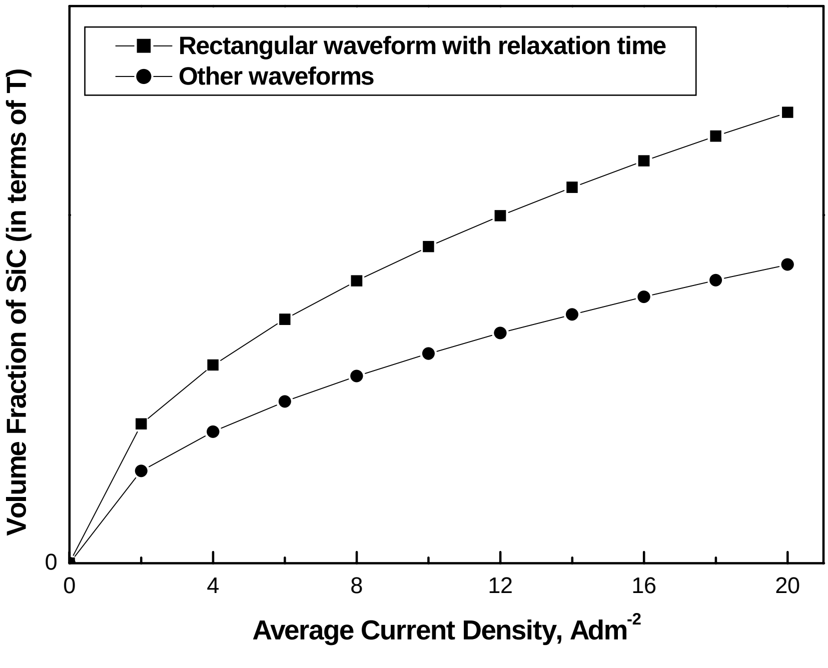

Figure 3.5 Predicted volume fractions of SiC particles under different waveforms

3.4.2 Morphology of Electrodeposited Composite

Although Guglielmi’s model is useful for explaining the kinetics of the codeposition process, it is unable to describe the second stage of the metal deposition process which involves the incorporation of adatoms into the periphery of a newly formed or already present monatomic layer. Figures 3.6&3.7 show the surface morphology of the electrodeposited composite obtained under different waveforms. It is found that the deposit produced by the four waveforms, both with relaxation time, have different grain sizes. The trend for producing the finest grain size is of the order: $rup > tri > rdn > rec$.

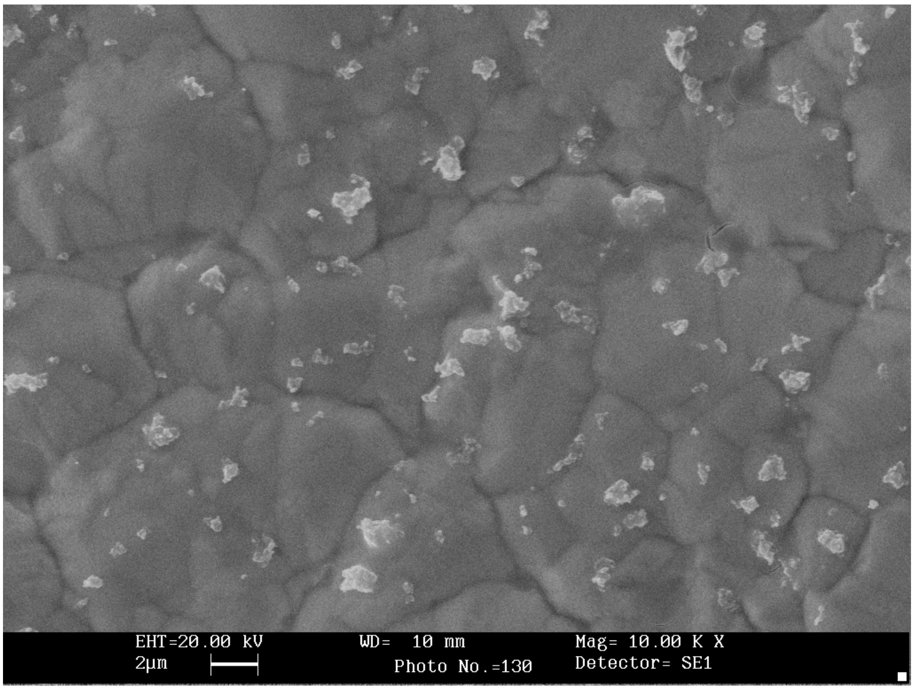

(a) Ramp-up waveform with relaxation time

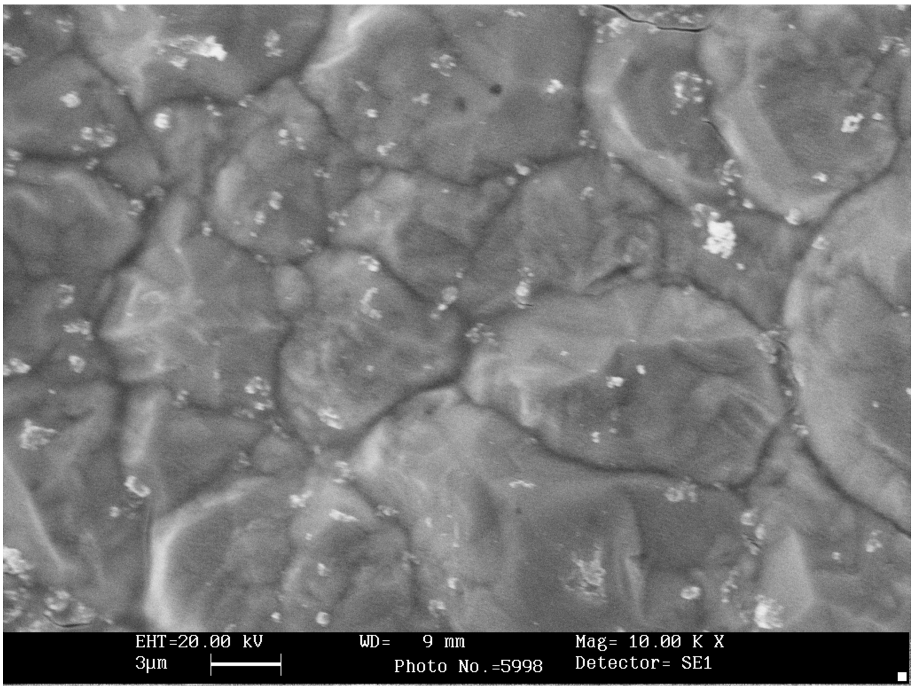

(b) Ramp-down waveform with relaxation time

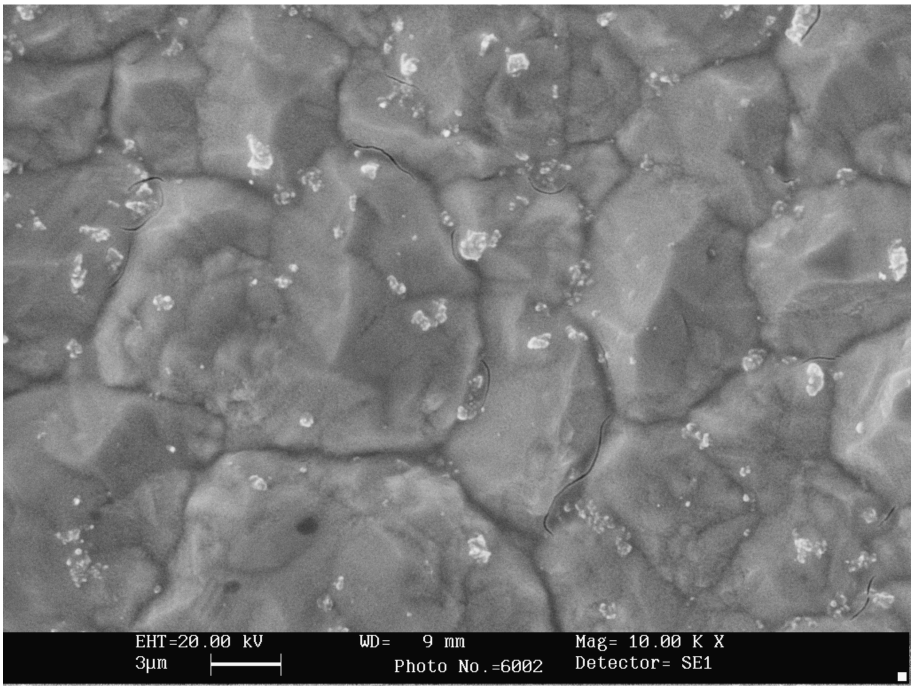

(c) Triangular waveform with relaxation time

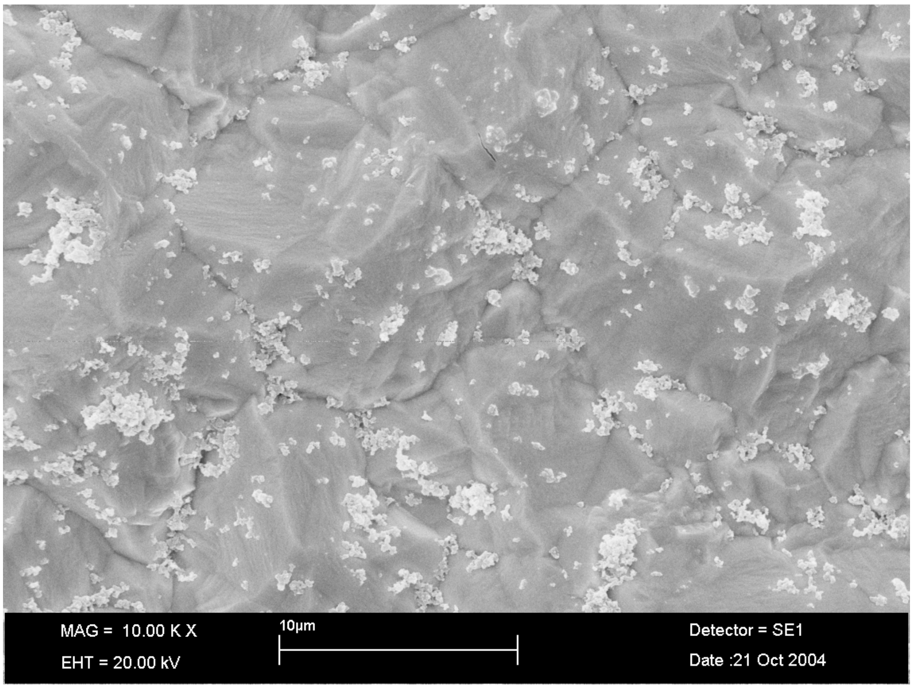

(d) Rectangular waveform with relaxation time

Figure 3.6 SEM photos showing the surface morphology of the deposit obtained at a fixed electrocodeposition thickness condition under an average current density of $0.5 Adm^{-2}$

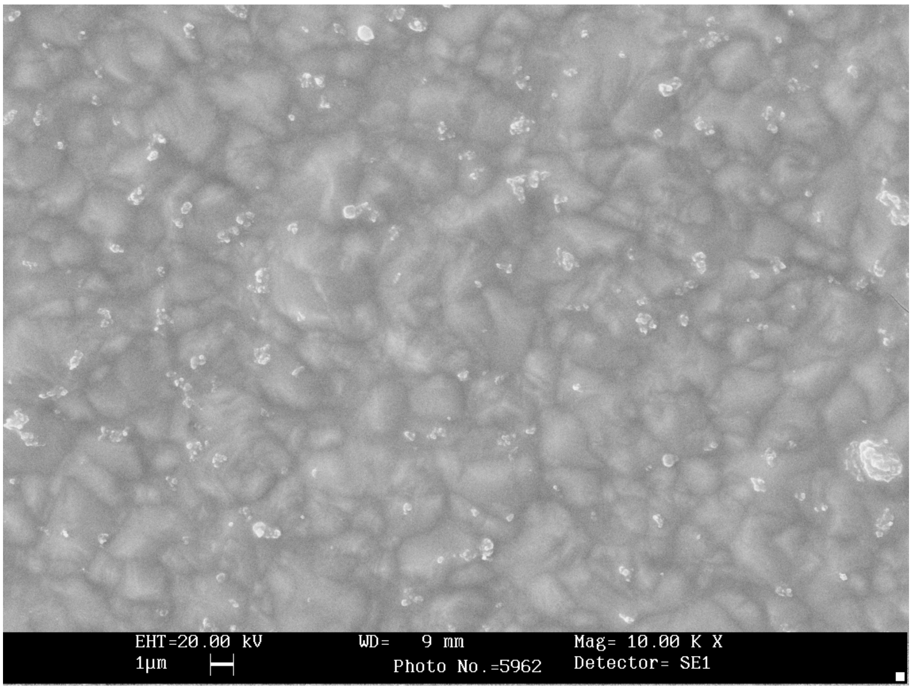

(a) Ramp-up waveform with relaxation time

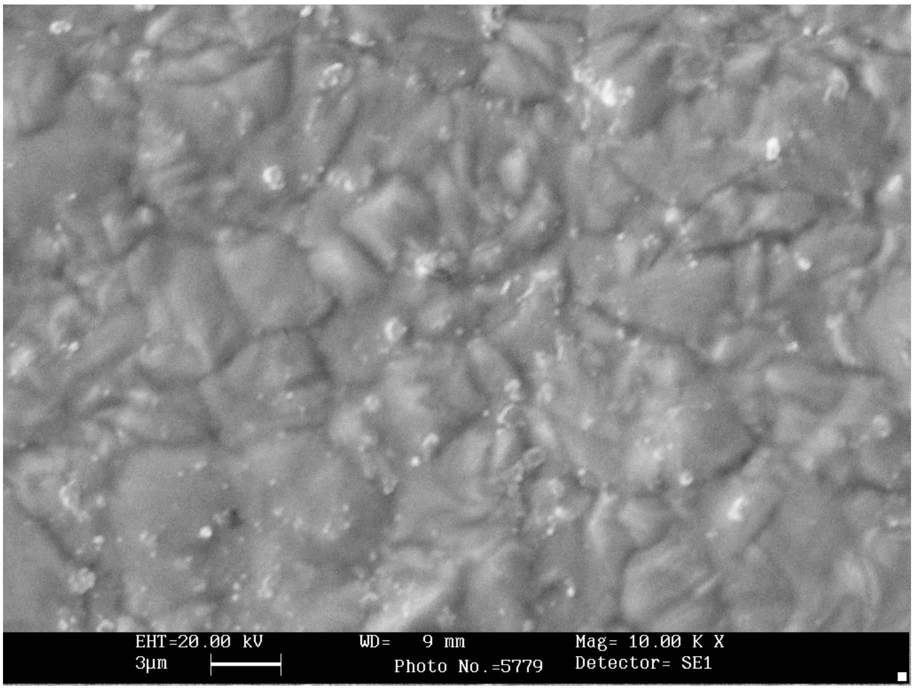

(b) Ramp-down waveform with relaxation time

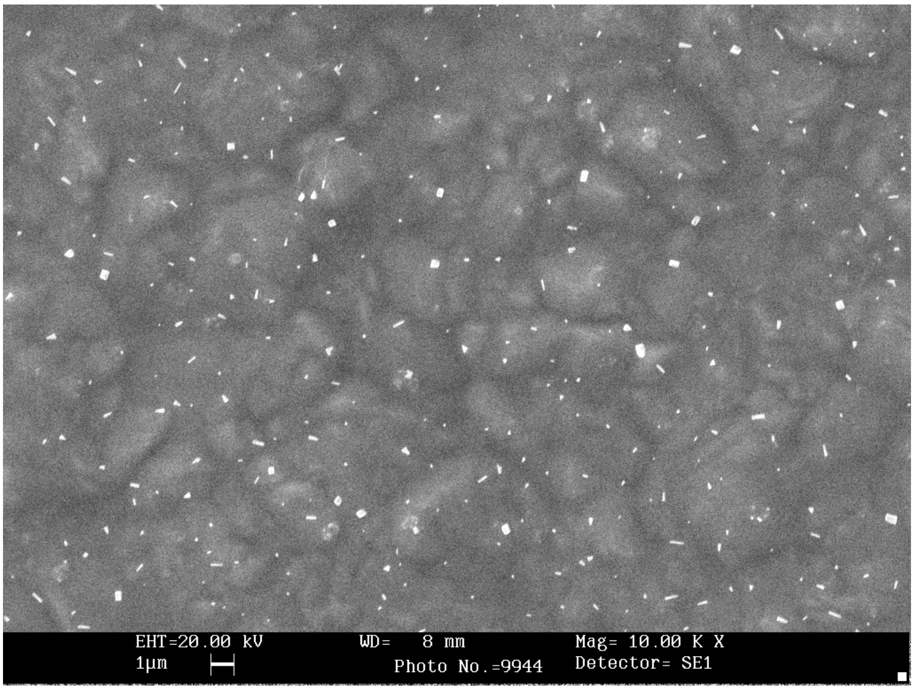

(c) Triangular waveform with relaxation time

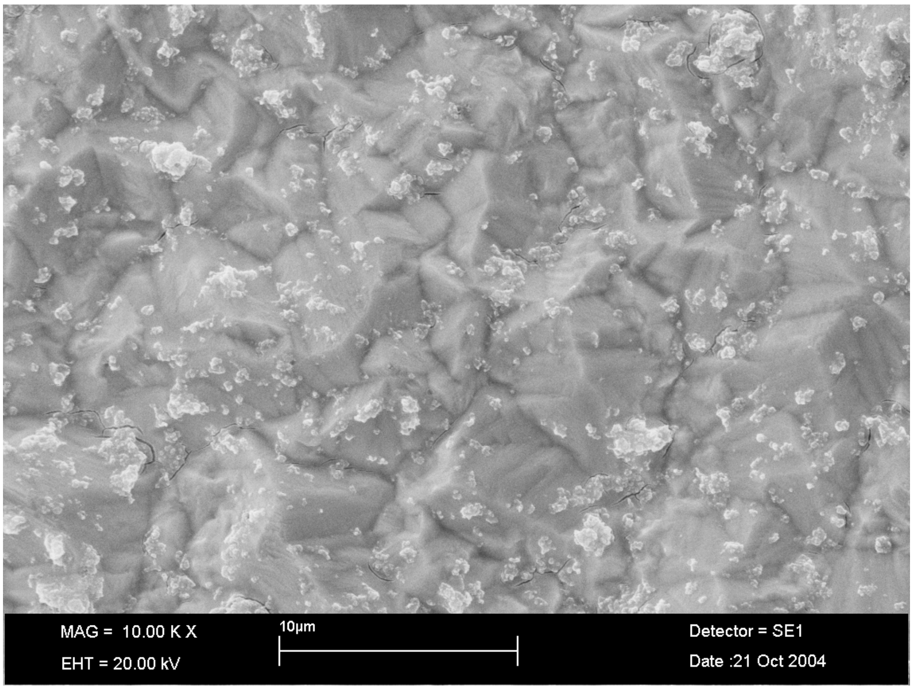

(d) Rectangular waveform with relaxation time

Figure 3.7 SEM photos showing the surface morphology of the deposit obtained at a fixed electrocodeposition thickness condition under an average current density of 1Adm^{-2}

The conventional nucleation rate considers the free energy (ΔG_c) of new interface and the growth of new grains. In the present study, SiC particles are found to have no ion-reaction in the process, and its effect on the deposition area is relatively insignificant as the volume percentage of SiC embedded in the deposit is very small. Thus the nucleation rate can be described as

$$J = K\exp(-\frac{\Delta G_c}{RT}) = K\exp(-\frac{\pi h\sigma_1^2 M}{\rho nFRT}\cdot\frac{1}{\eta}) = K\exp(-\frac{P\pi h\sigma_1^2 M}{\rho nFRT}\cdot\log\frac{i_0}{i}) \qquad (3.19)$$

It can be deduced from this equation that overpotential is the main parameter to determine the nucleation rate. Assuming that the deposition behaviour follows the ideal layer-by-layer growth such that the surface deposition area will quickly be covered by another layer, the grain size of each deposit layer will be reduced at a higher overpotential value. For a rectangular waveform, the nucleation rate becomes,

$$J_{rec} = K\exp\left(-\frac{P\pi h\sigma_1^2 M}{\rho nFRT} \cdot \log \frac{i_0}{\frac{i_p}{m+1} + \sum_{n=1}^{\infty}\left\{ \frac{i_p}{n\pi} \cdot \sin\left(\frac{2n\pi}{m+1}\right)\cos\left(\frac{2n\pi}{T}t\right) + \frac{2i_p}{n\pi} \cdot \sin^2\left(\frac{n\pi}{m+1}\right) \cdot \sin\left(\frac{2n\pi}{T}t\right)\right\}} \right) \tag{3.20}$$

Similarly, the nucleation rate of the ramp-up waveform (J_{rup}), ramp-down waveform (J_{rdn}), and the triangular waveform (J_{tri}) can be found. As nucleation rate varies with time, an average nucleation rate (J_{aver}) is given by

$$J_{aver.} = K \cdot \exp\left(-\frac{P\pi h\sigma_1^2 M}{\rho nFRT} \cdot \log \frac{i_0}{i_{aver.}(t)} \right) \tag{3.21}$$

The i_{aver} for the four waveforms are similar, and the average nucleation rates of the four waveforms are also found to be similar.

In the present study, it is interesting to note that under the average current densities of 0.5Adm^{-2} and 1Adm^{-2}, the ramp-up waveform with relaxation time produces the smallest grain size, while the rectangular waveform with relaxation time has the largest gain size. The equations that derived from conventional nucleation rate are not capable of explaining the phenomenon, and the analysis of the four waveforms with average current densities will be discussed in details in Chapter 4. Moreover, the analytic equation is not capable of comparing the shape-induced effect of different current waveforms. There is a need, therefore, to develop a more precise model to take into account the shape effect in the electrodeposition behaviour of Ni-SiC composites.

3.5 Conclusions

The effect of different types of waveform on the electrocodeposition behaviour of Ni-SiC composite has been experimentally and theoretically investigated. According to the experimental findings, at a constant pulse period and a fixed electrodeposition thickness, the largest amount of SiC embedded in the deposit was obtained when a rectangular waveform was used. Guglielmi’s model was successfully applied to predict the volume fraction of SiC embedded in the nickel matrix under different waveforms.

The findings of this Chapter are also of significance as it may be also possible to control the microstructures and to enhance the deposit quality of the electro-composite by manipulating different shaped current waveform during the electrocodeposition process. However, the conventional analytic equation for nucleation rate derived from the average current density cannot precisely reflect the effect of shaped current waveforms, so an in-depth analysis should be done to investigate the shape-induced effect and also the electrocodeposition behaviour.

Chapter 4 Equivalent Circuit Modeling of Electrodeposition of Ni-SiC Composites

4.1 Introduction

Pulse current and different current waveforms are able to produce deposits with more uniform particle distribution and better surface morphology than those obtained under direct current [56, 174]. It is generally believed that a higher instantaneous peak current in pulse and current waveform will lead to a more homogeneous surface morphology, a higher nucleation rate, and finer grains [80, 175]. Some researchers investigated the influence of pulse current on the double layer between the electrolyte and the solution. It was discovered that in the charging and discharging of a pulse, especially for short pulses, the double layer distorts the pulse current [176], and affects the overpotential response acting on the electrolyte [177]. In past decades, the electrodeposition of Ni-SiC composite attracted much research attention due to its potential application in the aerospace and automotive industries, in manufacturing and its use in medical devices [178]. Although pulse current was proved to result in better morphology, excellent wear resistance, and a more uniform particle distribution in the metal matrix than those attained by direct current techniques [56, 80]. There is a need to develop an in-depth simulation to investigate the electrocodeposition behaviour and also the shape-induced effects.

Electrochemical impedance spectroscopy (EIS) and description in terms of an equivalent circuit are common techniques for analyzing complicated processes involving surface and solution reactions. The EIS technique has been widely used to investigate the mechanism of nickel electrodeposition. Watson and Walters [52, 179] have observed two inductive loops in the impedance Nyquist plots. Yeh and Wan [12] reported two semicircles in the Nyquist plots, which showed two consecutive electron transfer reactions to occur during the reduction. Nowak et al [169] have revealed that a capacitive loop exists in the high frequency range, and at low frequency, there exists a sharp change from a capacitive to an inductive behaviour in a relatively narrow potential range. Benea et al [49] have found that the two inductance loops in the impedance diagram are converted to a single inductance loop upon the addition of nanosized SiC particles. Preliminary work has been done on the improvements of Ni-SiC composites obtained under a triangular waveform [180, 181]. Similar trends are believed to be applicable for the comparison between different shaped waveforms and direct current. The peak current density and average current density are common factors to be considered on the electrodeposition system, but the shape of different current waveforms is less investigated. The application of an equivalent circuit model can give an alternative and analytical method to describe and compare the shape-induced phenomenon under different current waveforms.

In this chapter, based on the equivalent circuit model, the electrodeposition behaviour of Ni-SiC composites is to be examined under four different waveforms. The electrochemical codeposition process was then transformed into an RC circuit, whereby the complicated electrolyte reactions were resolved as an electrical and mathematical problem.

4.2 Experimental

A three-electrode glass cell was used. The working cathode mandrel was made of stainless steel with dimensions of $30\text{mm} \times 30\text{mm} \times 1\text{mm}$, and ground finished on grade 240 emery papers. A saturated calomel reference electrode (SCE) and a counter electrode of pure nickel were used. Electrochemical impedance spectra were acquired in the frequency range of 30kHz to 5mHz with a 10mV amplitude sine wave generated by a frequency response analyzer. Current-voltage curves were recorded at a sweep rate of 20mV/s.

The composition of the bath was 330g/l nickel sulphamate, 15g/l nickel chloride, 30g/l boric acid and 1g/l sodium dodecylsulfate (SDS). An amount of 20g/l SiC (β SiC) of the diameter about 100nm was added. Figure 4.1 shows the morphology of the as-received silicon carbide powders, illustrating that they are of relatively spherical shape. The electrodeposition conditions are same as that described in Chapter 3.

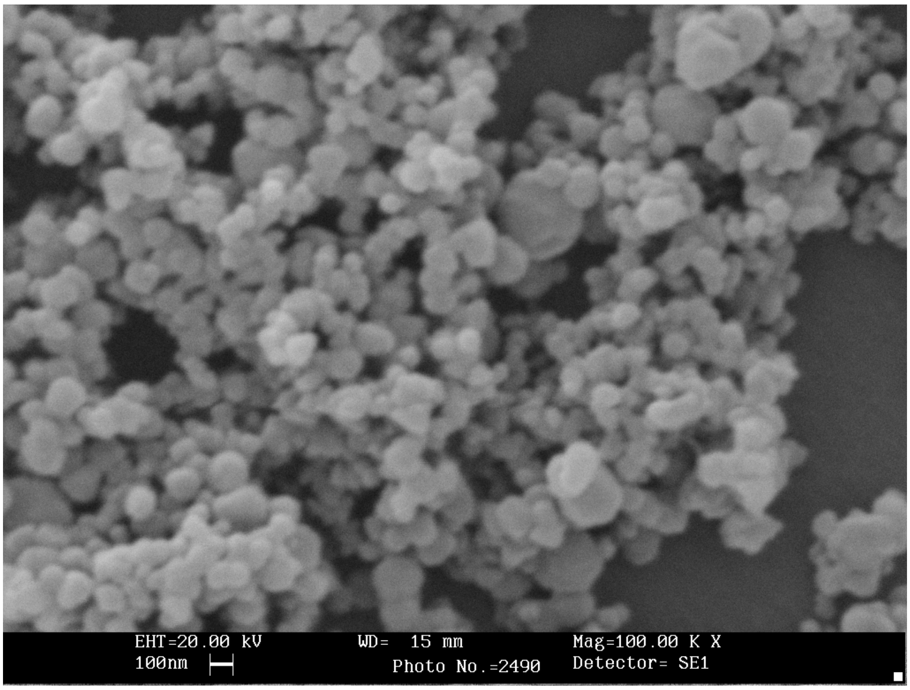

Figure 4.1 SEM image showing morphology of as-received SiC particles with diameter of about 100 nm

After electroforming, scanning electron microscopy (SEM, Leica Steroscan 440) was used to study the surface morphology of the composite and the X-Ray energy dispersion spectroscopy (EDX) system was utilized to determine its composition. The grain size of the composite was measured by transmission electron microscopy (TEM, JEOL 2010). The amounts of particles are also measured by the Archimedes method. Rectangular, triangular, ramp-up and ramp-down current waveforms were introduced to drive electrodeposition. The pulse parameters used were: $f=100Hz$ and $t_{on}=t_{off}$, where t_{on} is the deposition time and t_{off} is the relaxation time, and $T=t_{on}+t_{off}$. Figure 3.1 is the schematic diagram of the waveforms. Vickers microhardness of the composites was conducted under a load of 25 grams on a cross section of the composites. The load and testing surfaces were selected to avoid any subtract effect on the measurement of microhardness.

4.3 Theoretical Consideration

The Ni-SiC impedance behaviour in nickel sulphamate is studied. As a weak amplitude sine-shaped potential perturbation is superimposed on the steady-state potential value, sine-shaped modulations of θ and I are produced. The Nyquist plots of EIS measurements are shown in Figure 4.2. The diagram is composed of a high-frequency capacitive loop followed by a low frequency inductive loop.

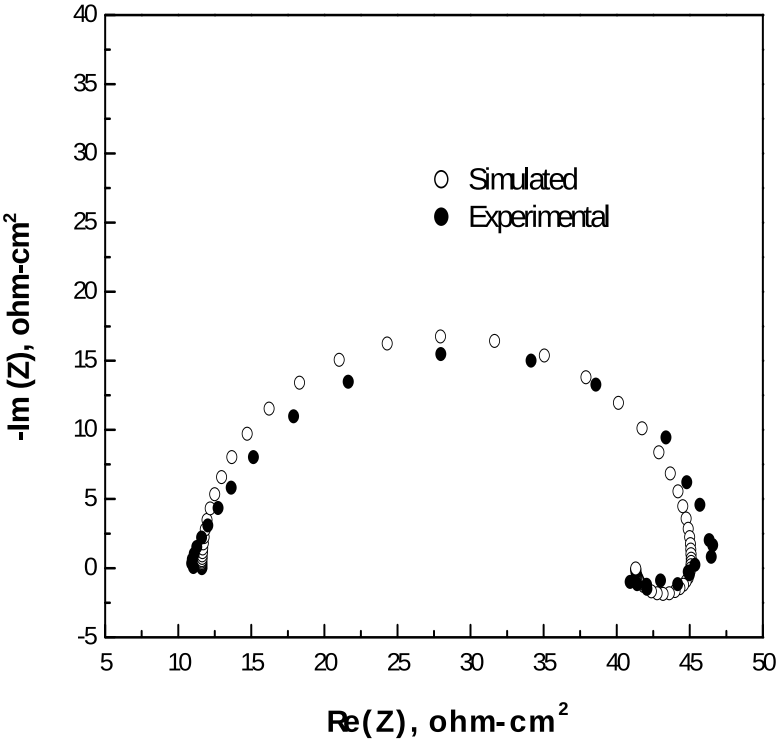

Figure 4.2 Comparison between experimental and simulated Nyquist plots in the Ni-SiC electrodeposition system at -750mV vs reference electrode (SCE) under a rotation rate of 400rpm

The high-frequency capacitive loop represents the reduction mechanism in the nickel sulphamate bath, and it includes the double layer capacitance and the charge transfer resistance.

The reduction of pure nickel in a Watts bath has been described in details by other mechanisms. Epelboin and Wiart [137] proposed a model using a chemical impedance procedure. The authors consider that the reaction mechanism involving an intermediate species, $(NiOH)^{+}_{ads}$, plays an important role in the rate-determining step. The addition of silicon carbide particles influenced the reactions in three main ways:

(1) Offering more nucleation sites that are detrimental to crystal growth;

(2) Nanoparticles will enhance the ionic transport, and also activate the nickel reduction [49];

(3) The presence of SiC particles in the solution results in an increase in surface roughness, and blocks off part of the electrode surface [169].

In the present bath composition, the nickel ions are firstly adsorbed on the electrode and incorporated with mono-hydroxide ions, as described by Eq. (4.1), and reduced to nickel adatoms in two steps, represented by Eqs. (4.2) and (4.3). The nickel adatoms will then enter kink sites and produce a film on the deposit.

$$Ni^{2+} + OH^{-} \rightarrow Ni(OH)^{+} \tag{4.1}$$

$$Ni(OH)^{+} \rightarrow Ni(OH)^{+}_{ads} \tag{4.2}$$

$$Ni(OH)^{+}_{ads} + 2e^{-} \rightarrow Ni + OH^{-} \tag{4.3}$$

Although the addition of SiC particles in the bath has a significant effect on the electrodeposition behaviour, Eqs. (4.2) and (4.3) are still considered to be the rate-determining steps, and will be used in formulating the equivalent circuit model for the composites.

The inductive loop was also observed by many researchers, and it was believed that it represented the presence of the intermediate. Some researchers represented the inductive loops as the surface coverage of the adsorbed intermediate [52, 179], whereas, other researchers considered that the loop was relating to the adsorption/desorption process of intermediates at/from the cathode surface [12, 49]. Epelboin et al also reported that an intermediate, Ni_{ads}^{+}, was involved in the electrocodeposition process of Ni-SiC [137].

A number of researchers [12, 49, 52] have applied an inductive circuit to describe the electrodeposition behaviour, but Franceschetti and Macdonald [183] pointed out that it is only an apparent inductance since real inductance requires the storage of energy in a magnetic field and there is no appreciable ac magnetic field energy present in low current impedance spectrum measurements. They proposed a circuit that involves both a negative capacitor and a negative resistor. Macdonald [184] suggested that an RC element with negative capacitance and resistance (which will yield a positive RC time constant) provides a more physical representation of processes leading to inductive features. In this Chapter, the equivalent circuit shown as Figure 4.3 is applied to represent the electrochemical response during the electrodeposition of Ni-SiC composite coatings.

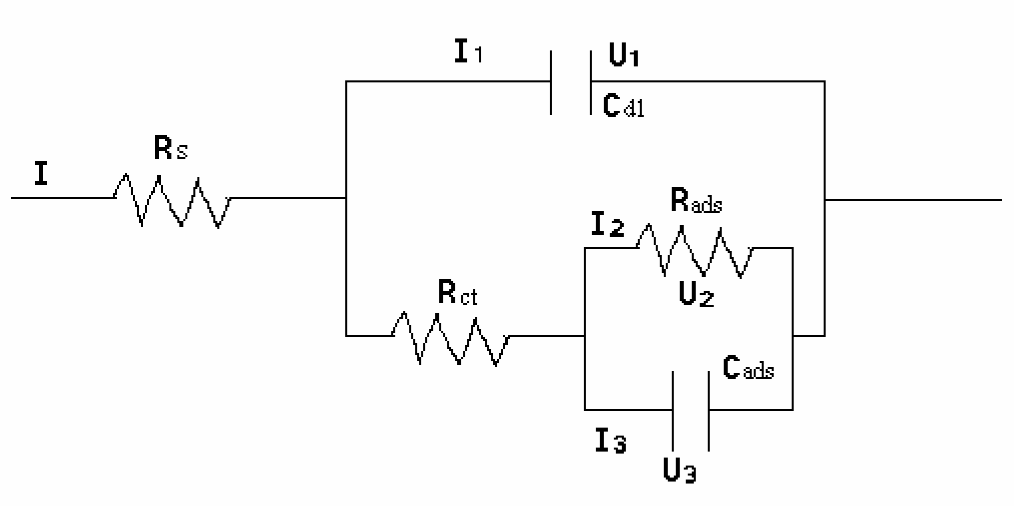

Figure 4.3 An equivalent circuit describing the electrochemical response during the electrodeposition of Ni-SiC composite coatings

In the circuit, R_s is the solution resistance between the reference and the working electrodes, which represents the resistance of the ions in the electrolyte that are transferred to the electrode. C_{dl} is the double layer capacitance of interface between the electrode and the electrolyte, and R_{ct} is the charge transfer resistance of reactions in the electrolyte. C_{ads} the pseudocapacitance from the adsorbed intermediates and R_{ads} desorption resistance. C_{ads} and R_{ads} are used to account for the surface coverage of adsorbed intermediates and the rate for desorption [12, 49, 52].

The current applied on the equivalent circuit can be divided into two components, the capacitive current, I_1, and the Faradic current, I_2+I_3, and their relation is as follows:

$$I_1 + I_2 + I_3 = I(t) \tag{4.4}$$

The capacitive current is related to the potential:

$$I_1 = C_{dl} \cdot \frac{dU_1}{dt} \tag{4.5}$$

where U_1 is the potential drop and C_{dl} is the capacitance of the double layer, which is independent of U_1.

The pseudo-capacitive current can be expressed by

$$I_3 = C_{ads} \frac{dU_3}{dt} \tag{4.6}$$

Current I_2 is consistent with Ohm's law

$$I_2 = \frac{U_2}{R_{ads}} \tag{4.7}$$

The potentials applied on the double layer, U_1, on the charge transfer, U_2, and on the inductive layer, U_3, are given by

$$U_2 = I_2 \times R_{ads} = U_3 \tag{4.8}$$

$$U_1 = (I_2 + I_3)R_{ct} + U_2 \tag{4.9}$$

According to Eqs. (4.4) ~ (4.9), we obtain:

$$I_1 = C_{dl} C_{ads} R_{ct} R_{ads} \frac{d^2 I_2}{dt^2} + (C_{dl} R_{ct} + C_{dl} R_{ads}) \frac{dI_2}{dt} \tag{4.10}$$

$$I_3 = C_{ads} R_{ads} \frac{dI_2}{dt} \tag{4.11}$$

$$U_1 = (R_{ct} + R_{ads}) I_2 + C_{ads} R_{ct} R_{ads} \frac{dI_2}{dt} \tag{4.12}$$

Substituting Eqs. (4.5) ~ (4.11) into Eq. (4.4), the following is obtained:

$$C_{dl} C_{ads} R_{ct} R_{ads} \frac{d^2 I_2}{dt^2} + (C_{dl} R_{ct} + C_{dl} R_{ads} + C_{ads} R_{ads}) \frac{dI_2}{dt} + I_2 = I(t) \tag{4.13}$$

Upon substitution of the waveform function into Eq. (4.11), I_2 can be calculated, while the voltages can be obtained from Eqs. (4.8) and (4.12).

Based on the above equations, the currents and voltages of the circuit can be obtained for the first pulse. In order to determine the performance of the circuit in a stationary state, its currents and voltages are also determined for successive pulses, and it is assumed that during the on-time or off-time period, the initial potential of the capacitor equals the potential at the end of the last pulse period.

4.4 Modeling of the Effect of Different Shaped Current Waveforms

4.4.1 Dependence of Current Waveform

Figures 3.6&7 compare the Ni-SiC surface coatings obtained from rectangular, triangular, ramp-down and ramp-up waveforms with relaxation time. The composite coatings develop a pyramid-like structure. The SiC particles are found to be homogeneously incorporated in the nickel matrix, and the shape of current waveforms significantly influences the surface morphologies of the composites. It is shown that the grain size is greatly influenced by the shaped current waveform. The largest grain size is obtained by the rectangular waveform while the ramp-up waveform results in the finest grain size.

Figure 4.4(b) is the line-scanning result of a white region of the surface shown in Figure 4.4(a). The result shows that particles consist of high silicon and low nickel content, as shown in Figure 4.4(b), representing the presence of SiC particles. Spot scanning result on the same surface (coated with gold) also showed that the white region consists of SiC particles, as shown in Figure 4.5.

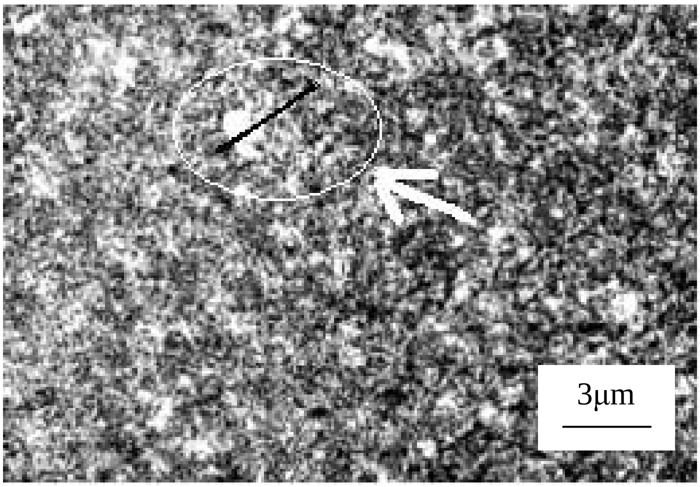

(a)

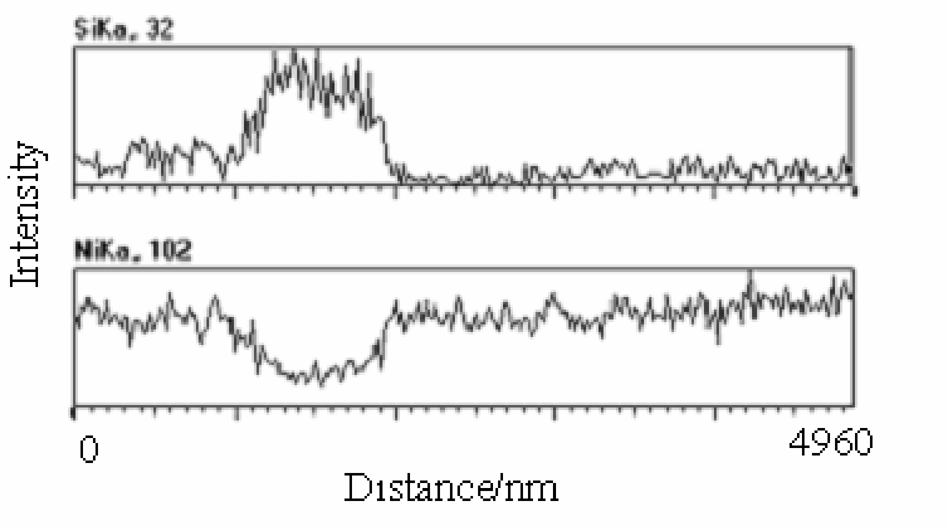

(b)

Figure 4.4 EDX line scan (b) of region of Ni-SiC composite coating indicated in (a) obtained at an average current density of 0.3Adm^{-2} under the ramp-down waveform

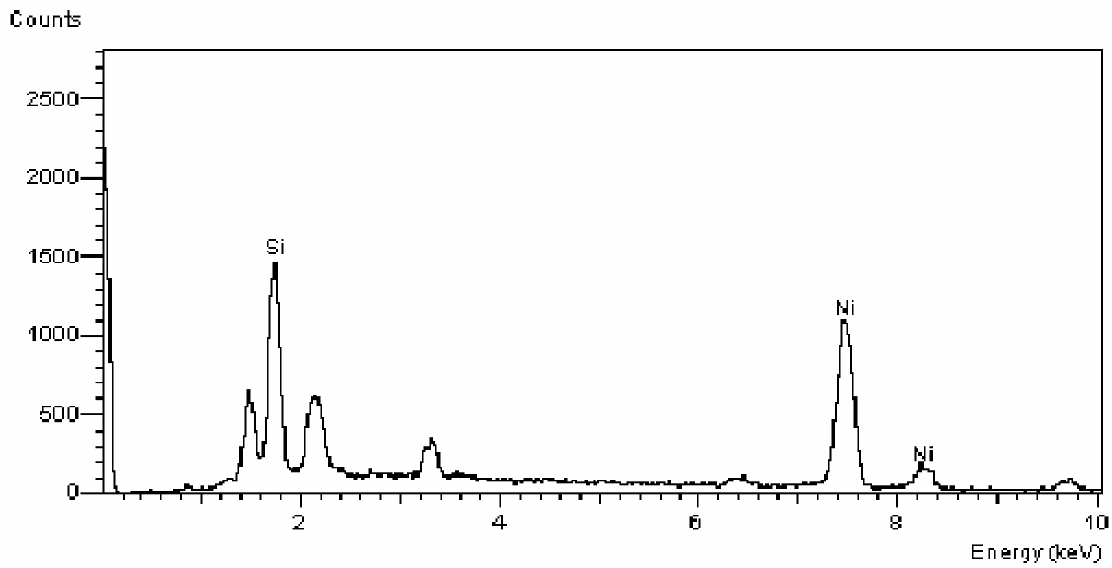

Figure 4.5 EDX spot scan of Ni-SiC composite coating obtained at an average current density of 0.3Adm^{-2} under the ramp-up waveform

4.4.2 Charge Transfer Simulation

The limiting current density of the process was also obtained from the current-voltage curves, as shown in Figure 4.6. The diffusion limiting current density is about 13Adm^{-2} for the electrodeposition with or without dispersed particles. But the addition of silicon carbide nanoparticles has shifted the curve and it is attributed to an increase in the active surface area due to the adsorbed particles on the cathode [52, 179]. As the applied average current density (1Adm^{-2}) is much less than the limit current density, the mass transport effect can be assumed to be negligible, and the current waveform is mainly controlled by the charge transfer effect. The equivalent circuit described in Figure 4.3 can be applied to describe the process. By fitting the model to the experimental data, the parameters of the circuit are obtained and are shown in Table 1. Figure 4.2 shows the experimental and simulated Nyquist plots. The model reasonably fits the data and the Chi-squared value is about 3.412×10^{-3}. The RC time constants of the circuit $\tau_H(C_{dl}R_{ct})$ and $\tau_L(C_{ads}R_{ads})$ are found to be ~0.052ms and ~0.378ms respectively, indicating that the reaction of intermediates is the rate determining step during nickel electrodeposition.

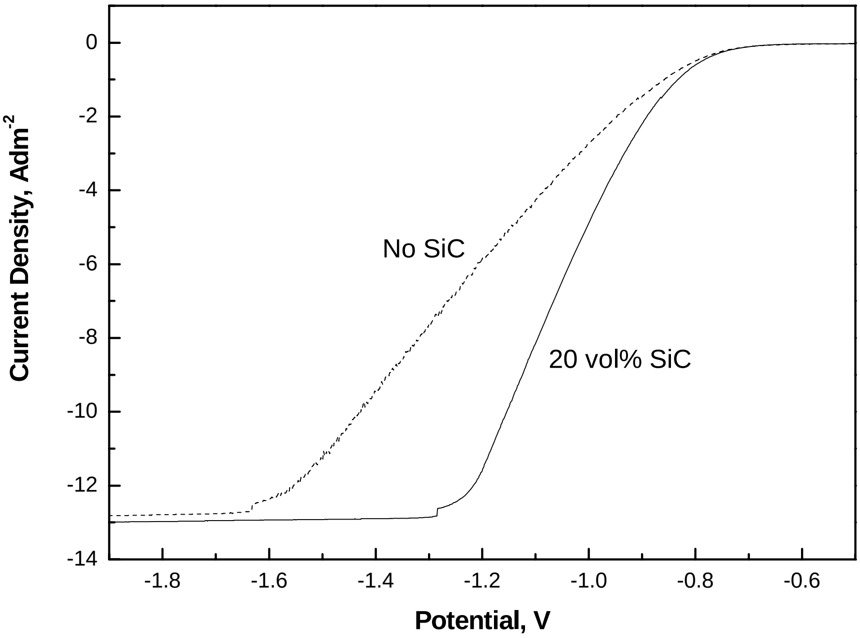

Figure 4.6 Cathodic potentiodynamic diagrams for codeposition of nickel and SiC particles (20g/l SiC in the electrolyte) and pure nickel electrodeposition at a sweep rate 20mV/s.

Table 4.1 Impedance parameters of the Ni-SiC electrodeposition system

R_s	11.62Ω-cm^2
R_{ct}	33.52Ω-cm^2
R_{ads}	-3.829Ω-cm^2
C_{dl}	36.64μF
C_{ads}	-0.3096F

The ramp-up, ramp-down, triangular, and rectangular waveforms with relaxation time can be transferred to an electrical and mathematical problem. During on-time and off-time periods, the currents passing through the charge transfer resistor under the two waveforms are shown in Tables 4.2~4.5 and Figure 4.7. At T=0.01, the applied peak current equals 0.1A. It is shown that the four waveforms can accumulate electrical energy in the on-time period, then discharge the energy in the off-time period, thus giving an instantaneous peak current for charge transfer. At the same average current density, i_{aver}, the ramp-up waveform with relaxation time provides an instantaneous peak current for charge transfer which is 63.2% higher than that of the rectangular waveform, both with relaxation time. The electrodeposition process is well known as a competition between nucleation and grain growth. A high instantaneous peak current of the ramp-up waveform is detrimental to crystal growth, for it facilitates the creation of new nuclei and suppresses grain growth. Thus the morphology of Ni-SiC coating should definitely be improved and the hardness will be greater than that under the ramp-down waveform. Meanwhile, the nickel ions also have higher velocity to move towards the cathode under higher instantaneous peak current, leading to an increase of the nickel ions concentration on the surface of the deposit, which is favorable to the cathodic electrodeposition.

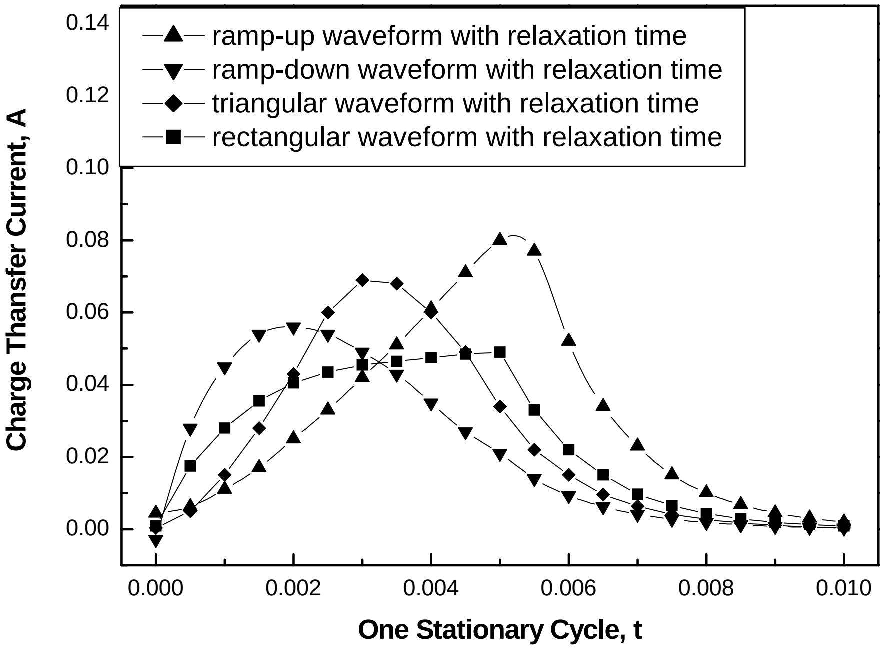

Figure 4.7 Simulation of charge transfer current in a stationary state

Table 4.2 Current passing through the resistor for charge transfer under the ramp-down waveform

	Faradic Current
Ramp-down Waveform	On-time
	$I_2 + I_3 = 0.12 - 20t - 0.123 \times e^{-811t} + 0.002899 \times e^{-0.844t}$
	Off-time
	$I_2 + I_3 = 0.02092 \times e^{-811t} + 4.048 \times 10^{-8} \times e^{-0.844t}$

Table 4.3 Current passing through the resistor for charge transfer under the ramp-up waveform

	Faradic Current
Ramp-up Waveform	On-time
	$I_2 + I_3 = -0.02 + 20t + 0.02438 \times e^{-811t} - 0.002887 \times e^{-0.844t}$
	Off-time
	$I_2 + I_3 = 0.0774 \times e^{-811t} - 2.345 \times 10^{-8} \times e^{-0.844t}$

Table 4.4 Current passing through the resistor for charge transfer under the rectangular waveform

	Faradic Current
Rectangular Waveform	On-time
	$I_2 + I_3 = 0.05 - 0.04915e^{-811t} + 0.0000606e^{-0.844t}$
	Off-time
	$I_2 + I_3 = 0.04915e^{-811t} - 5.135 \times 10^{-8} \cdot e^{-0.844t}$

Table 4.5 Current passing through the resistor for charge transfer under the triangular waveform and DC

Triangular Waveform	Up-time
	$I_2 + I_3 = -0.04 + 40t + 0.04608e^{-811t} - 0.005774e^{-0.844t}$
	Down-time
	$I_2 + I_3 = 0.14 - 40t - 0.08581e^{-811t} + 0.005786e^{-0.844t}$
	Off-time
	$I_2 + I_3 = 0.03320e^{-811t} + 0.0002514e^{-0.844t}$
Direct Current	$I_2 + I_3 = 0.25 + 0.00805e^{-811t} + 0.00556e^{-0.844t}$

4.4.3 Capacitive Current Simulation

The capacitive current is also important in the equivalent circuit. The current accumulated in the capacitor will be released in the off-time period and maintains the charge transfer current. Tables 4.6~4.9 and Figure 4.8 show the charging and discharging process of the capacitor. The simulation results clearly show that the shape of the current waveform has an important effect on the capacitive current as well as the electrodeposition behaviour. For the ramp-up and triangular waveforms, the capacitor will be charged during its on-time period since the applied *I(t)* increases from zero. However, the ramp-down and rectangular waveforms have high electricity at the beginning of its on-time period because of the high applied *I(t)*. After that, the capacitor under the ramp-down and rectangular waveforms will gradually discharge electricity because the applied *I(t)* decreases with time, and the capacitor under the ramp-up and triangular waveforms will charge electricity during the on-time period as the applied current increases with time. During the relaxation time, as shown in the simulation result, the discharge current under the ramp-up waveform, which is helpful for the charge transfer, is higher than the other three waveforms. Although these four current waveforms have the same average current, the shape of waveform influences the electrodeposition process significantly, and the capacitive current, $I_1(=I(t)-(I_2+I_3))$, is directly related to the charge transfer current (I_2+I_3) for a fixed applied current.

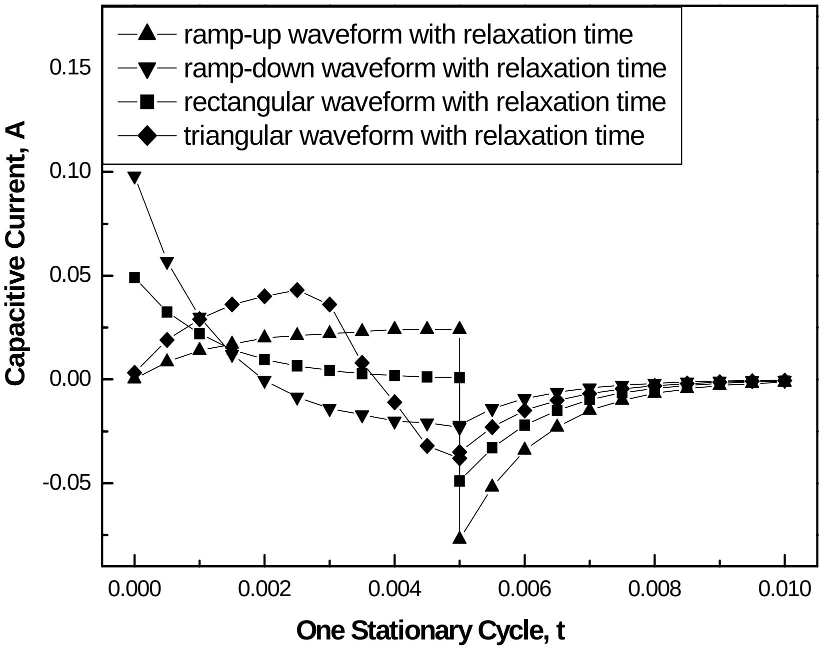

Figure 4.8 Simulation of capacitive current in a stationary state

Table 4.6 Current passing through the capacitor under the ramp-down waveform

	Capacitive Current
Ramp-down Waveform	On-time
	$I_1 = -0.02176 + 0.123 \times e^{-811t} - 0.002899 \times e^{-0.844t}$
	Off-time
	$I_1 = -0.02092 \times e^{-811t} - 4.048 \times 10^{-8} \times e^{-0.844t}$

Table 4.7 Current passing through the capacitor under the ramp-up waveform

	Capacitive Current
Ramp-up Waveform	On-time
	$I_1 = 0.02176 - 0.02438 \times e^{-811t} + 0.002887 \times e^{-0.844t}$
	Off-time
	$I_1 = -0.0774 \times e^{-811t} + 2.345 \times 10^{-8} \times e^{-0.844t}$

Table 4.8 Current passing through the capacitor under the rectangular waveform

	Capacitive Current
Rectangular Waveform	On-time
	$I_1 = 0.04915e^{-811t} - 0.0000606e^{-0.844t}$
	Off-time
	$I_1 = 0.04915e^{-811t} - 5.135 \times 10^{-8} \cdot e^{-0.844t}$

Table 4.9 Current passing through the capacitor under the triangular waveform and DC

	Capacitive Current
Triangular Waveform	Up-time
	$I_1 = 0.04352 - 0.04608e^{-811t} + 0.005774e^{-0.844t}$
	Down-time
	$I_1 = -0.04352 + 0.08581e^{-811t} + 0.005786e^{-0.844t}$
	Off-time
	$I_1 = -0.03320e^{-811t} + 0.0002514e^{-0.844t}$
Direct Current	0

4.4.4 Dependence of Current Density

Figure 4.9 shows the Ni-SiC surface coatings obtained by the triangular waveform with relaxation time. A nodular-like structure is observed under high current densities. Agglomerations of SiC particles are observed on the composite produced at low average density. A cross section of the composite obtained at $3Adm^{-2}$ under the triangular waveform is also examined to illustrate the incorporation of particles into the matrix, as shown in Figure 4.10.

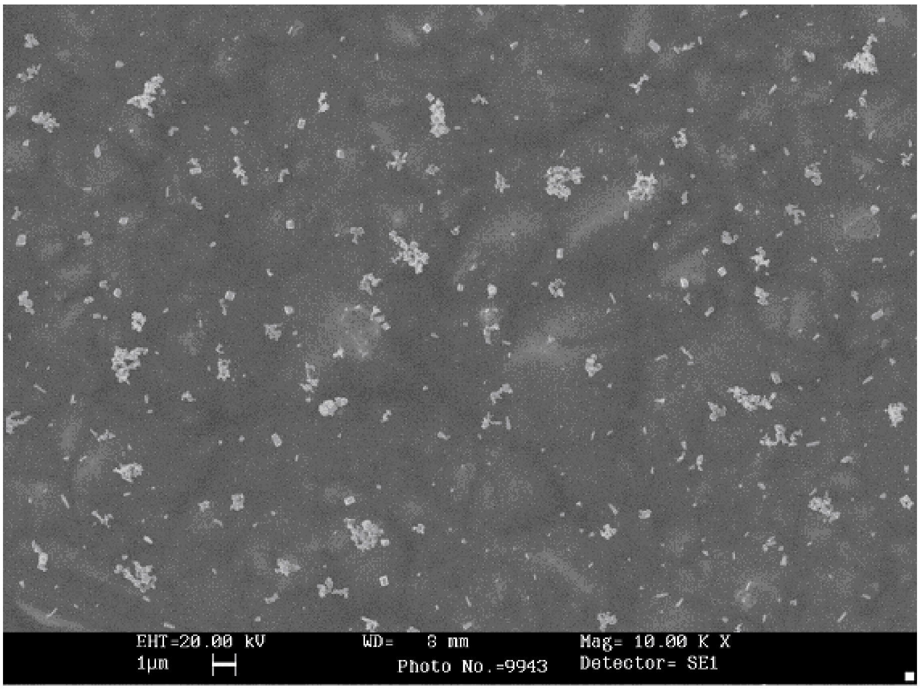

(b) 3Adm^{-2}

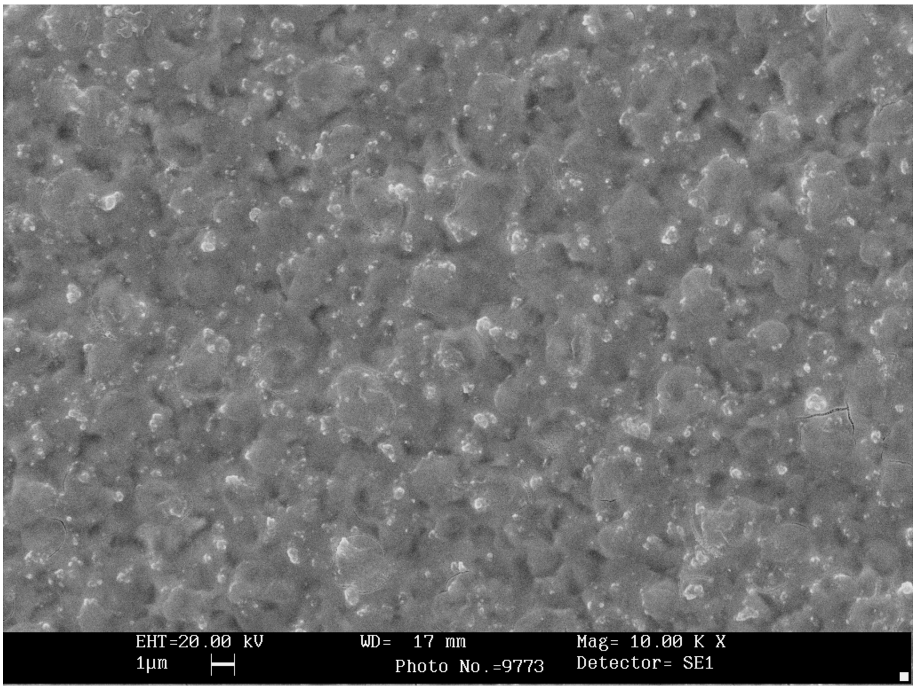

(c) 4Adm^{-2}

Figure 4.9 SEM morphology of Ni-SiC deposits under a triangular waveform with increasing average current density

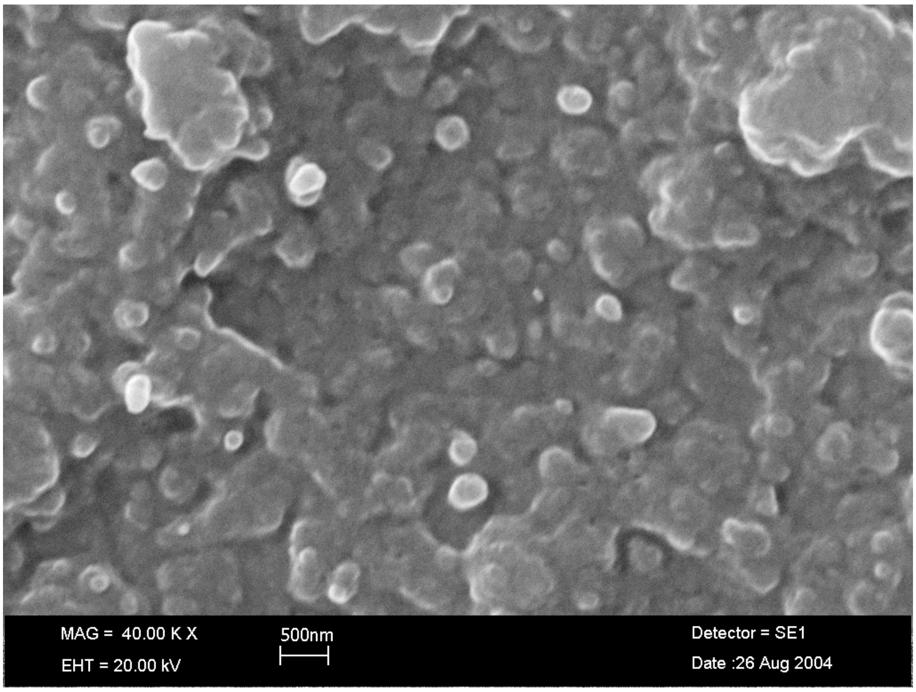

Figure 4.10 The cross section of the composite produced under the triangular waveform with relaxation time at a current density of 3Adm^{-2}

The Ni grain size is found to decrease as the average current density increases. Figure 4.9(a) shows that at an average current density of 2Adm^{-2}, the largest grain size of about 5 μm is obtained. And the TEM photos shown in Figure 4.11 also illustrate the grain sizes under different current densities. These results are in good agreement with the theory of nucleation and growth of electrodeposits, which predicts a larger nucleation rate at a high average current density, while more extensive growth of nuclei is expected to take place at low average current densities [179]. The grain size is also affected by the distribution and the volume percentage of SiC particles [56, 174, 177]. At a low average current density, the presence of particles near the cathode further suppresses the reduction of metal ions which is not beneficial to nucleation. But at a high average current density, the effect of particles on the deposition of metal ions becomes less significant [12, 49]. The SEM micrograph of the composite also shows that the SiC particles agglomerate significantly at low current density. At high current density, nickel ions dissolved from the anode transported faster, and the repulsive forces among nickel ions with SiC particles adsorbed on the surface is stronger than those under low current density conditions, thus SiC particles can be more dispersive on the deposits, and SiC agglomerations can hardly be produced.

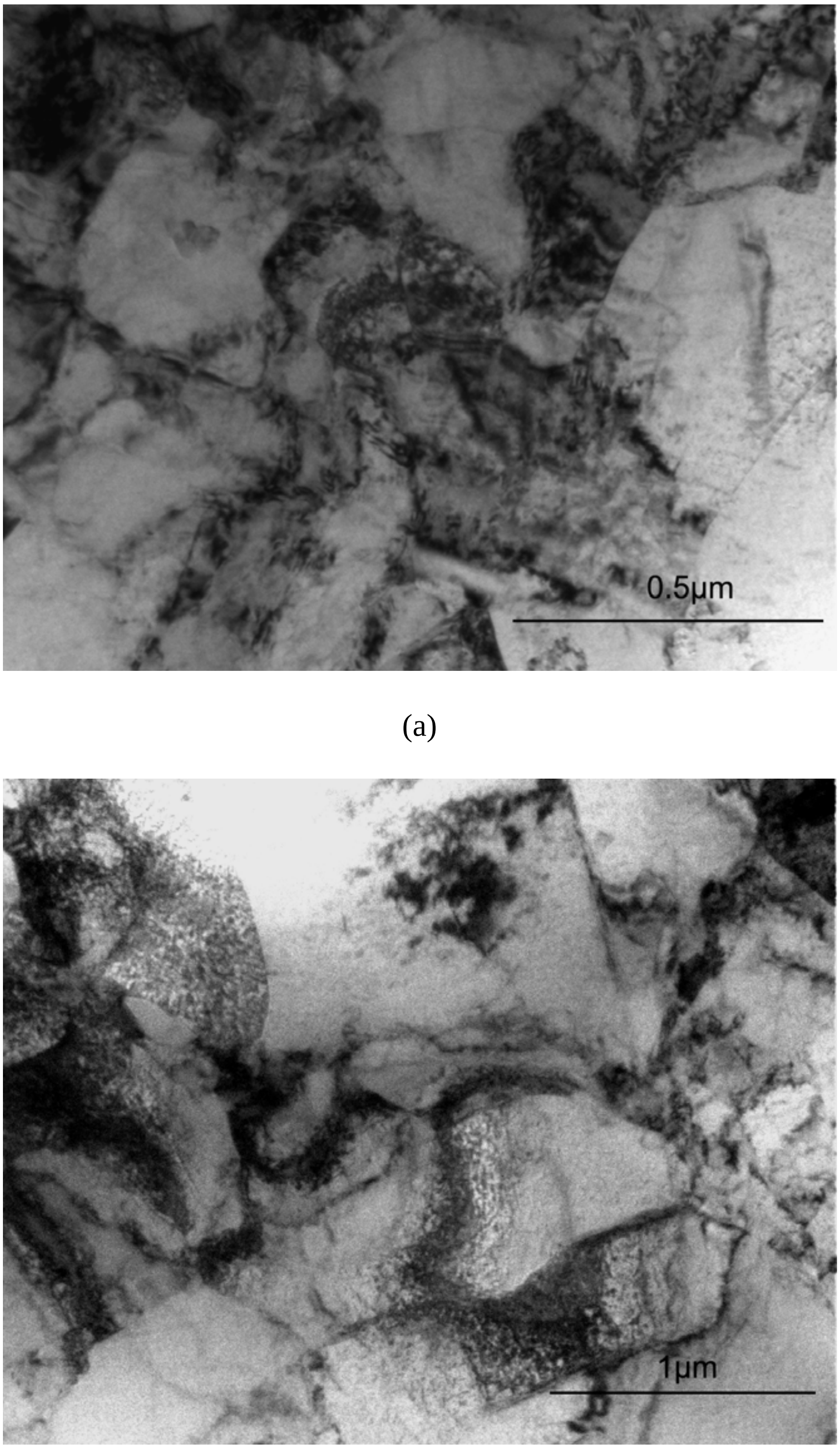

(a)

(b)

Figure 4.11 TEM brightfield micrograph of the Ni-SiC composites under average current densities of 4Adm^{-2}(a) and 3Adm^{-2}(b)

The effect of cathodic potential and particles on the EIS curves is also examined. Figure 4.12 shows that the change in cathodic potential does not significantly affect the shape of the curves, as they all comprise of a frequency capacitive loop followed by a low frequency inductive loop. But, the loop size is found to increase with increasing cathodic potential. Without the addition of particles, the EIS curve at a cathode potential of -750mV is also obtained. It is found that without the particles, the size of the EIS curve is increased, while its shape is maintained.

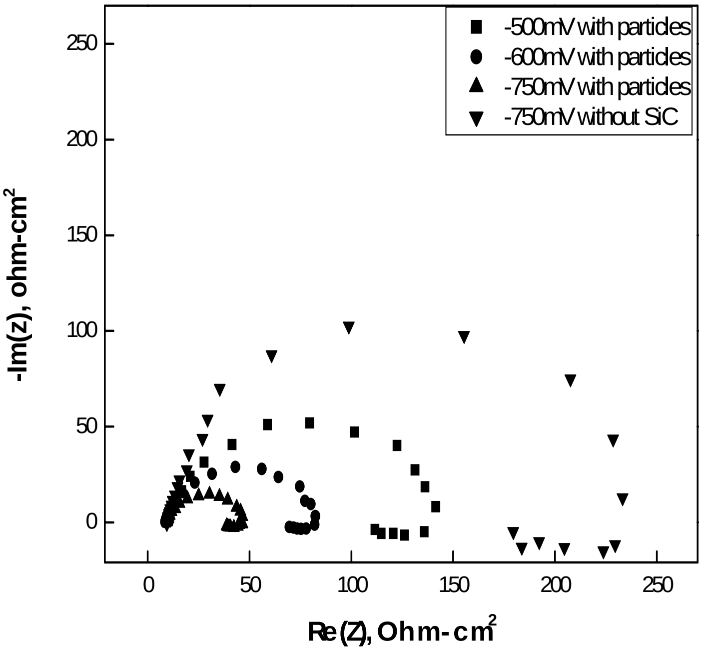

Figure 4.12 EIS curves of a Ni-SiC deposition system under different cathodic potentials, and a pure nickel electrodeposition system at a cathode potential of -750mV.

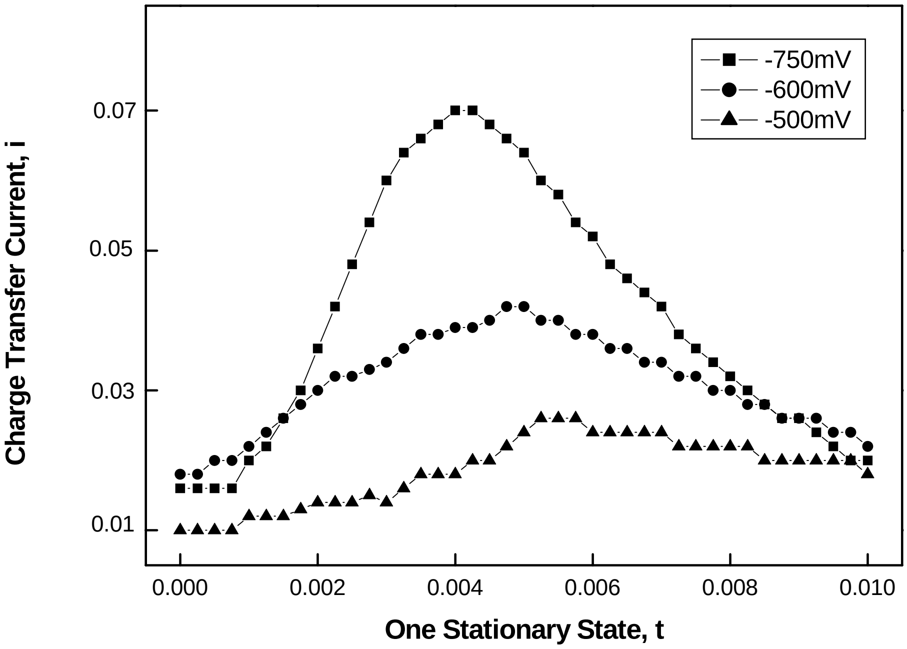

Figure 4.13 Simulated charge transfer current at different current densities under the triangular waveform

Based on the EIS curves of Figure 4.12, the faradaic current at different cathodic potentials under the triangular waveform is also simulated. Figure 4.13 shows that a higher instantaneous peak current for charge transfer under the triangular waveform is obtained when the applied cathodic potential increases.

4.4.5 Microhardness Results

The hardness is also found to decrease with decreasing average current density. Figure 4.14 shows the variation of Vickers micro-hardness of the Ni-SiC deposit with average current density under the four waveforms. The hardness of the Ni-SiC composite under the ramp-up waveform is greater than other waveforms, which is in accordance with the predictions of the EC model. The maximum hardness can reach to about HV450, which is significantly higher than those under the direct current, which normally has a hardness of around HV250. Hardness of composites is known to be related to matrix grain size as well as the volume fraction of reinforcement phases. It is obvious that as particles are of greater hardness and strength, they will inhibit the plastic flow of the soft nickel matrix and, hence, increase the hardness of nickel composite coatings [43]. Previous work has been done to examine the variation of SiC volume fraction under different shaped waveforms [181]. It is found that the two waveforms produced similar volume fractions and the volume fraction increases with increasing current density, which can explain the relationship between hardness and current density.

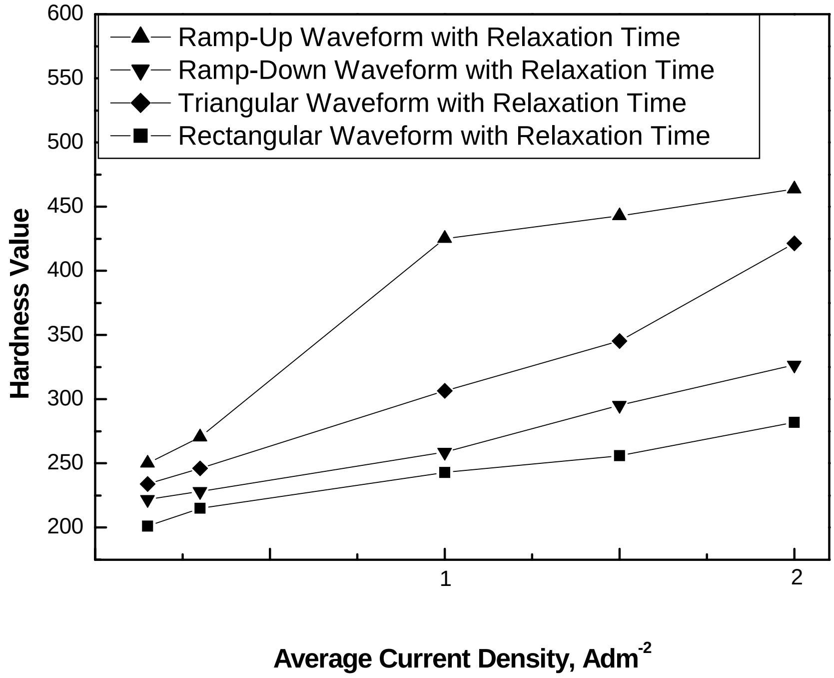

Figure 4.14 Vickers micro-hardness of Ni-SiC deposit at different average current densities under ramp-up and ramp-down waveforms

4.4.6 Conclusions

In this part, an equivalent circuit model (EC) deriving from the electrochemical impedance spectra was developed to describe the deposition behaviour of Ni–SiC composites under the four waveforms with relaxation time. Experimental results show that the ramp-up waveform results in finer grain size and enhanced hardness. The equivalent circuit model predicts the capacitive and faradaic currents of the process, which cannot be illustrated by the conventional nucleation rate as mentioned in Chapter 3. At the same average current densities, the ramp-up waveform has higher instantaneous peak current for charge transfer than that of rectangular waveform, and results in an improvement in the microstructure of the composite.

4.5 Effect of Pulse Parameters on Electrodeposition

4.5.1 Introduction

Pulse plating has received a considerable amount of interest in recent decades as its advantages include its availability of additional adjustable operating parameters (pulse frequency, duty cycle and pulse current density), and its possibility of achieving higher instantaneous current densities at the cathode [185~187]. Compared to direct current plating, pulse plating can produce fine grained and smooth electrodeposits, as well as decreasing the hydrogen content in the deposits [124, 188]. Moreover, pulse current changes the local current density compared with direct current for the same amount of charge [120]. Over the past years, the effect of pulse parameters on morphology, composition, structure, porosity, current efficiency and the properties of deposits has been investigated quite extensively [123, 124, 189]. The parameter of duty cycle was reported to affect the preferential orientation of CdSe alloy [126], the grain size of copper [128, 129], alloy composition [122, 190], and current efficiency [124, 125]. The effects of duty cycle are partly due to its influence on the diffusion and mass transfer behaviour. The parameter of pulse frequency is generally reported to be related to the stationary state. A higher pulse frequency should be avoided for a certain amount of time is needed to charge and discharge the electrical double layer at the electrode, and a too low pulse frequency will make the pulse current become a direct current. Although pulse parameters have significant influences on pure metals and alloys, relatively few investigations have been done on composites. In this Chapter, the electro-codeposition behaviour of Ni-SiC composites will be examined.

The findings in this thesis have proved, both theoretically and experimentally, that the different types of shaped current waveforms affect the morphology and microhardness of Ni-SiC composites. Although charging and discharging processes for the different shaped current waveforms are different, the duty cycle and frequency has insignificant effect on the shaped current waveforms. In this Chapter, modeling of the effect of duty cycle and frequency will be conducted for both the rectangular and the ramp-down waveforms, and their charging and discharging processes, coupled with the effects on the SiC incorporation, will also be discussed in details.

4.5.2 Experimental

The adopted parameters were: duty cycles $t_{on}/(t_{on}+t_{off})$ varied from 25% to 75%, while the pulse frequencies ranged from 10Hz to1000Hz. The average current density was fixed at 1Adm^{-2}. Figure 4.15 is the schematic diagram of the pulse currents, and Figure 4.16 is the schematic diagram of the ramp-down waveform with relaxation time. After electrodeposition, scanning electron microscopy (SEM, Leica Steroscan 440) was used to study the surface morphology of the composites and the X-Ray energy dispersion spectroscopy (EDX) system was utilized to determine the composition of the composite coating. The Vickers microhardness test was conducted under a load of 25g on a cross section of the composite. The load and testing surfaces were selected to avoid any substrate effect on the measurement of microhardness. A nanoindentor (Hysitron) was also employed to examine the mechanical properties of the Ni-SiC composite using a diamond Berkovich triangular pyramidal tip at a load of 8000μN.

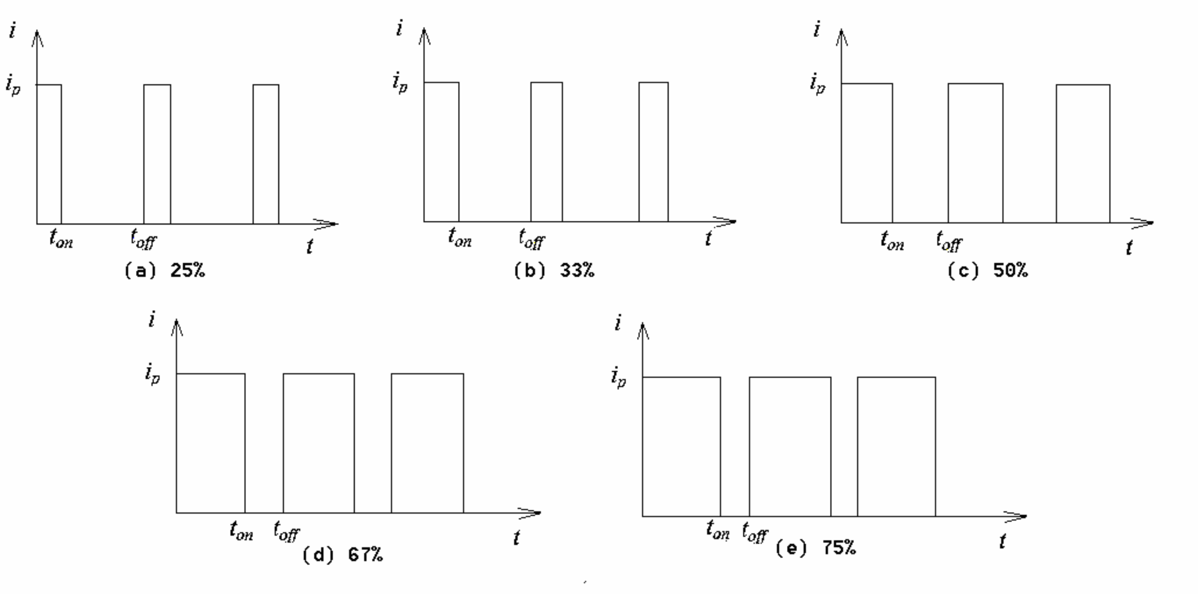

(a) 25% (b) 33% (c) 50% (d) 67% (e) 75%

Figure 4.15 The pulse current with different duty cycles (from 25% to 75%)

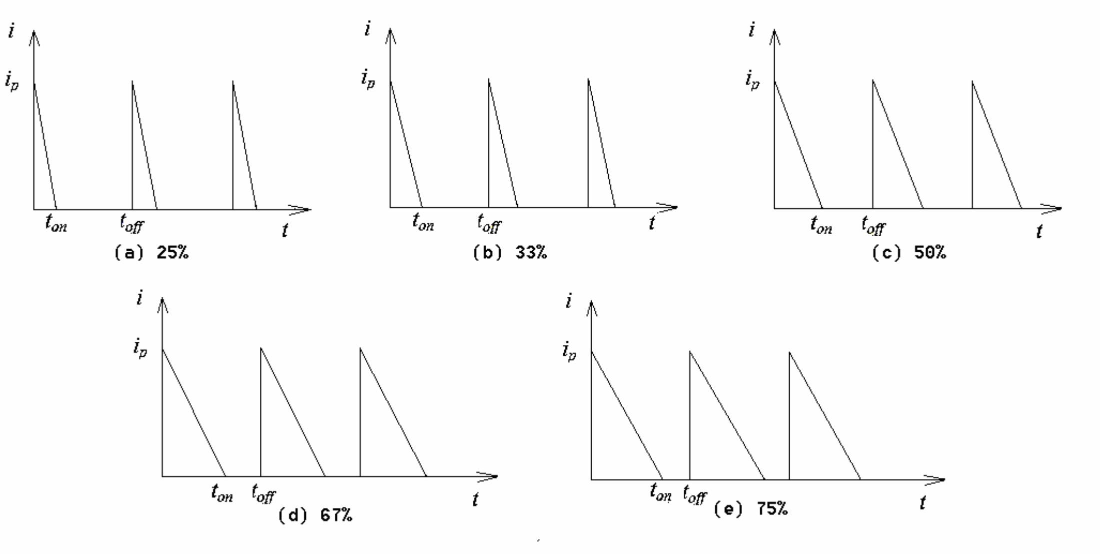

(a) 25% (b) 33% (c) 50% (d) 67% (e) 75%

Figure 4.16 The ramp-down waveform with different duty cycles (from 25% to 75%)

4.5.3 Current Waveforms under Duty Cycles and Frequencies

The charge transfer current in one stationary cycle at different duty cycles from 25% to 75% was plotted in Figure 4.17, and the charge transfer current at different pulse frequencies from 0.1Hz to 10000Hz was shown in Figure 4.18. They reveal that both parameters have significant influence on the instantaneous peak current. With the increasing of duty cycle, the instantaneous peak current decreases, and with the increasing of frequency, the peak current value also decreases. The highest instantaneous peak current is obtained at a duty cycle of 25% and frequencies below 10Hz. At high pulse frequencies, the charging and discharging period becomes very short and the pulse current acts as a direct current. It is interesting to note that at low frequencies, the charge transfer current of the two currents behaves like the applied current, with instant charge and discharge processes.

The frequency and duty cycle have similar influences on the two currents. It significantly affects the charging and discharging processes, but not the shape of the current waveform. In the following study, different pulse frequencies and duty cycles will be applied on the electrodeposition of Ni-SiC composites to analyze the effects of the pulse parameters.

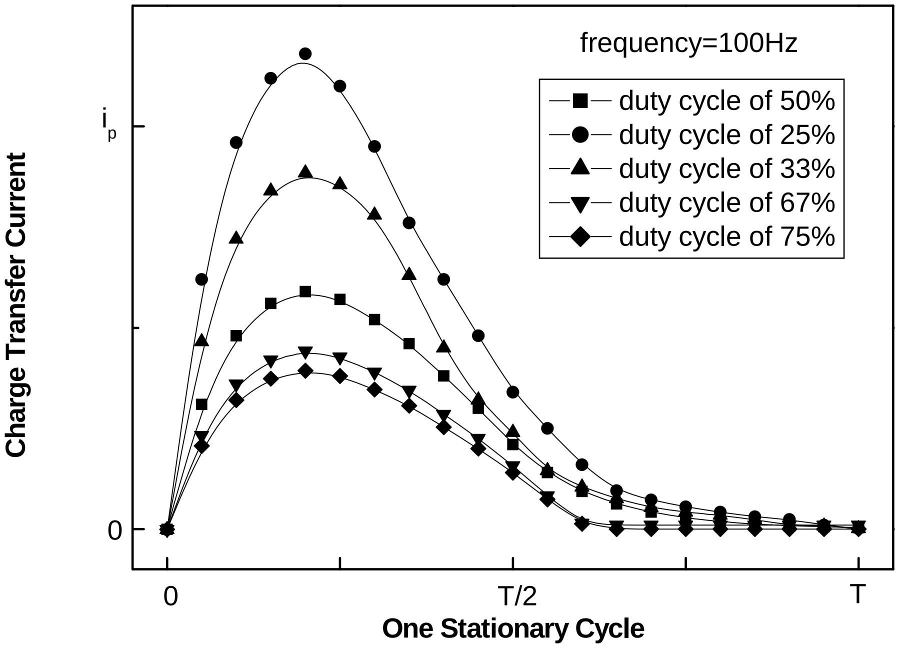

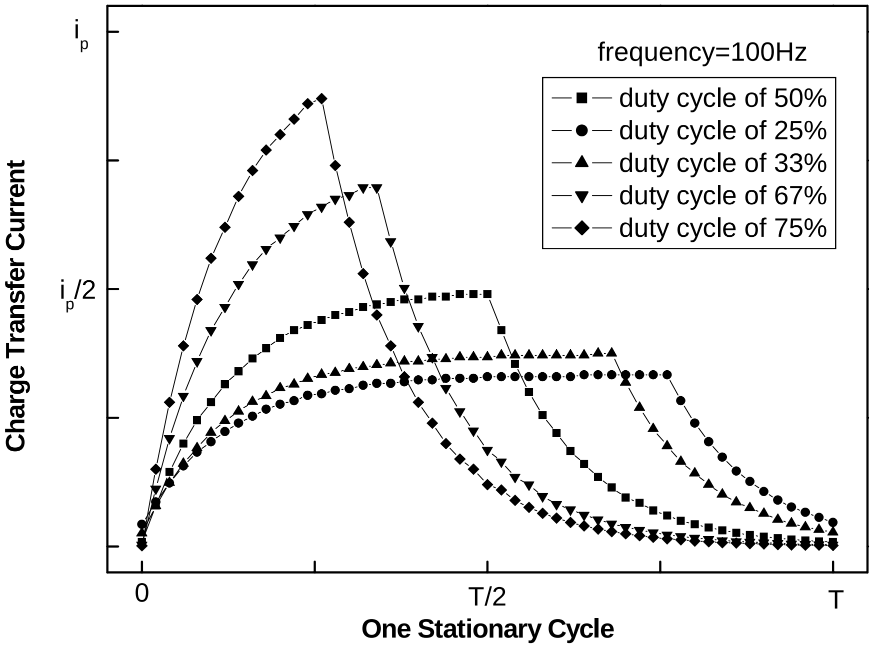

Figure 4.17 The comparison of charge transfer current under different duty cycles between the ramp-down waveform and the rectangular waveform, both with relaxation time

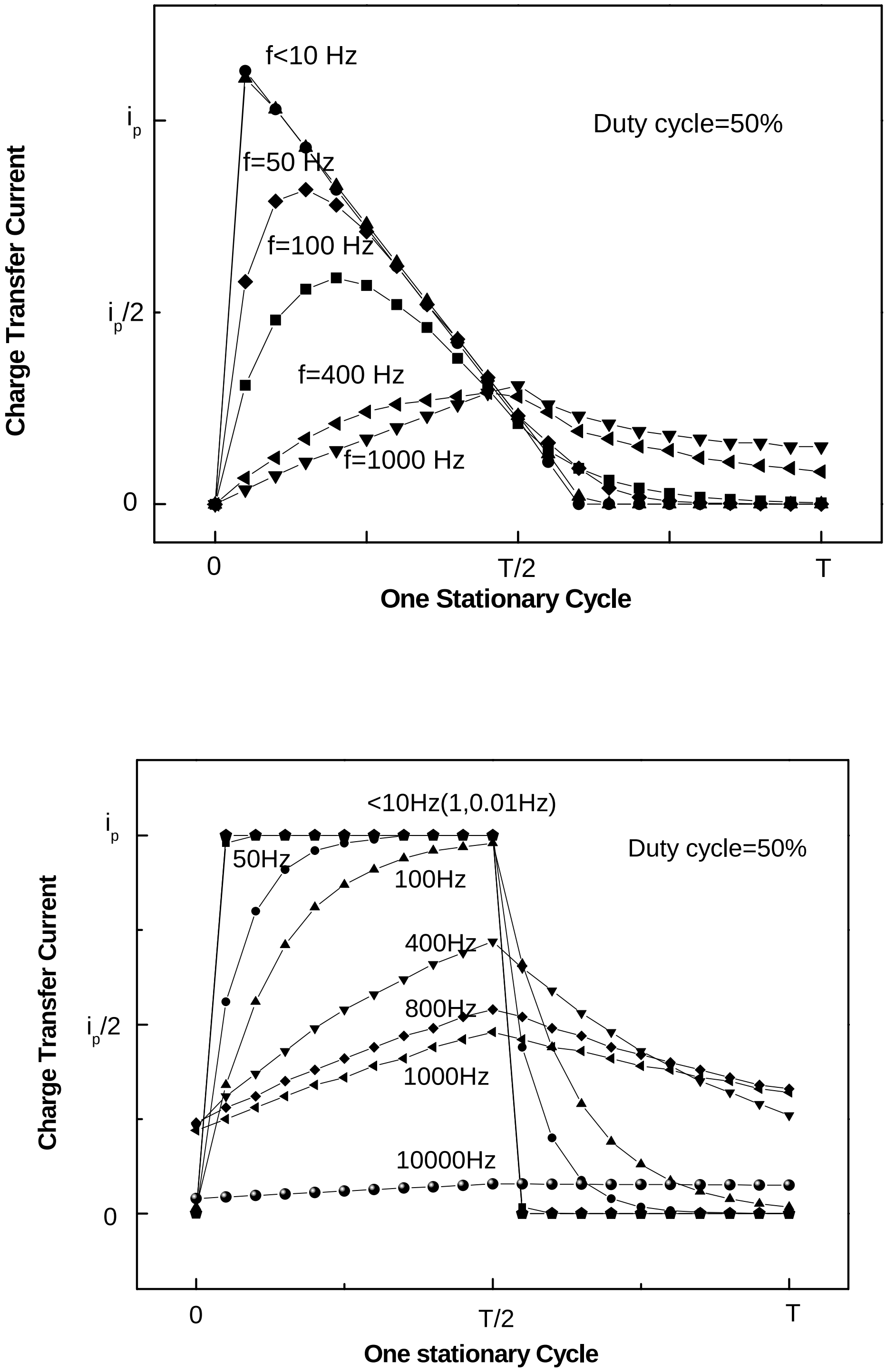

Figure 4.18 The comparison of charge transfer current under different pulse frequencies between the ramp-down waveform and the rectangular waveform, both with relaxation time

4.5.3 The Effect of Duty Cycle

4.5.3.1 Surface Morphology

Figure 4.19 shows the surface morphology of the deposits under different duty cycles. A typical pyramid microstructure, with embedded inert particles of SiC, is observed. With increasing duty cycle, the crystalline size of the nickel matrix increases, and the relationship between grain size and duty cycle is shown in Figure 4.20. For pulse electrodeposition, as duty cycle increases, the process approaches to direct current plating. But when the duty cycle decreases, there is an increase in peak current due to the increase of off-time, when the average current density is kept constant [130]. The high peak current results in a higher population of adatoms on the surface during deposition, which favours the formation of fine grains, as the nucleation rate increases exponentially with the value of overpotential. Moreover, the long off-time provides more time for nickel ions and other charged particles to settle down on the cathode. The increased amount of the ions and particles increases the number of nucleation sites, which favours the nucleation rate and results in fine grained deposits [126].

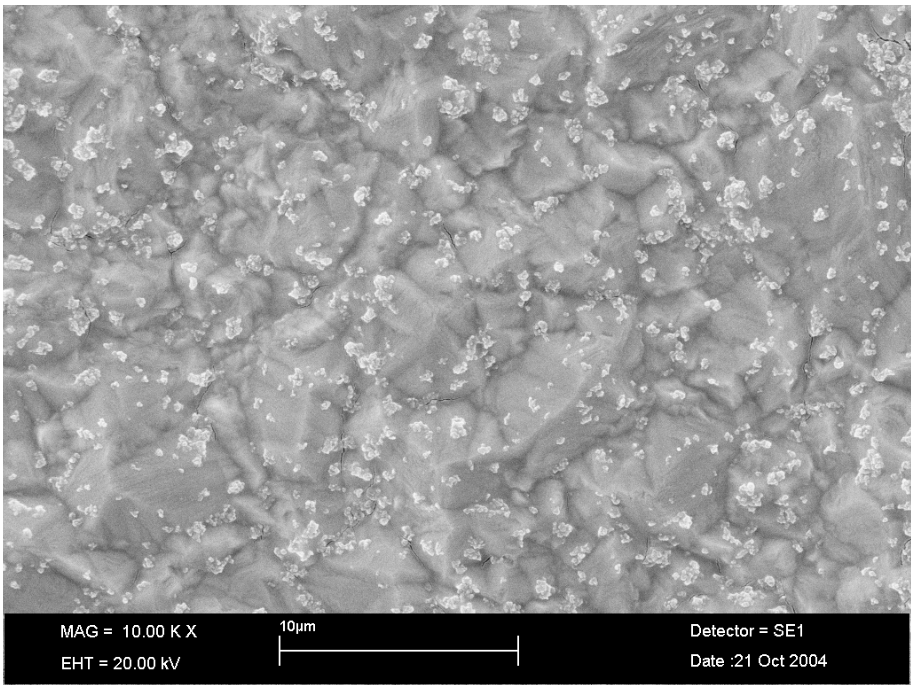

(a) duty cycle 25%

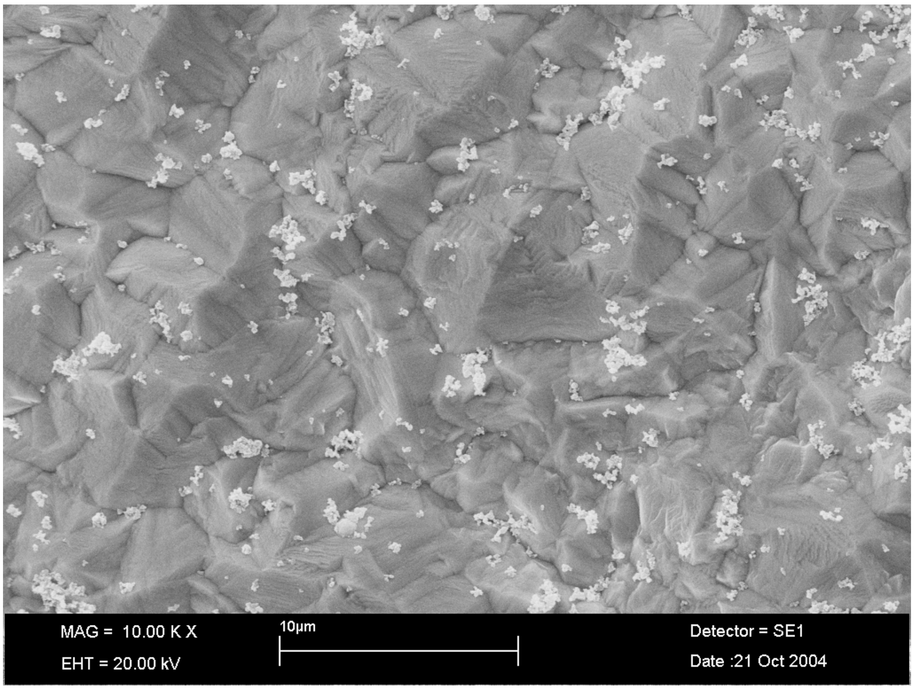

(b) duty cycle 50%

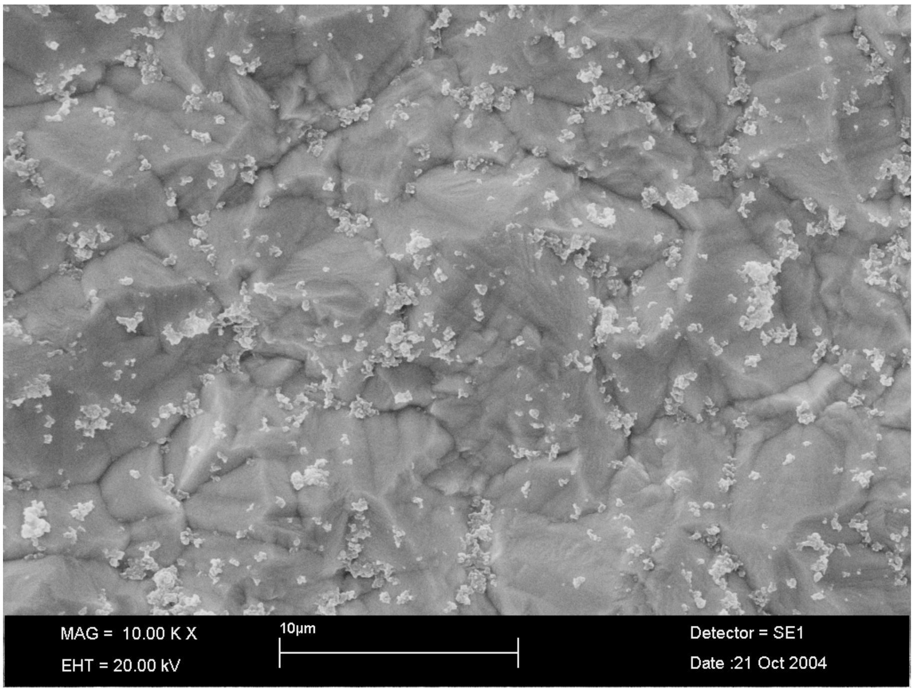

(c) duty cycle 75%

Figure 4.19 SEM surface morphology of Ni-SiC composite coating obtained at different duty cycles

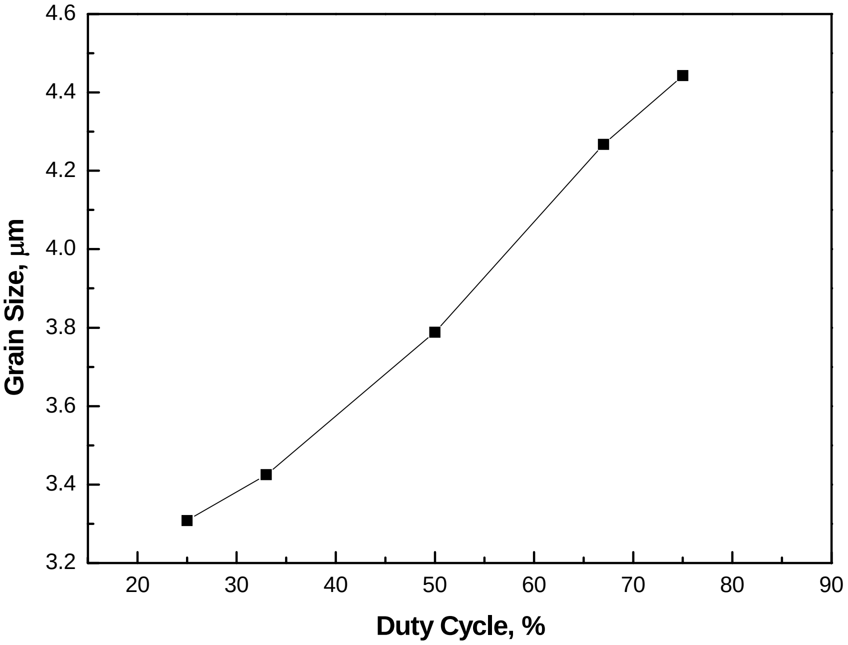

Figure 4.20 The grain size of the nickel matrix as a function of the duty cycle

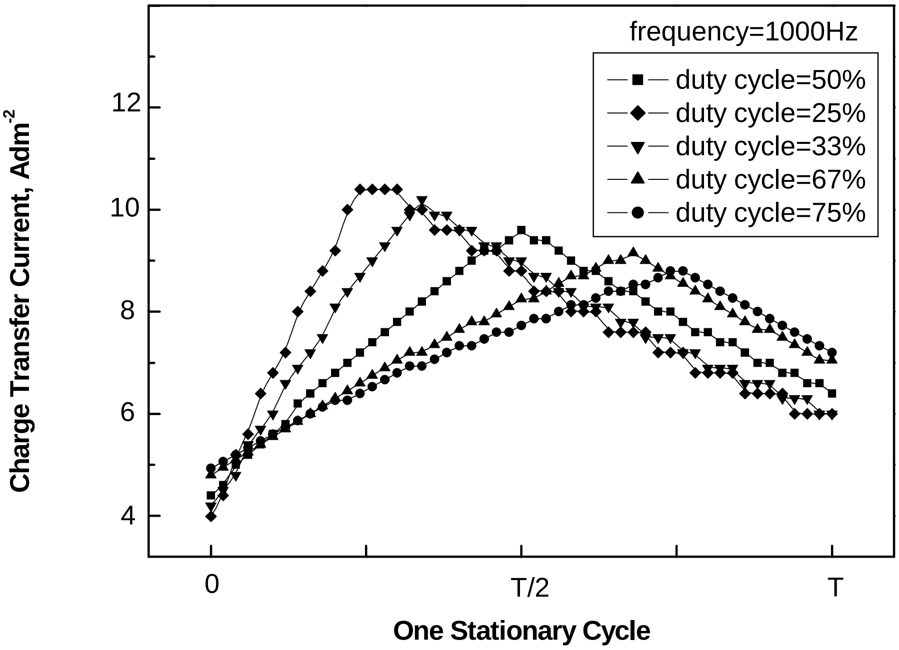
frequency=1000Hz
duty cycle=50%
duty cycle=25%
duty cycle=33%
duty cycle=67%
duty cycle=75%
Charge Transfer Current, Adm-2
4
6
8
10
12
0
T/2
T
One Stationary Cycle

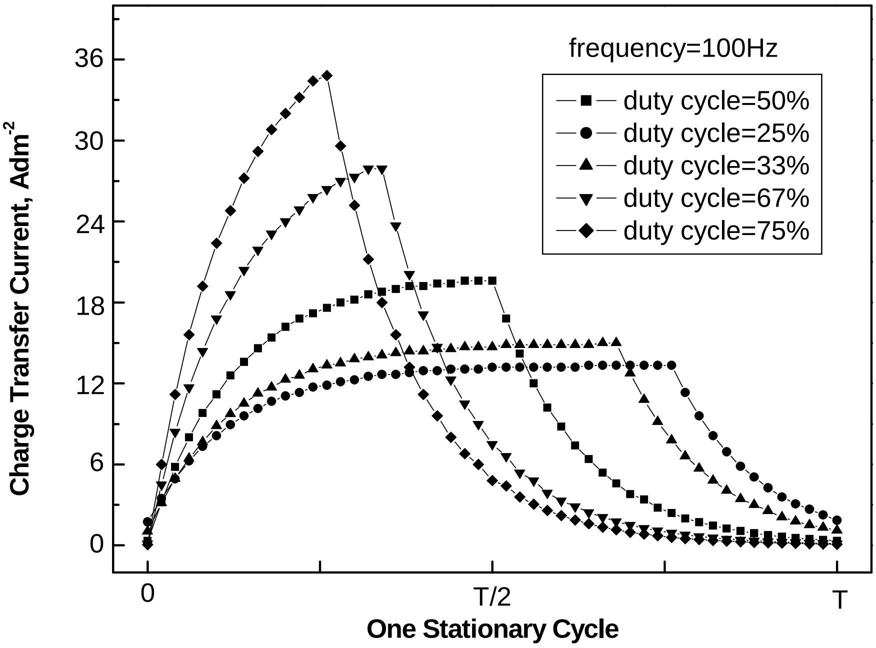
frequency=100Hz
duty cycle=50%
duty cycle=25%
duty cycle=33%
duty cycle=67%
duty cycle=75%
Charge Transfer Current, Adm-2
0
6
12
18
24
30
36
0
T/2
T
One Stationary Cycle

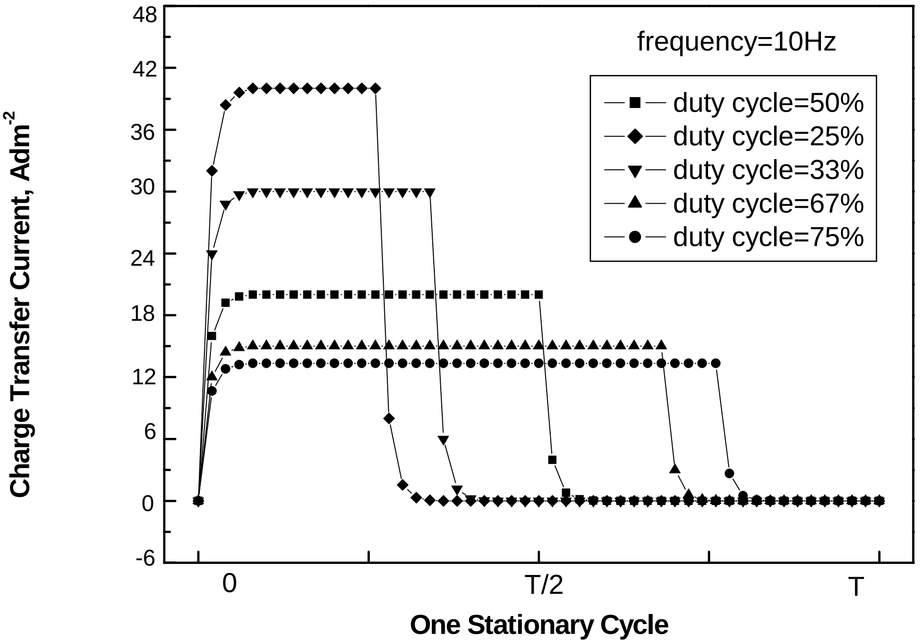

Figure 4.21 The simulation results of charge transfer current under different duty cycles

The influence of pulse duty cycle was reported to be related to the band gap value of a composite CdSe [126], and the duty cycle also affects the electrochemical reaction behaviour [118]. It is known that in pulse electrodeposition, the capacitive effect will affect the current efficiency and the charge transfer current. The equivalent circuit model simulated the charge transfer current under different duty cycles.

Figures 4.17 and 4.21 show the simulation results of the charge transfer current for different duty cycles with frequencies of 10, 100 and 1000Hz. It shows that the charge transfer current reaches the maximum value at the duty cycle of 25%, and the duty cycle of 75% yields the lowest charge transfer current. The simulation results considered the capacitive effect of the electrical double layer on the electrocodeposition behaviour and found that it requires a certain amount of time to charge and discharge, which depends on the current density and the physico-chemical parameters of the system. At different frequencies, the peak currents of charge transfer decrease with increasing frequency. At the frequency of 10Hz, the charge transfer current for Ni-SiC electrodeposition resembles the applied pulse current. It illustrates that the charging and discharging times are short as compared to the on-time and off-time periods. It also shows that at this frequency, the highest charge transfer current is obtained at the duty cycle of 25%. When the frequency increases to 1000Hz, the peak charge transfer current (less than $10Adm^{-2}$ for the duty cycle of 50%) becomes much lower than the applied peak current density ($20Adm^{-2}$ at the same duty cycle). It is because the charging and discharging times of the double layer are much longer than the on-time and off-time of the pulse, respectively, and the pulse current is virtually a direct current, losing the potential benefits of pulse plating. It is worth noting that at the frequency of 100Hz, the peak charge transfer current is about $19Adm^{-2}$ for a duty cycle of 50%, which is close to the applied peak current density of $20Adm^{-2}$, which may result in a high current efficiency.

4.5.3.2 The SiC Incorporation

The SiC volume fractions in the deposits as a function of the duty cycle are measured by X-Ray energy dispersion spectroscopy (EDX), as represented in Figure 4.22. It reveals that the SiC content increases with increasing pulse duty cycle. It is known that the deposition of SiC particles is due to the electrophoretic attraction, by which inert particles (absorbed by nickel ions) are driven to the cathode surface by the Coulomb force, and the SiC volume fraction is related to the current density, particle loadings in the electrolyte, and other deposition parameters. The main difference between pulse plating and direct current plating is the existence of two distinct cathodic diffusion layers. In the immediate vicinity of the cathode, the concentration pulsates with the frequency of the pulsating current, whereas in the outer diffusion layer, cations are supplied towards the cathode during the off-time [174]. As a result, the pulse on-time reflects the adsorption process, and the pulse off-time represents the diffusion process and hydrogen evolution reaction. Assuming the electrodeposition of Ni-SiC composites is a charge transfer controlled process and the influence of off-time is less significant, the SiC volume fraction can be predicted by the Eq. (3.12) as given in Chapter 3.

One of the parameters in the equation is the current density, *I(t)* which can be represented by

$$I_{rec}\left(t\right)=\frac{i_p}{m+1}+\sum_{n=1}^{\infty}\left\{\frac{i_p}{n\pi}\cdot\sin\left(\frac{2n\pi}{m+1}\right)\cos\left(\frac{2n\pi}{T}t\right)+\frac{2i_p}{n\pi}\cdot\sin^2(\frac{n\pi}{m+1})\cdot\sin\left(\frac{2n\pi}{T}t\right)\right\} \quad (4.14)$$

where *m* is the ratio of off-time and on-time. With increasing duty cycle, the *m* value and the peak current density will decrease. Under the same average current density, the current density at different duty cycles can be given by:

$$\begin{aligned}
I_{13}\left(t\right)&=\frac{i_p}{4}+\sum_{n=1}^{\infty}\left\{\frac{i_p}{n\pi}\cdot\sin\left(\frac{n\pi}{2}\right)\cos\left(\frac{2n\pi}{T}t\right)+\frac{2i_p}{n\pi}\cdot\sin^2(\frac{n\pi}{4})\cdot\sin\left(\frac{2n\pi}{T}t\right)\right\}\\
I_{12}\left(t\right)&=\frac{i_p}{3}+\sum_{n=1}^{\infty}\left\{\frac{i_p}{n\pi}\cdot\sin\left(\frac{2n\pi}{3}\right)\cos\left(\frac{2n\pi}{T}t\right)+\frac{2i_p}{n\pi}\cdot\sin^2(\frac{n\pi}{3})\cdot\sin\left(\frac{2n\pi}{T}t\right)\right\}\\
I_{11}\left(t\right)&=\frac{i_p}{2}+\sum_{n=1}^{\infty}\left\{\frac{i_p}{n\pi}\cdot\sin\left(n\pi\right)\cos\left(\frac{2n\pi}{T}t\right)+\frac{2i_p}{n\pi}\cdot\sin^2(\frac{n\pi}{2})\cdot\sin\left(\frac{2n\pi}{T}t\right)\right\} \quad (4.15)\\
I_{21}\left(t\right)&=\frac{2i_p}{3}+\sum_{n=1}^{\infty}\left\{\frac{i_p}{n\pi}\cdot\sin\left(\frac{4n\pi}{3}\right)\cos\left(\frac{2n\pi}{T}t\right)+\frac{2i_p}{n\pi}\cdot\sin^2(\frac{2n\pi}{3})\cdot\sin\left(\frac{2n\pi}{T}t\right)\right\}\\
I_{31}\left(t\right)&=\frac{3i_p}{4}+\sum_{n=1}^{\infty}\left\{\frac{i_p}{n\pi}\cdot\sin\left(\frac{3n\pi}{2}\right)\cos\left(\frac{2n\pi}{T}t\right)+\frac{2i_p}{n\pi}\cdot\sin^2(\frac{3n\pi}{4})\cdot\sin\left(\frac{2n\pi}{T}t\right)\right\}
\end{aligned}$$

where $I_{13}(t)$, $I_{12}(t)$, *I11(t)*, $I_{21}(t)$, and $I_{31}(t)$ are the current density at a duty cycle of 25%, 33%, 50%, 67% and 75% respectively. Substituting the current function into Eq. (1), the SiC volume fractions are calculated and the simulation results are shown in Figure 4.22.

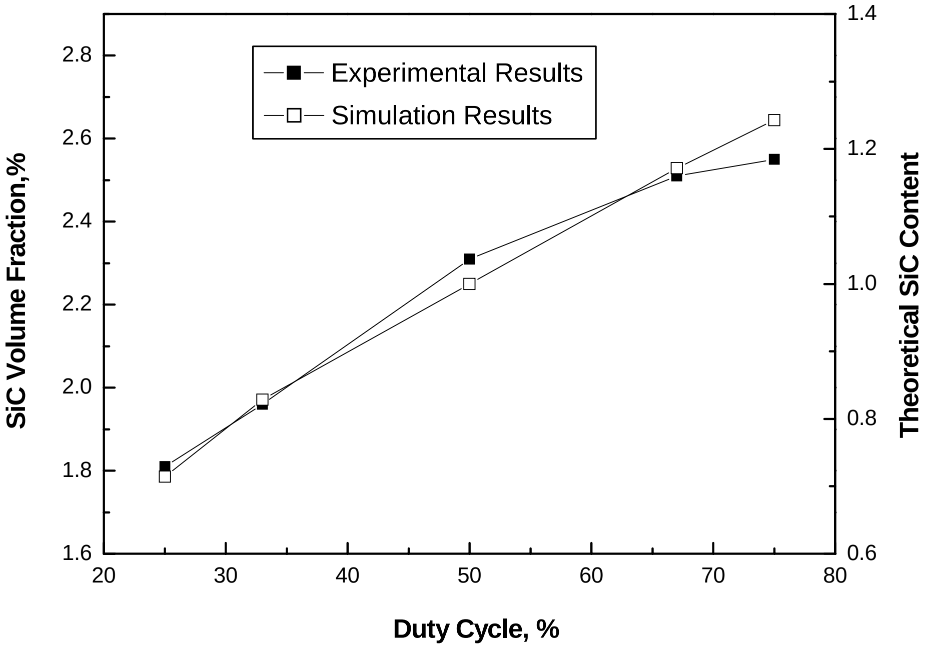

Figure 4.22 The volume fraction of nanosized SiC particles as a function of the duty cycle

4.5.3.3 The Microhardness

The Vickers microhardness of Ni-SiC composites at different duty cycles is shown in Figure 4.23. A maximum hardness value is obtained at the duty cycle of 50%. This can be attributed to the decreased nickel grain size and the increased SiC particle content. Smaller grain sizes will lead to an increased hardness value of the composite according to the Hall-Patch relationship [191]

$$H_v = H_{v_0} + Kd^{-1/2} \tag{4.16}$$

where *H* is the microhardness, *K* is a constant, and *d* is the mean grain size. As the duty cycle increases, the grain size of nickel matrix increases, which is detrimental to the hardness. Conversely, the increased amount of embedded SiC particles due to the increase in duty cycle will increase the hardness of the composite according to the equation

$$H_v = H_{v,SiC} \times SiC\% + H_{v,Ni} \times Ni\% \tag{4.17}$$

Grain size and the SiC content are two competing factors and in the present study, a maximum hardness value of 290HV is obtained at the duty cycle of 50%. Figure 4.24 further illustrates the load-displacement curves obtained by nanoindentation tests for the composite obtained at different duty cycles. The hardness value and the Young's modulus at different duty cycles are also plotted in Figure 4.25. Both the Young's modulus and the hardness achieve their maximum values at a duty cycle of 50% (a maximum hardness value of 2.25GPa and a maximum value for the Young's modulus being 49.03GPa). These findings are in line with the results of microhardness.

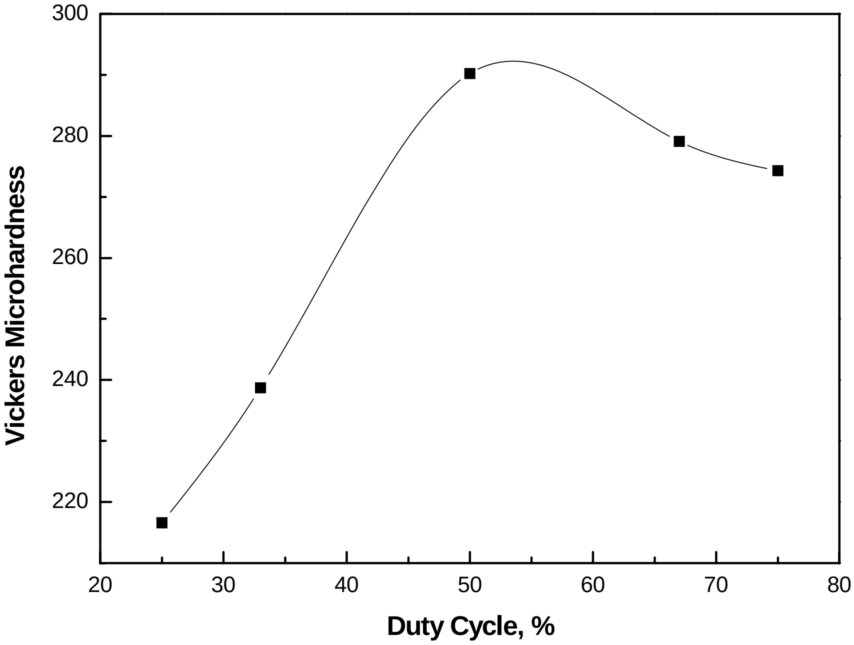

Figure 4.23 Vickers microhardness of Ni-SiC composites under different duty cycles

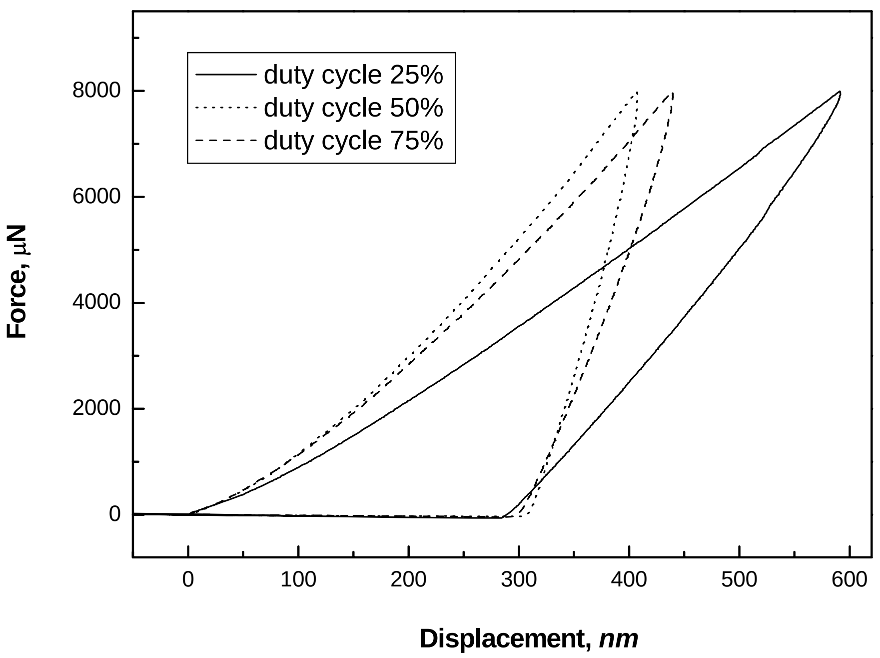

Figure 4.24 Nanoindentation load-depth curves for Ni-SiC composites obtained at different duty cycles

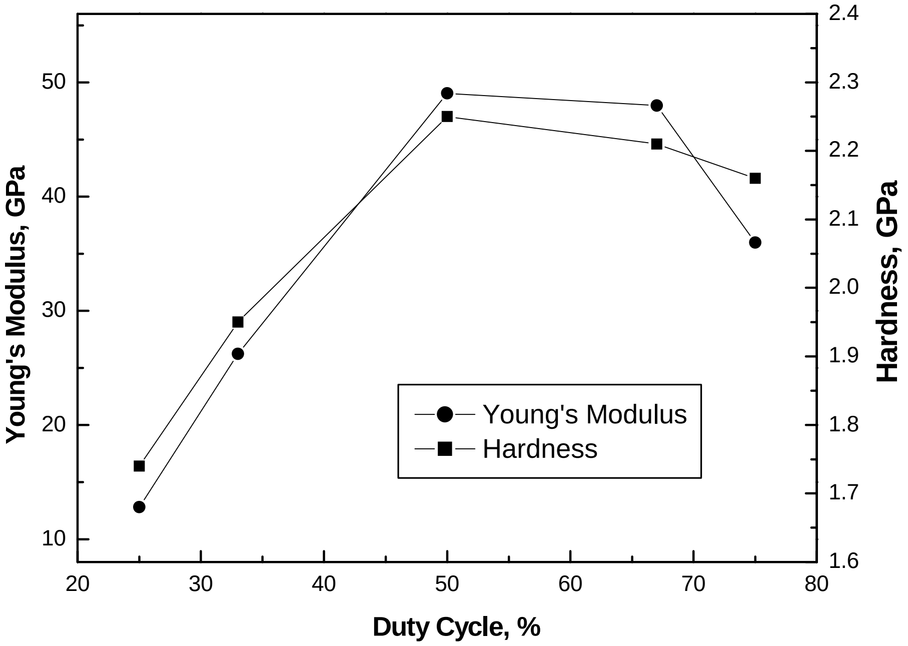

Figure 4.25 The effect of duty cycle on Young’s modulus and hardness of Ni-SiC composites

4.5.4 The Effect of Pulse Frequency

4.5.4.1 Microstructural Analysis

Figure 4.26 compares the nickel grain size of the Ni-SiC composite obtained at $10Adm^{-2}$ and at pulse frequencies of 10, 100 and 1000Hz. The grain size is found to increase with increasing pulse frequency, and the smallest grain size is obtained at the frequency of 10Hz. According to the findings of the equivalent circuit, a high instantaneous current is obtained at high pulse frequencies, and it is well known that high peak currents promote nucleation and fine grains, which can explain the dependence of pulse frequency on grain size.

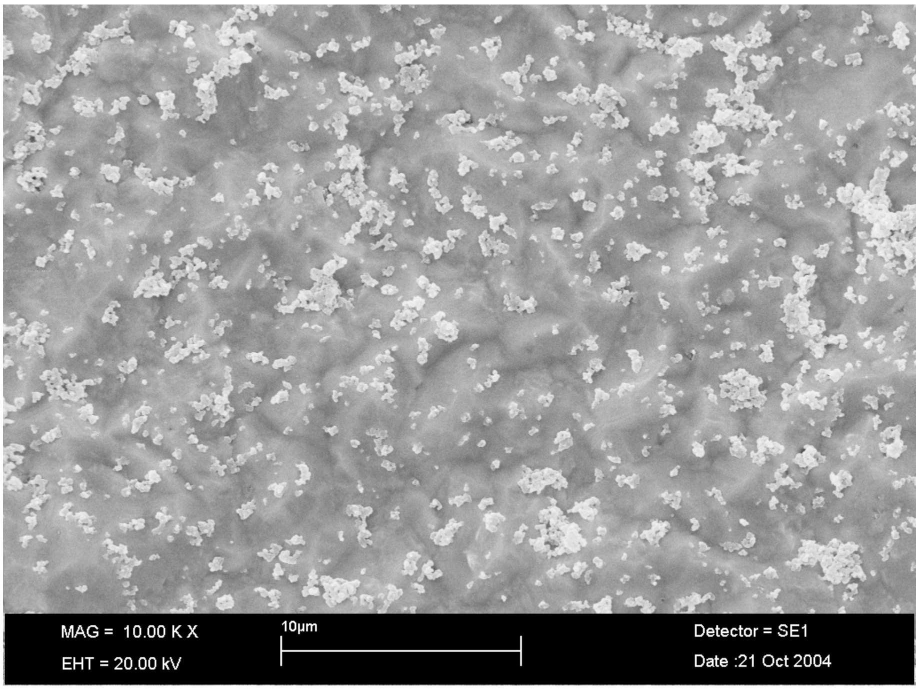

Frequency =10Hz

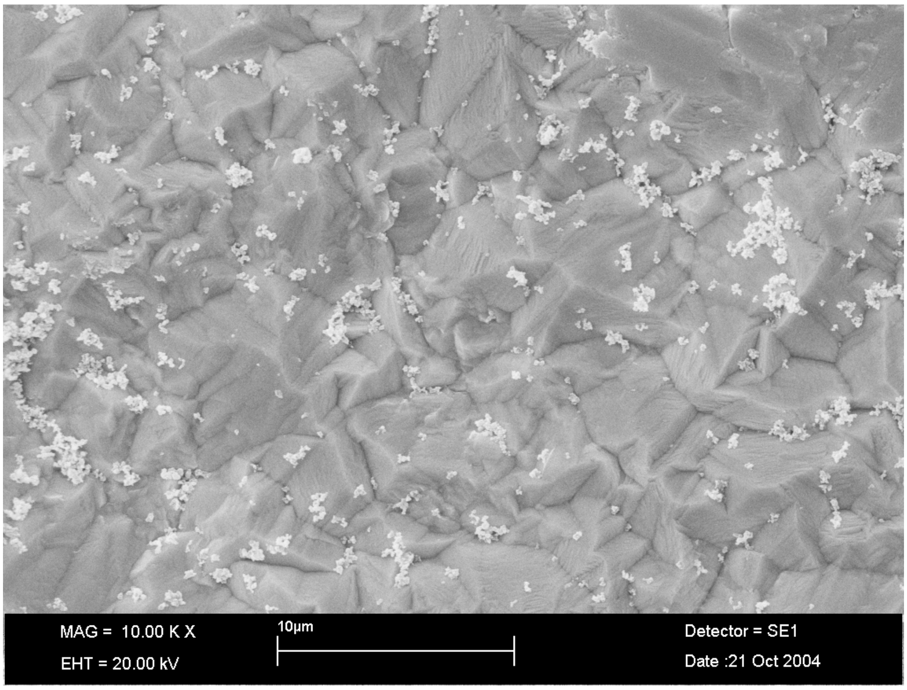

Frequency =100Hz

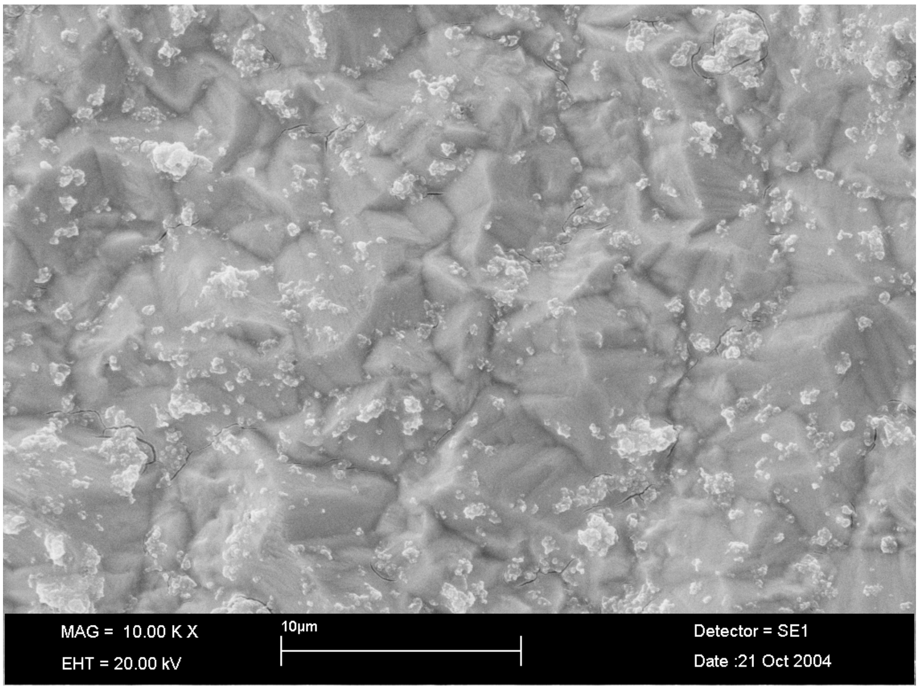

Frequency =1000Hz

Figure 4.26 Effect of pulse frequency on grain size of the Ni-SiC composite

The results of X-Ray energy dispersion spectroscopy (EDX) show that the silicon contents are 2.55%, 2.31%, and 2.43% for the composites obtained at pulse frequencies of 10, 100 and 1000 Hz respectively. It revealed that the pulse frequency has relatively insignificant effect on the volume fraction of SiC.

The volume fraction can also be theoretically simulated by the Eq. (3.12). According to the equation, the SiC volume fraction is related to the current density *I(t)*. As the peak current density, the average current density and the deposition time of the electrodeposition system are the same under different pulse frequencies, the theoretical volume fraction of SiC is independent of pulse frequency.

4.5.4.2 Micro-hardness and Nanoindentation Results

The microhardness values of the Ni-SiC composites are found to increase from 220HV to 280HV when the frequency decreases from 1000Hz to 100Hz, and it slightly increases to 300HV when frequency further decreases to 10Hz. It is well known that the hardness of a composite is related to its microstructure and the presence of second phase [174]. With the same volume fraction of SiC, the increase in hardness of the composite is due to the decrease in grain size. Figure 4.27 further shows the load-displacement curves obtained by the nanoindentation tests for the composites under different pulse frequencies. Based on the indentation depth and the slope of the unloading curves, the hardness and the elastic modulus of the composite can be determined [192~194]. Figure 4.28 shows that both the hardness and elastic modulus increase with decreasing frequency. A high hardness value of 2.25GPa and a high elastic modulus of 49.03GPa are observed in the Ni-SiC composites under the frequency of 10Hz, which is significantly larger than that at a frequency of 1000Hz (with a hardness of 1.69GPa and an elastic modulus of 26.34GPa). This phenomenon is also related to the change in grain size and charge transfer current.

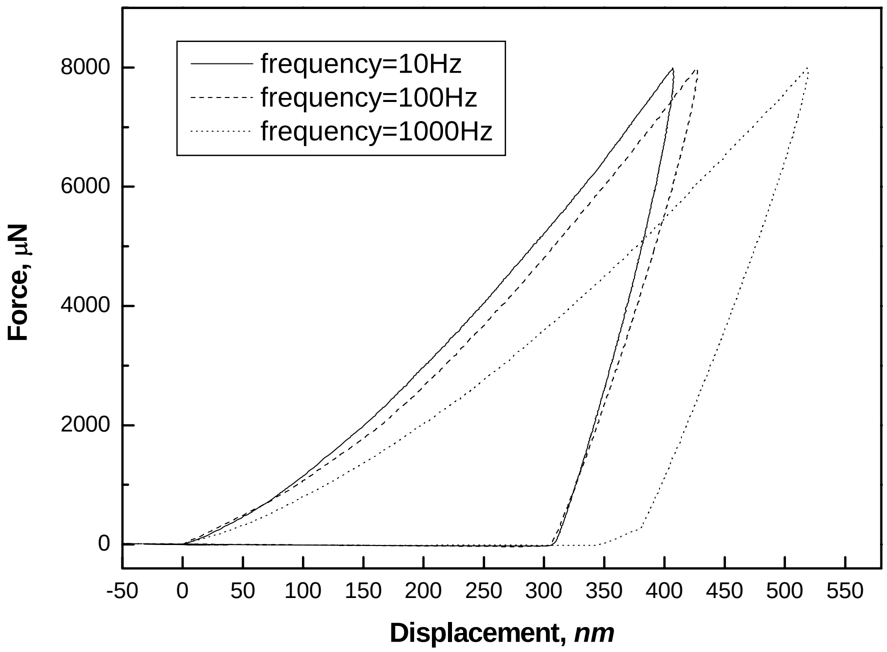

Figure 4.27 Load-displacement curve for the Ni-SiC composite obtained at different pulse frequencies

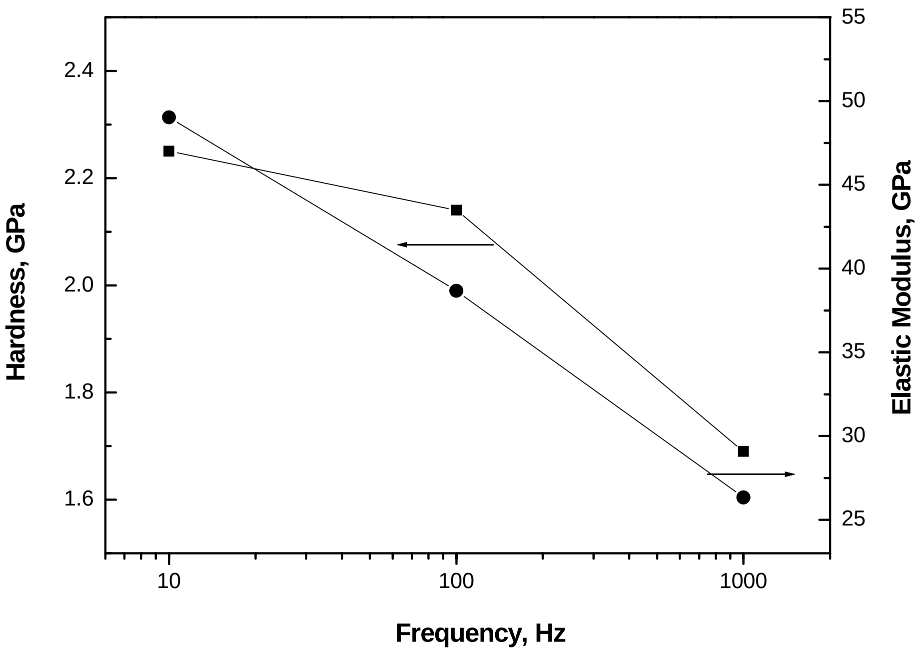

Figure 4.28 Hardness and elastic modulus of the Ni-SiC composite at different pulse frequencies

4.5.5 Conclusions

By varying the duty cycle from 25% to 75%, and pulse frequency from 10Hz to 1000Hz, their effects on morphology, nickel matrix grain size, SiC volume fraction in the deposits, and microhardness were examined and the following conclusions drawn.

(a) Both pulse frequency and duty cycle are shown to have significant influence on both grain size and the mechanical properties of the electrocodeposited Ni-SiC composites, but the volume fraction of SiC is relatively independent of pulse frequency.

(b) The nickel grain size is found to increase with increasing pulse frequency and duty cycle, resulting in a change in microhardness.

(c) An analytical model is applied to examine the effect of pulse parameters on SiC volume fraction. The trend of the prediction is consistent with the experimental findings.

(d) The charge transfer current obtained by the equivalent circuit model reveals that the peak current increases with decreasing pulse frequency and duty cycle. A high peak current favors nucleation and small grain size. The findings are consistent with the experimental observations.

Chapter 5 Effect of Magnetic Field on the Electrocodeposition of Ni-SiC Composites

5.1 Introduction

Current waveforms were shown to have a great influence on the electrodeposition behaviour of Ni-SiC composites, and the equivalent circuit model was proved to be useful to predict the nucleation rate for different current waveforms. In this Chapter, a magnetic field will be introduced in the electrolyte, and its effect of the magnetic field on the codeposition behaviour will be described.

Electrolysis with an imposed magnetic field has been demonstrated to be able to lead to a more uniform deposit compared to that produced by conventional electrolysis [195~197]. Early findings have illustrated that the magnetic field will improve mass transfer in electrolyte, which will result in better deposit qualities. It was reported that the limiting current density for electrodeposition of copper, nickel and nickel-iron significantly increased with the presence of magnetic field [198, 199], and the hardness has been significantly increased. Chiba et al. [150] have also examined the effect of magnetic fields on crystallographic orientations of nickel. The research work in the area of magnetoelectrolysis has been reviewed extensively by Fahidy [200] and Tacken and Janssen [165].

It is generally agreed that the effect of a magnetic field is attributed to the magnetohydrodynamic effect due to the enhanced convection process induced by the Lorentz force. Based on experimental results, some empirical equations were developed to describe the relationship between mass transport limiting current, i_B and magnetic field, **B** in electrodeposition of metals and alloys [166]. Aogaki et al. also showed that i_B varied with $\mathbf{B}^{1/3}$, and an empirical equation describing the effect of strong magnetic field on mass transport limiting current for electrodeposition on disk platinum electrodes using chronoamperometry was developed by Legeai et al. [166]. An in-depth analysis to enable us to understand the detailed mechanisms of the effect of magnetic field has yet to be done.

The influence of magnetic field in electrodeposition of composites has less been investigated. It is considered that the codeposition process of inert particles and metal is able to be controlled by regulating the magnetic field strength [162]. Nevertheless, more research is needed in order to better understand the effect of magnetic fields on the incorporation of particles and deposition mechanisms of electro-composites. With the aim to improve the properties of the electro-composites by controlling their microstructure, the effect of magnetic fields on surface morphology, crystal orientation and the SiC content of the Ni-SiC composites will be examined for the first time.

5.2 Experimental

In this Chapter, a two-electrode glass cell for nickel deposition with an electrolyte volume of 100ml was used. A stainless steel cathode mandrel with dimensions of 30mm × 15mm × 1mm, and a stainless steel anode electrode. The experimental setup is shown in Figure 5.1. A stable and uniform magnetic field with a strength of 0.3T was generated using an electric magnet with an input DC voltage of 37.5V and a current of 8.5A. Electrodeposition was conducted in the magnetic field perpendicular to the electrode surface. The composition of the bath solution was nickel sulphamate 330g/l, nickel chloride 15g/l, boric acid 30g/l and SDS 1g/l. An amount of 40g/l of SiC particles (β SiC) of diameter about $100\,nm$ was added. The electrolyte was agitated by a mechanical stirrer, temperature was kept at 50℃, and the initial pH of the electrolyte was 4.2, which is a typical value used in electroplating.

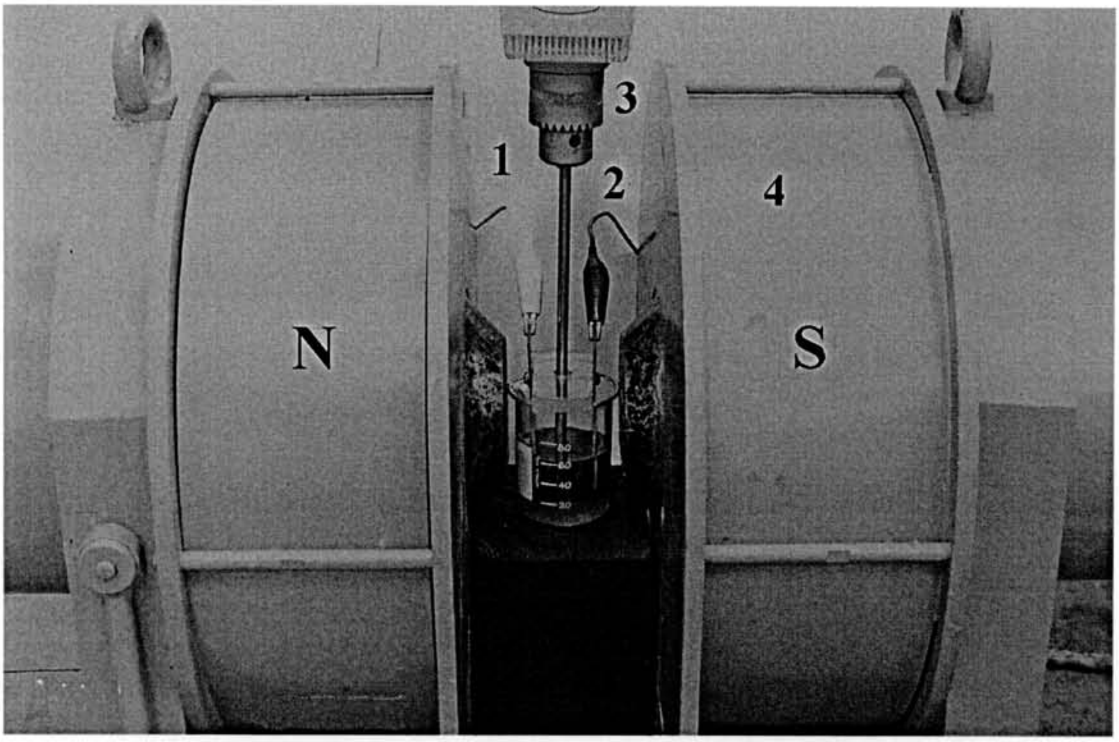

Figure 5.1 The experimental setup – (1) cathode; (2) anode; (3) stirrer; (4) electric magnet with a cooling system. A magnetic field of 0.3T is generated by the electric magnet with an input DC voltage of 37.5V and a current of 8.5A. The magnetic field is perpendicular to the electrode surface.

Electrochemical impedance spectra (EIS) of the deposition system were acquired in the frequency range of 30kHz to 5mHz with a 10mV amplitude sine wave generated by a frequency response analyzer, and a thin layer of composite was deposited before each set of measurements. A three-electrode setup was used in the electrochemical measurements, and the reference electrode was a Ag/AgCl electrode with KCl saturated aqueous solution. The data obtained were corrected for ohmic drop. After electroplating, scanning electron microscopy (SEM, Leica Steroscan 440) and EDX was used to study the surface morphology and composition of the Ni-SiC composite. The preferred crystal orientation was measured by XRD using the $Cu-K\alpha$ line (X'Pert, Philips, 40kV, 30mA). In order to evaluate quantitatively the preferred orientation, an orientation index was used and the calculation method was based on Ref. [161].

5.3 Electrochemical Characteristics

5.3.1 Linear Sweep Voltammetry

The voltammogram of the Ni-SiC electrodeposition system with and without a magnetic field is shown in Figure 5.2. Without a magnetic field, the polarization curve has three typical electrochemical regions: the activation region at low overpotentials, the mass transfer region (characterized by the current plateau) and the third region characterizing hydrogen evolution (with the cathodic potential higher than -1.4V). With a magnetic field of 0.3T, a rapid increase in current is observed when the cathodic potential is less than -0.6V vs. Ag/AgCl, and no current plateau is observed. Similar results are also reported for the electrodeposition of Ni-Fe alloy in magnetic fields ranging from 0T to 0.9T [152], and in copper electrodeposition from 0T to 0.178T [153].

This phenomenon can be attributed to the magnetohydrodynamic (MHD) effect which enhances the convection process (as well as the motion of ions and particles) in the electrolyte, leading to an increase in Faradaic current and limiting current. A higher limiting current density is shown to result in an increase in current efficiency and a more uniform current distribution, which will improve the physical and mechanical properties of the deposits [152, 201, 202]. It is generally known that the mass transport process is related to the thickness of diffusion layer, δ and its value is determined by the limiting current density through the equation: $j = \frac{nFDc}{\delta}$, where n, F, D, c are constant [205]. A higher limiting current obviously reduces the thickness of the diffusion layer, and Danilyuk et al. [153] even believed that the diffusion layer is essentially reconstructed due to the MHD effects.

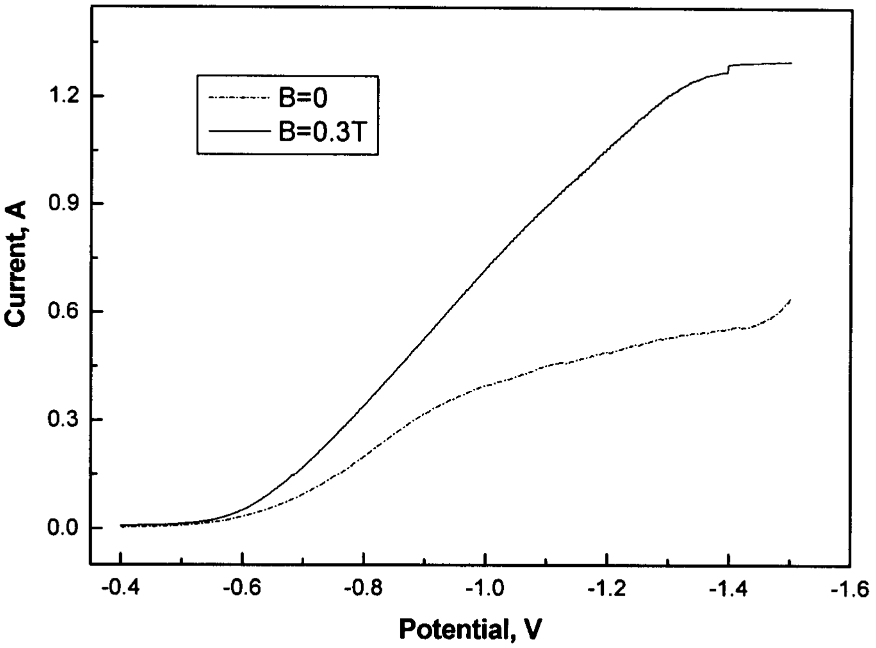

Figure 5.2 Current-potential curves for Ni-SiC electrodeposition with and without magnetic field vs. reference electrode Ag/AgCl.

5.3.2 Impedance Analysis

The electrodeposition of metals is an adsorption and crystallization process. With the change of mass transport process and limiting current density, the reduction reactions are expected to be more complicated. In order to understand the process, the electrochemical impedance spectra are examined. Figure 5.3 gives the Nyquist plots of EIS curves with and without magnetic field at the cathodic potential of -700mV, and they are corrected for the solution resistance. The capacitive loop under the magnetic field of 0T is a half circle. While the capacitive loop for the magnetic field of 0.3T is depressed, the capacitive loop for 0.5T is more distorted. The shape and characteristics of the impedance spectra which are related to the cathodic reactions are shown to be affected by the magnetic field. In fact, in copper electrodeposition system, the transformation from one capacitive loop to two indistinguishable capacitive loops was also observed [201], and the author proposes a pseudocapacitance to illustrate the depressed capacitive loop.

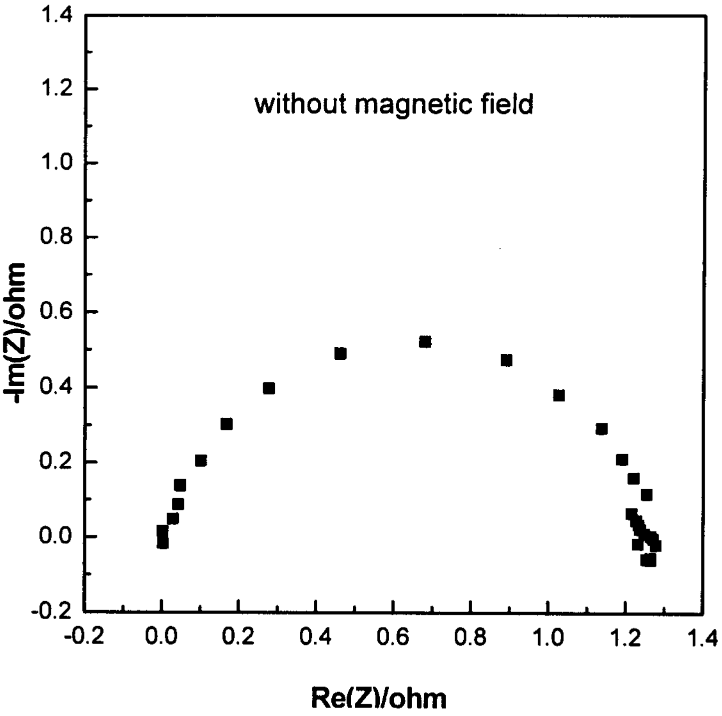
without magnetic field
-Im(Z)/ohm
Re(Z)/ohm
-0.2
0.0
0.2
0.4
0.6
0.8
1.0
1.2
1.4

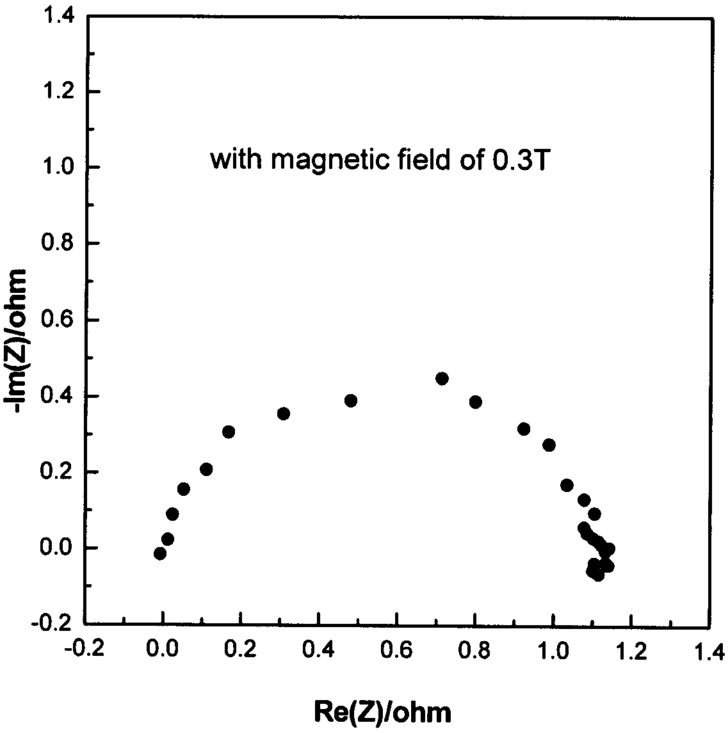
with magnetic field of 0.3T
-Im(Z)/ohm
Re(Z)/ohm
-0.2
0.0
0.2
0.4
0.6
0.8
1.0
1.2
1.4

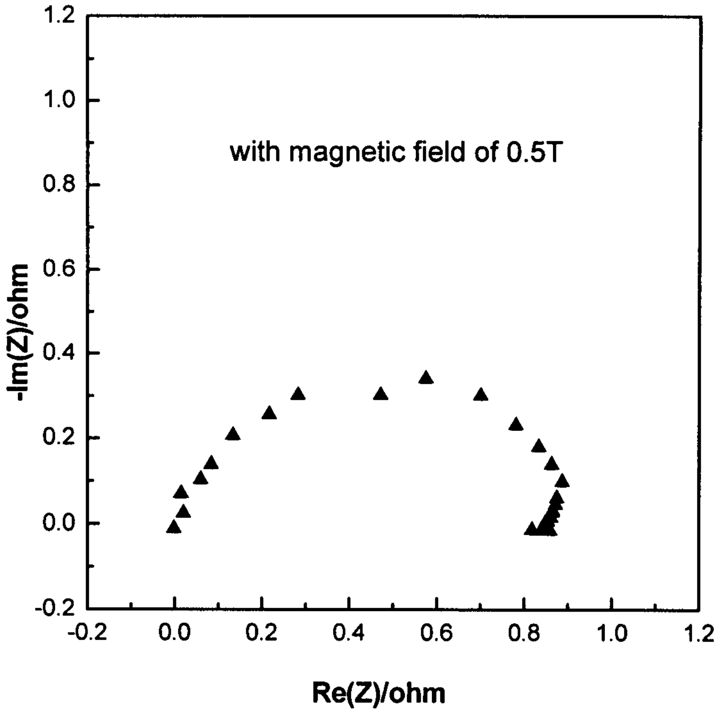

Figure 5.3 Nyquist plots of Ni-SiC electrodeposition system at the cathodic potential of -700mV vs. reference electrode

Based on the equivalent circuit of Ref. [201], the EIS curves at different cathodic overpotentials ranging from -600mV to -1050mV were best fitted by the software ZsimpWin to obtain the charge transfer resistances and the double layer capacitances. The results are shown in Table 1. It is worth mentioning that the time constant of the first loop is higher than that of the second one, and the first charge transfer reaction is believed to be the determining step in the electrocodeposition process under a magnetic field. Table 1 shows that the charge transfer resistance is changed by the magnetic field. Similar phenomenon was observed by other researchers. Devos et al [162] found a decrease of R_{ct} from 7.6Ω at 0.15T to 4.0Ω at 0.9T in the zinc electrodeposition system. For nickel electrodeposition, the amplitude of the capacitive loop also increased with increasing magnetic field [155]. Msellak et al [152] also observed that the amplitude increased when the magnetic field increased from 33Ω at 0T to 39Ω at 0.9T in Ni-Fe alloy codeposition. It is also worth pointing out that the product of the charge-transfer resistance and the electrolysis current is approximately constant in the whole overpotential range, which illustrates that the magnetic field does not affect the charge transfer coefficient. Similar phenomena were reported by other researchers [152, 155, 162]. However, the data obtained from the study is far from sufficient to explain and enable us to understand the effect of a magnetic field on charge transfer kinetics, and more work has yet to be done.

Table 5.1 The charge transfer resistances and double layer capacitances obtained for the Ni-SiC electrodeposition system with and without magnetic field

B (T)	$-\eta$ (mV)	R_{ct} (Ω)	C_{dl} (μ F)	$R_{ct}I$ (V)	Chi Squared Value
0	600	1.782	373.6	0.0597	0.0004954
	700	1.555	395.8	0.1477	0.001229
	800	0.6273	661.3	0.1261	0.0026
0.3	600	1.246	382.4	0.0645	0.0009928
	700	0.8644	540.1	0.1456	0.001757
	800	0.3406	716.4	0.1165	0.00958

The presence of magnetic fields also changes the features of the inner cathodic surface, which can be estimated by the double layer thickness between the metal and electrolyte. In a parallel plate, the thickness of double layer, x_d, can be expressed by the equation [204]: $x_d = \frac{\varepsilon\varepsilon_0 A}{C_{dl}}$, where ε is the relative permittivity of the medium and ε_0 is the permittivity of free space. As a larger value of C_{dl} is obtained with an external magnetic field as shown in Table 1, the thickness of the double layer will be slightly reduced according to the above equation.

5.4 Crystal Orientation

XRD patterns were obtained for the Ni-SiC composites, and under all the testing conditions, the relative intensity of the (200) orientation is the largest. Figure 5.4 summarizes the intensity of the (200) orientation at different current densities without and with a magnetic field of 0.3T. It is clear that the intensity of the (200) orientation with the magnetic field is significantly higher than those without any magnetic field. Such an increase can be attributed to the MHD effect. The electrocrystallization of nickel is known as a highly inhibiting process and the (200) texture mode of crystal growth is inhibited by chemical species, such as nickel hydroxide and hydrogen ions [205]. As discussed above, the magnetic field of 0.3T reduces the thickness of diffusion layer, which will result in the enhancement of hydrogen evolution [160], and the concentration of hydrogen ions close to the cathode surface is consequently reduced. The electrocrystallization process becomes less inhibited, and it favors the formation of (200) grains. Without any magnetic field, a minimum intensity is observed at the current density of 4Adm^{-2}. The change of the (200) orientation index is attributed to the change in the amount of inhibiting chemical species. As the intensity of the (200) orientation decreases with increasing current density when the current density is below 4Adm^{-2}, the amount of inhibiting species should increase with increasing of current density. However, it is expected that the amount will decrease when the current density is above 4 Adm^{-2} as the intensity of the (200) orientation increases. It is interesting to note that at the current density of 10Adm^{-2}, about the same intensity is obtained with or without a magnetic field. It is considered that such a high current density induces a very significant hydrogen evolution process, and the influence of the magnetic field on the process becomes secondary.

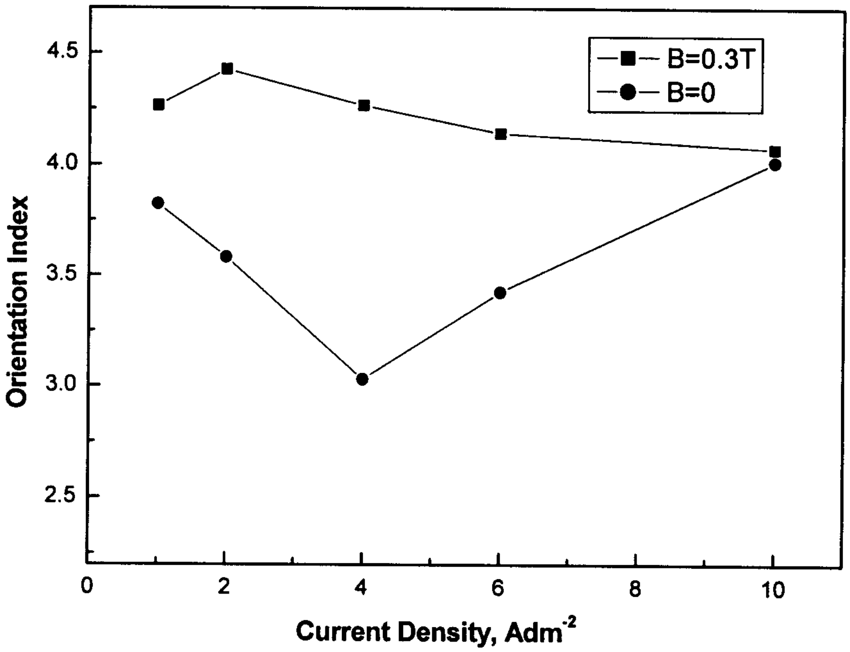

Figure 5.4 Dependence of (200) orientation index on current density in Ni-SiC electrodeposition

5.4 Morphology and Composition

Figure 5.5 shows the surface morphologies of the Ni-SiC composites obtained at current densities of 1, 4, 10Adm^{-2} without any magnetic field. The surface morphologies are found to be influenced by the current density as the values of surface roughness decrease with increasing current density. Pyramidal grains and rough composite surface are observed at the current density of 1Adm^{-2}, and a flat surface with roundish grains is observed at the current density of 10Adm^{-2}. The average SiC content of the composites is about 1.22 at.%.

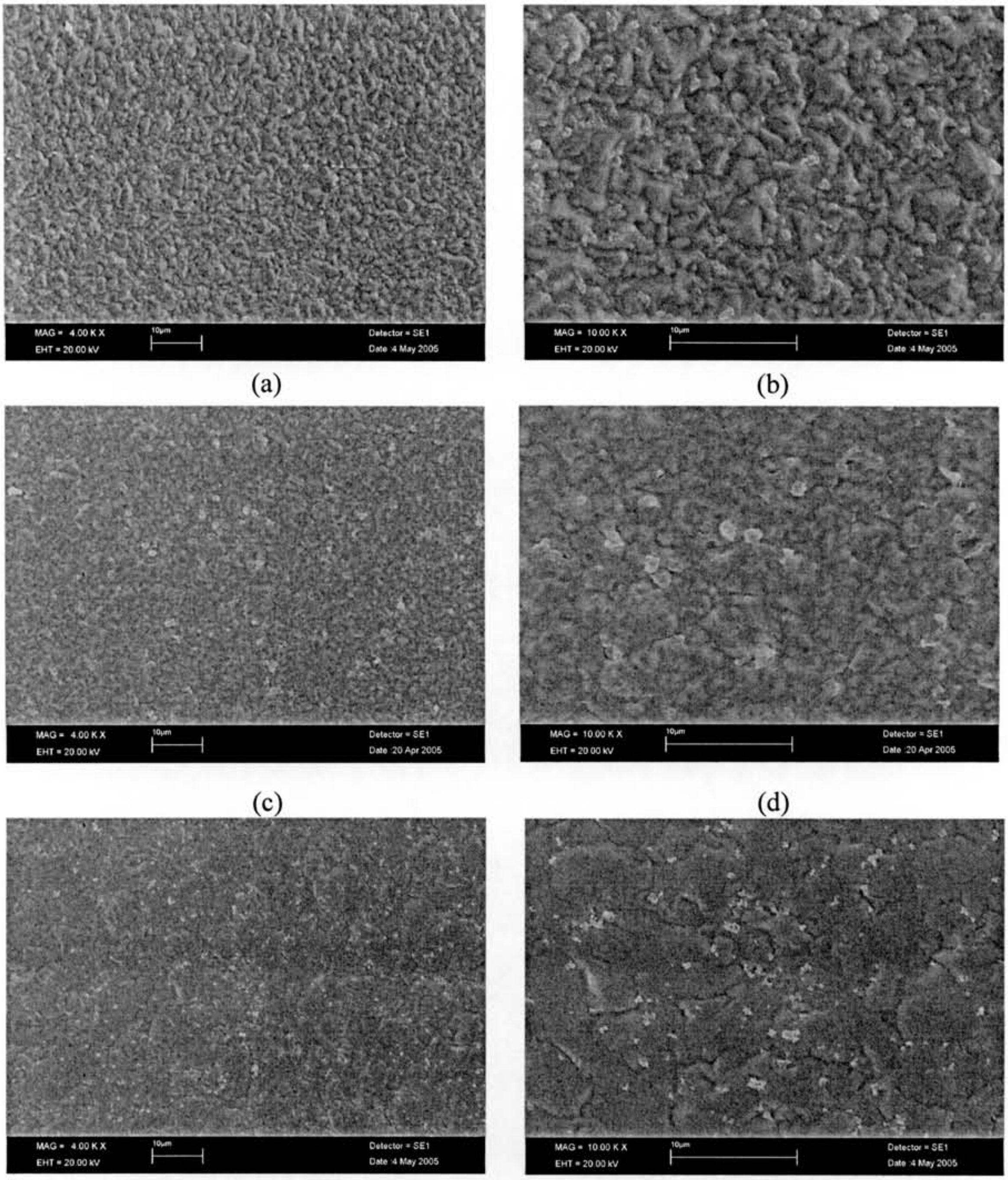

(a) (b)

(c) (d)

(e) (f)

Figure 5.5 SEM micrographs of Ni-SiC deposits obtained in the two-electrode cell with 100 ml of sulphamate bath and without external magnetic field. Current density: (a, b) 1; (c, d) 4; (e, f) 10 Adm^{-2}. Magnification: (a, c, e) 4000×; (b, d, f) 10000×.

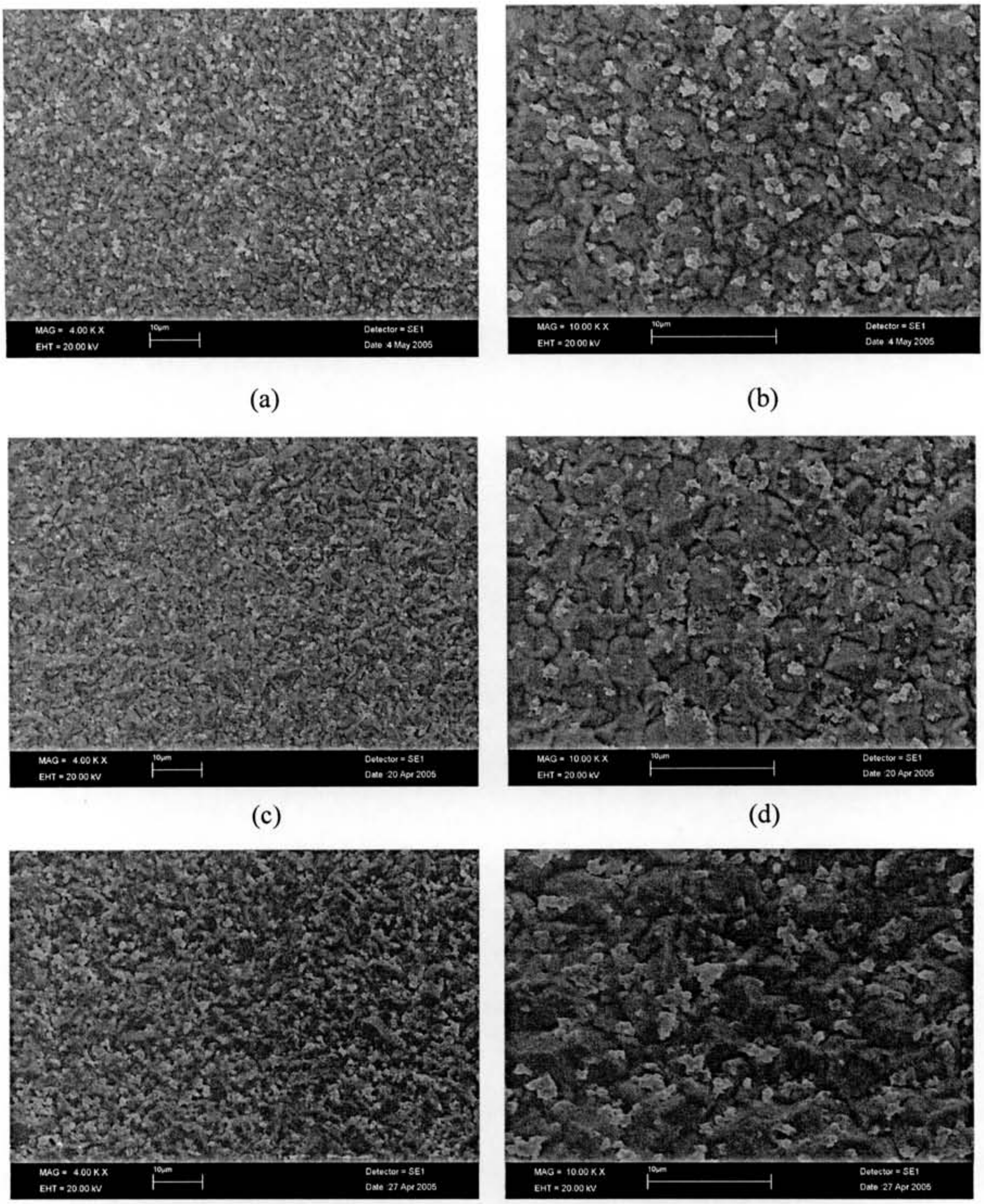

(a) (b)

(c) (d)

(e) (f)

Figure 5.6 SEM micrographs of Ni-SiC deposits obtained in the two-electrode cell with 100 ml of sulphamate bath and with a magnetic field of 0.3T. Current density: (a, b) 1; (c, d) 4; (e, f) 10Adm^{-2}. Magnification: (a, c, e) 4000×; (b, d, f) 10000×.

With the aid of an external magnetic field of 0.3T, the surface morphologies obtained under current densities of 1, 4, 10Adm^{-2} are shown in Figure 5.6. The nickel matrix grains are modified by the magnetic field (as compared to the morphologies as shown in Figure 5.5). It is probably due to the change of reduction passage of nickel ions. The Lorentz force drives the ions around a magnetic flux. Without the magnetic field, the ions are transferred from the anode to the cathode, and the direction of transfer is only normal to the cathode mandrel. Moreover, the incorporation of SiC particles is greatly improved in the presence of a magnetic field, and the particle codeposition process may also interfere with the electrocrystallization of nickel and modify the surface morphology of Ni-SiC composites.

Compared to the composites synthesized without a magnetic field, the amount of SiC particles in the composites are greatly enhanced to an average content of 3.26 at.%. It is known that SiC particles do not exist solely in the electrolyte solution. They are adsorbed by nickel ions, transported to the cathode and deposited with the reduction of nickel ions. The SiC particles are actually charged particles and influenced by applied fields. The increase in SiC content might be explained by the MHD effect in terms of the Lorentz force and the charge transfer process. The Lorentz force enhances the convection process which is favourable for maintaining the suspension of particles and transporting them to surface of the electrode. It will offer a higher chance for the SiC particles to make contact with the cathode electrode, and to be embedded in the deposit. On the other hand, the MHD effect increases the limiting current, and also the rate of charge transfer. The codeposition phenomenon is explained as a competition process between particle adhesion and removing [12], and the codeposition mechanism is also explained as a charge transfer controlled process [46, 47]. In the present work, a higher charge transfer rate is obtained under the same current density. As suggested by the Guglielmi's model, it will result in a more rapid process for incorporation of particles in the composite [173]. The investigation of magneto-electrolysis is significant for both industrial and academic value. It may open up a novel method to modify the microstructure, in particular the particle content, by controlling the magnetic fields with no need to adjust additives and bath composition throughout the process.

5.5 Conclusions

The effect of magnetic field of 0.3T on electrodeposition behaviour and microstructure of Ni-SiC composites was studied in a sulphamate bath. Based on the impedance analysis, the magnetohydrodynamic effect is shown to be significant in improving the mass transport process and accelerating the charge transfer rate. It is found that the surface morphology and grain orientation of the composites are modified by the magnetic field of 0.3T. A significant increase of SiC content is also observed in the composites with the magnetic field, and this is attributed to the improvement of the convection and charge transfer process. The study presents a novel, and alternative method to modify the microstructures of the composites and enhance the content of embedded particles.

6. Overall Conclusions

The effect of different shaped current waveforms on the electrocodeposition behaviour of Ni-SiC composite has been experimentally and theoretically investigated. According to the experimental findings, the largest amount of SiC embedded in the deposit was obtained when a rectangular waveform was used. Guglielmi's model was successfully applied to predict the volume fraction of SiC embedded in the nickel matrix under different waveforms by proposing that a waveform of arbitrary shape can be represented by a Fourier series and that it consists of an infinite number of very short rectangular pulses. The nickel grain size was found to relate to different shaped current waveforms, which cannot be explained by the conventional nucleation rate. An equivalent circuit model based on the electrochemical impedance spectroscopy results can successfully explain the deposition behaviour of the electro-composites under different processing conditions. The simulated instantaneous current passing through the charge transfer resistor is much higher than that of direct current. The double layer in direct current electrodeposition makes no contribution to the charge transfer reactions. While under different shaped current waveforms, it can discharge current in the time-off period, and thus continue the charge transfer reactions. The equivalent circuit model also predicts the capacitive and faradaic currents of the process, and with the same average current densities, the ramp-up waveform has the highest instantaneous peak current for charge transfer and the rectangular waveform produces the lowest instantaneous peak current.

By varying the duty cycle from 25% to 75% and the frequency from 10Hz to 1000Hz, the effect on morphology, nickel matrix grain size, SiC volume fraction in the deposits, and microhardness were examined. Experimental results show that pulse frequency and duty cycle have a significant influence on both grain size and mechanical properties of the co-electrodeposited Ni-SiC composites, but its volume fraction of SiC is relatively independent of pulse frequency. The charge transfer current obtained by the equivalent circuit model reveals that the peak current density increases with decreasing duty cycle and frequency. And the SiC volume fraction increases with an increase in the duty cycle. As a result, a higher hardness value of 290HV is obtained at a duty cycle of 50% and a frequency of 100Hz. The results of the nanoindentation test further confirm the influence of pulse parameters on hardness and elastic modulus of the composite.

The effect of magnetic field on electrodeposition behaviour and microstructure of Ni-SiC composites was studied. Based on the impedance analysis, the magnetohydrodynamic effect is shown to be significant in improving the mass transport process and accelerating the charge transfer rate, It was found that the surface morphology and grain orientation of the composites are modified by the magnetic field. A significant increase of SiC content is also observed in the composites with the magnetic field, and it is attributed to the improvements of the convection and charge transfer process. The study presents a novel alternative method to modify the microstructures of the composites and enhance the content of embedded particles.

The findings of the paper are of significance as it may also be also possible to control the microstructures and to enhance the deposit quality of the electro-composite by manipulating the current waveform and magnetic field during the electro-deposition process.

7. Future Work

After the completion of this body of work, there are still some concerns of electrodeposition that need to be addressed.

7.1 Complex Waveforms

It was shown in Chapters 4&5 of this thesis that the shape of current waveform has great influence on the electrodeposition behaviour of Ni-SiC composites. It will be of significant interest to further examine the effects of other complex waveforms (such as the spike current, the sine shaped waveform, square-wave pulse current) in the electrodeposition process. This will further enhanced the understanding of the electrodeposition mechanisms of Ni-SiC composites.

7.2 Magnetic Field

The magnetic field has been demonstrated in Chapter 5 to have a significant effect on electrodeposition behaviour. The magnetic fields are able to control the magneto-hydrodynamic conditions to get different microstructures and SiC incorporation. Research effort is currently underway on low magnetic fields in a position parallel to the cathode surface. It will be of great interest to study the electro-codeposition behaviour under higher magnetic fields, and also different positions in relation to the cathode surface.

7.3 Tailored Microstructure with Enhanced Properties

There have been a number of attempts to produce gradient composites by electrodeposition through manipulation of current density and particle loading in the bath. Based on the findings of the above investigations, further attempts can be made to produce tailored microstructures for enhanced mechanical properties and deposit quality using two additional process variables: magnetic field and current waveform in a single or multiple step deposition process. It is intended not to adjust additives, bath composition or volume percentage of particles continuously during the process in order to minimize environmental problems.

Although recent studies indicate that the Ni-SiC composites can lead to significant enhancement of hardness, and further improvement in the hardness can be achieved by incorporation of inert particles. However, there are very few studies on the other properties, such as wear resistance and anti-corrosion. Therefore, more work should be done to address the influence of particles on mechanical properties.

8. Statement of Originality and Contribution to Knowledge

Electro-composites that consist of inert particles and a metal have demonstrated that they possess many enhanced properties compared to metals or alloys. A significant amount of research has been conducted to improve the deposit quality of electroforms. Most of them have attempted to adjust the bath composition and pulse currents. The present study is the first to apply shaped current waveforms on electrocodeposition of nickel matrix composites. As compared to the conventional pulse current technique, the shaped current waveforms are shown to result in an improvement in morphology and hardness of composites. The results of this thesis have shown that the finest grain size and the highest hardness are found by using a ramp-up waveform, as compared to those obtained under rectangular, triangular, and ramp-down waveforms with relaxation time. This can be explained by the fact that the ramp-up waveform produces the highest instantaneous peak current for charge transfer. An analytical model is proposed to predict the volume fraction of SiC particles in the electro-codeposition process under waveforms with arbitrary shape, and the trend of the prediction is in agreement with the experimental results.

The present study is also the first to establish an equivalent circuit model to explain the effect of shaped current waveforms on the deposition behaviour of composites. The use of the equivalent circuit model is shown to be useful in describing the deposition behaviour, through which the process kinetics, as charge transfer reactions and adsorption and desorption processes, can be represented.

The magnetic field was shown to be great influence on electrodeposition of metals and alloys, and the present study is the first to apply the magnetic field to the electrocodeposition system. It is found that the magnetic field is an alternative tool to get different microstructures and SiC incorporation in the nickel matrix by controlling the magnetohydrodynamic conditions.

References

1. J.M. West, *Electrodeposition and Corrosion Processes*, Van Nostrand Reinhold, New York, 2nd edition, 1971.
2. G.D. Wilcox, and D.R. Gabe, Faraday's laws of electrolysis, *Transactions of the Institute of Metal Finishing*, 1992, 70(2), pp. 93-94.
3. D. Barker, and F.C. Walsh, Applications of Faraday's laws of electrolysis in metal finishing, *Transactions of the Institute of Metal Finishing*, 1991, 69(4), pp.158-162.
4. J. Downes, *The Electrodeposition of Zinc and Zinc Cobalt Alloys*, PhD thesis, University of Nottingham, 1994.
5. E. Raub and K. Muller, *Fundamentals of Metal Deposition*, Elsevier Publishing Company, New York, 1967.
6. J.S. Newman, *Electrochemical Systems*, Prentice Hall, Englewood Cliffs, New Jersey, 1973.
7. S. Glasstone, *The Fundamentals of Electrochemistry and Electrodeposition*, American Electroplaters Society, New York, 2nd edition, 1960.
8. D.R. Crow, *Principles and Applications of Electrochemistry*, London, Chapman and Hall, New York, Wiley, 2nd edition,1979
9. H.R. Thirsk, and J.A. Harrison, *A Guide to the Study of Electrode Kinetics*, Academic Press, New York, 1972.
10. A.C. Beshore, B.J. Flori, G. Shade, and T.J. O'Keefe, Nucleation and growth of

zinc electrodeposited from acidic zinc solutions, *Journal of Applied Electrochemistry*, 1987,17(4), pp.765-772.

11. H. Li, F. Czerwinski and J.A. Szpunar, Monte-Carlo simulation of texture and microstructure development in nanocrystalline electrodeposition, *Nanostructured Materials*, 1997, 9(1-8), pp. 673-676.
12. S.H. Yeh and C.C. Wan, Codeposition of SiC powders with nickel in a Watts bath, *Journal of Applied Electrochemistry*, 1994, 24(10), pp. 993-1000.
13. J.P. Celis, J.R. Roos, C. Buelens, and J. Fransaer, Mechanism of electrolytic composite plating-survey and trends, *Transactions of the Institute of Metal Finishing*, 1991, 69(4), pp. 133-139.
14. C.T. Dervos, C. Kollia, S. Psarrou, P. Vassiliou, and N. Spyrellis, Electrical properties of nickel matrix composite electrocoatings, *Transactions of the Institute of Metal Finishing*, 1998, 76(4), pp. 127-130.
15. Y.M. Henuset, and R. Menini, Effect of ceramic particle pretreatment and surface chemistry on electrocomposite coatings, *Plating and Surface Finishing*, 2002, 89(9), pp. 63-67.
16. S. Shawki, and Z.A. Hamid, Deposition of high wear resistance of Ni-composite coatings, *Aircraft Engineering and Aerospace Technology*, 1997, 69(5), pp. 432-439.
17. J.R. Roos, J.P. Celis, J. Fransaer, and C. Buelens, The development of composite plating for advanced materials, *Journal of the Minerals Metals and Materials Society*, 1990, 42(11), pp. 60-63.

18. R.P. Socha, K. Laajalehto, and P. Nowak, Influence of the surface properties of silicon carbide on the process of SiC particles codeposition with nickel, *Colloids and Surfaces A: Physicochemical and Engineering Aspects*, 2002, 208(1-3), pp. 267-275.
19. J.P. Celis, and J.R. Roos, Kinetics of deposition of alumina particles from copper sulfate plating baths, *Journal of the Electrochemical Society*, 1977, 124(10), pp. 1508-1511.
20. K. Helle, and F. Walsh, Electrodeposition of composite layers consisting of inert inclusions in a metal matrix, *Transactions of the Institute of Metal Finishing*, 1997, 75(2), pp. 53-58.
21. G. Maurin, and A. Lavanant, Electrodeposition of nickel/silicon carbide composite coatings on a rotating disc electrode, *Journal of Applied Electrochemistry*, 1995, 25(12), pp. 1113-1121.
22. J.P. Celis, J.R. Roos, and C. Buelens, A mathematical model for the electrolytic codeposition of particle with a metallic matrix, *Journal of the Electrochemical Society*, 1987, 134(6), pp. 1402-1408.
23. E.C. Lee, and J.W. Choi, A study on the mechanism of formation of electrocodeposited Ni-Diamond coatings, *Surface and Coatings Technology*, 2001, 148(2-3), pp. 234-240.
24. B. Losiewicz, A. Stepien, D. Gierlotka, and A. Budniok, Composite layers in Ni-P system containing TiO_2 and PTFE, *Thin Solid Films*, 1999, 349(1-2), pp. 43-50.

25. J.L. Valdes, *Deposition of Colloidal Particles in Electrochemical Systems*, PhD thesis, Columbia University, New York, 1987.

26. J. Fransaer, J.P. Celis, and J.R. Roos, Analysis of the electrolytic codeposition of Non-brownian particles with metals, *Journal of the Electrochemical Society*, 1992, 139(2), pp. 413-425.

27. L. Orlovskaja, N. Periene, M. Kurtinaitiene, and S. Surviliene, Ni-SiC composite plated under a modulated current, *Surface and Coatings Technology*, 1999, 111(2-3), pp. 234-239.

28. Z. Gnjidic, D. Bozic, and M. Mitkov, The influence of SiC particles on the compressive properties of metal matrix composites, *Materials Characterization*, 2001, 47(2), pp. 129-138.

29. K. Kondo, A. Ohgishi, and Z. Tanaka, Electrodeposition of Zinc-SiO_2 composites, *Journal of the Electrochemical Society*, 2000, 147(7), pp. 2611-2613.

30. K.H. Hou, M.D. Ger, L.M. Wang, and S.T. Ke, The wear behaviour of electro-codeposited Ni-SiC composites, *Wear*, 2002, 253(9-10), pp. 994-1003.

31. Z. Zhu, X. Kuang, G. Carotenuto, and L. Nicolais, Fabrication and properties of carbon fiber-reinforced copper composite by controlled three-step electrodeposition, *Journal of Materials Science*, 1997, 32(4), pp. 1061-1067.

32. J.L. Stojak, and J.B. Talbot, Investigation of electrocodeposition using a rotating cylinder electrode, *Journal of the Electrochemical Society*, 1999, 146(12), pp. 4505-4513.

33. J.L. Stojak, *Investigation of Electrocodeposition Using a Rotating Cylinder Electrode*, PhD thesis, University of California, San Diego, 1997.

34. I. Garcia, A. Conde, G. Langelaan, J. Fransaer, and J.P. Celis, Improved corrosion resistance through microstructural modifications induced by codepositing SiC-particles with electrolytic nickel, *Corrosion Science*, 2003, 45(6), pp.1173-1189.

35. H. Takeuchi, Y. Tsunekawa, and M. Okumiya, Formation of compositionally graded Ni-P deposits containing SiC particles by jet electroplating, *Materials Transactions JIM*, 1997, 38(1), pp. 43-48.

36. J.W. Graydon, and D.W. Kirk, Suspension electrodeposition of phosphorus and copper, *Journal of the Electrochemical Society*, 1990, 137(7), pp. 2061-2066.

37. J. Sadowska-Mazur, M.E. Warwick, and R. Walker, Electrodeposition and properties of Tin-Nickel Silicon-Carbide composite coatings, *Transactions of the Institute of Metal Finishing*, 1986, 64(4), pp. 142-148.

38. M. Verelst, J.P. Bonino, and A. Rousset, Electroforming of metal matrix composite-dispersoid grain-size dependence of thermostructural and mechanical properties, *Materials Science and Engineering A-Structural Materials Properties Microstructure and Processing*, 1991, 135, pp. 51-57.

39. S.C. Wang, and W.C. J. Wei, Kinetics of electroplating process of nano-sized ceramic particle/Ni composite, *Materials Chemistry and Physics*, 2003, 78(3), pp. 574-580.

40. L. Benea, P.L. Bonora, A. Borello, S. Martelli, F. Wenger, P. Ponthiaux, and J.

Galland, Composite electrodeposition to obtain nanostructured coatings, *Journal of the Electrochemical Society*, 2001, 148(7), pp. C461-C465.

41. S.K. Kim, and H.J. Yoo, Formation of bilayer Ni-SiC composite coatings by electrodeposition, *Surface and Coatings Technology*, 1998, 108(1-3), pp. 564-569.
42. T. Valand, T. Burchardt, and T. Grontoft, Structure and catalytic behaviour of NiSx films with respect to the hydrogen evolution, *International Journal of Hydrogen Energy*, 2002, 27(1), pp. 39-44.
43. I. Garcia, J. Fransaer, and J.P. Celis, Electrodeposition and sliding wear resistance of nickel composite coatings containing micron and submicron SiC particles, *Surface and Coatings Technology*, 2001, 148(2-3), pp. 171-178.
44. A.F. Zimmerman, D.G. Clark, K.T. Aust, and U. Erb, Pulse electrodeposition of Ni-SiC nanocomposite, *Materials Letters*, 2002, 52(1-2), pp. 85-90.
45. D.H. Cheng, W.Y. Xu, L.Q. Hua, Z.Y. Zhang, and X.J. Wan, Electrochemical preparation and mechanical properties of amorphous nickel-SiC composites, *Plating and Surface Finishing*, 1998, 85(2), pp. 61-64.
46. N.K. Shrestha, I. Miwa, and T. Saji, Composite plating of Ni/SiC using a cationic surfactant with an azobenzene group, *Journal of the Electrochemical Society*, 2001, 148(2-3), pp. C106-C109.
47. C. Muller, M. Sarret, and M. Benballa, ZnNi/SiC composites obtained from an alkaline bath, *Surface and Coatings Technology*, 2003, 162(1), pp. 49-53.
48. A. Hovestad, and L.J.J. Janssen, Electrochemical codeposition of inert particles

in a metallic matrix, *Journal of Applied Electrochemistry*, 1995, 25(6), pp. 519-527.

49. L. Benea, P.L. Bonora, A. Borello, S. Martelli, F. Wenger, P. Poonthiaux, and J. Galland, Preparation and investigation of nanostructured SiC-nickel layers by electrodeposition, *Solid State Ionics*, 2002, 151(1-4), pp. 89-95.
50. V. Medeliene, The influence of B_4C and SiC additions on the morphological, physical, chemical and corrosion properties of Ni coatings, *Surface and Coatings Technology*, 2002, 154(1), pp. 104-111.
51. J. Li, D.L. Wang, C.S. Dai, and X.G. Hu, Microstructure characteristics of the nickel matrix in electrodeposited Ni-PSZ Gradient Coating, *Transactions of the Institute of Metal Finishing*, 1998, 76(4), pp. 131-134.
52. S.W. Watson, Electrochemical study of SiC particle occlusion during nickel electrodeposition, *Journal of the Electrochemical Society*, 1993, 140(8), pp. 2235-2238.
53. L. Benea, Electrodeposition of Zironia particles in a copper matrix, *Materials and Manufacturing Processes*, 1999, 14(2), pp. 231-242.
54. A. Grosjean, M. Rezrazi, J. Takadoum, and P. Bercot, Hardness, friction and wear characteristics of nickel-SiC electroless composite deposits, *Surface and Coatings Technology*, 2001, 137(1), pp. 92-96.
55. I. Shao, P.M. Vereecken, C.L. Chien, P.C. Searson, and R.C. Cammarata, Synthesis and characterization of particle-reinforced Ni/Al_2O_3 nanocomposites, *Journal of Materials Research*, 2002, 17(6), pp. 1412-1418.

56. P. Gyftou, M. Stroumbouli, E.A. Pavlatou, and N. Spyrellis, Electrodeposition of Ni/SiC composites by pulse electrolysis, *Transactions of the Institute of Metal Finishing*, 2000, 80(3), pp. 88-91.

57. L. Benea, P.L. Bonora, A. Borello, and S. Martelli, Wear corrosion properties of nano-structured SiC-nickel composite coatings obtained by electroplating, *Wear*, 2001, 249(10-11), pp. 995-1003.

58. D. Koleva, N. Boshkov, G. Raichevski, and L. Veleva, Electrochemical corrosion behaviour and surface morphology of electrodeposited zinc, zinc-cobalt and their composite coatings, *Transactions of the Institute of Metal Finishing*, 2005, 83(4), pp. 188-193.

59. Y.Z Wan, Y.L. Wang, H.M. Tao, G.X Cheng, and X.H. Dong, Preparation and characterization of Cu-$MoSi_2$ composite coatings, *Transactions of the Institute of Metal Finishing*, 1999, 77(1), pp. 52-54.

60. B. Bozzini, G. Giovannelli, and P.L. Cavallotti, An investigation into the electrodeposition of Au-Cu-matrix particulate composites, *Journal of Applied Electrochemistry*, 1999, 29(6), pp. 685-692.

61. M.E. Bahrololoom, and R. Sani, The influence of pulse plating parameters on the hardness and wear resistance of nickel-alumina composite coatings, *Surface and Coatings Technology*, 2005, 192(2-3), pp. 154-163.

62. Y.D. Gamburg, M.Y. Grosheva, S. Biallozor, and M. Hass, The electrochemical deposition of nickel from electrolytes containing malonic acid, *Surface and Coatings Technology*, 2002, 150(1), pp. 95-100.

63. V.B. Singh, and R.S. Sarabi, Hardness and structure of electrodeposited nickel from a nickel sulfamate-formamide bath, *Plating and Surface Finishing*, 1996, 83(10), pp. 54-57.

64. N.S. Qu, D. Zhu, K.C. Chan, and W.N. Lei, Pulse electrodeposition of nanocrystalline nickels using ultra narrow pulse width and high peak current density, *Surface and Coatings Technology*, 2003, 168(2-3), pp. 123-128.

65. Y. Tsuru, M. Nomura, and F.R. Foulkes, Effects of boric acid on hydrogen evolution and internal stress in films deposited from a nickel sulfamate bath, *Journal of Applied Electrochemistry*, 2002, 32(6), pp. 629-634.

66. J.K. Dennis, and T.E. Such, *Nickel and Chromium Plating*, Butterworths, London, 2nd edition, 1986.

67. C.H. Huang, Hydrolysis of sulfamate ion in nickel sulfamate solution, *Plating and Surface Finishing*, 1994, 81(9), pp. 64-68.

68. Y. Tsuru, M. Nomura, and F.R. Foulkes, Effects of chloride, bromide and iodide ions on internal stress in films deposited during high speed nickel electroplating from a nickel sulfamate bath, *Journal of Applied Electrochemistry*, 2000, 30(2), pp. 231-238.

69. N.V. Myung, and K. Nobe, Electrodeposition of Ni/Cu multilayers, *Plating and Surface Finishing*, 2000, 87(6), pp.125-134.

70. R.A. Tacken, P. Jiskoot, and L.J.J. Janssen, Effect of magnetic charging of Ni on electrolytic codeposition of Zn with Ni particles, *Journal of Applied Electrochemistry*, 1996, 26, pp. 129-134.

71. A. Grosjean, M. Rezrazi, and M. Tachez, Study of the surface charge of silicon carbide (SiC) particles for electroless composite deposits, *Surface and Coatings Technology*, 1997, 96(2-3), pp. 300-304.

72. N.K. Shrestha, M. Masuko, and T. Saji, Composite plating of Ni/SiC using azo-cationic surfactants and wear resistance of coatings, *Wear*, 2003, 254(5-6), pp. 555-564.

73. L. Orlovskaja, N. Periene, M. Kurtinaitiene, and G. Bikulcius, Electrocomposites with SiC content modulated in layers, *Surface and Coatings Technology*, 1998, 105(1-2), pp. 8-12.

74. B. Bozzini, G. Giovannelli and P.L. Cavallotti, An investigation into the electrodeposition of AuCu-matrix particulate composites. Part 2: Baths not containing free cyanide, *Journal of Applied Electrochemistry*, 2000, 30(5), pp. 591-594.

75. A. Kentepozidou, C. Kiparissides, F. Kotzia, and C. Kollia, Nickel/microcapsules composite electrocoatings: the synthesis of water-containing microcapsules and preparation of the coatings, *Journal of Materials Science*, 1996, 31(5), pp. 1175-1181.

76. S.C. Wang and W.C. J. Wei, Electrokinetic properties of nanosized SiC particles in highly concentrated electrolyte solutions, *Journal of the American Ceramic Society*, 2001, 84(7), pp. 1411-1414.

77. A. Grosjean, M. Rezrazi, and P. Bercot, Some morphological characteristics of the incorporation of silicon carbide (SiC) particles into electroless nickel deposits,

Surface and Coatings Technology, 2000, 130(2-3), pp. 252-256.

78. A. Hovestad, R.J.C.H.L. Heesen, and L.J.J. Janssen, Electrochemical deposition of zinc-polystyrene composites in the presence of surfactants, *Journal of Applied Electrochemistry*, 1999, 29(3), pp. 331-338.
79. F. Ebrahimi, G.R. Bourne, M.S. Kelly, and T.E. Matthews, Mechanical properties of nanocrystalline nickel produced by electrodeposition, *Nanostructured Materials*, 1999, 11(3), pp. 343-350
80. A.M. ElSherik, U. Erb, and J. Page, Microstructural evolution in pulse plated nickel eletrodeposits, *Surface and Coatings Technology*, 1996, 88(1-3), pp. 70-78.
81. J.J. Kelly, P.E. Bradley, and D. Landolt, Additive effects during pulsed deposition of Cu-Co Nanostructures, *Journal of the Electrochemical Society*, 2000, 147(8), pp. 2975-2980.
82. D. Mockute, G. Bernotiene, and R. Butkiene, The effect of electrolytes composition on behaviour of saccharin and N-methyl saccharin during Ni electrodeposition, *Transactions of the Institute of Metal Finishing*, 2002, 80(4), pp. 120-123.
83. N.M. Martyak, Grain refinement in electrogalvanized coatings, *Materials Characterization*, 2003, 50(4-5), pp. 269-274.
84. D.H. Jeong, F. Gonzalez, G. Palumbo, K.T. Aust, and U. Erb, The effect of grain size on the wear properties of electrodeposited nanocrytalline nickel coatings, *Scripta Materialia*, 2001, 44(3), pp. 493-499.

85. L. Burzynska, and E. Rudnik, The influence of saccharin and sodium lauryl sulfate on the electrodeposition process of Co-Ni alloys, *Archives of Metallurgy*, 2000, 45(3), pp. 276-285.

86. F. Lallemand, L. Ricq, P. Bercot, and J. Pagetti, Effects of the structure of organic additives in the electrochemical preparation and characterization of CoFe film, *Electrochimica Acta*, 2002, 47(26), pp. 4149-4156.

87. N.V. Mandich, and D.W. Baudrand, Troubleshooting electroplating installations: nickel sulfamate plating systems, *Plating and Surface Finishing*, 2002, 89(9), pp. 68-76.

88. S.D. Leith, S. Ramli, and D.T. Schwartz, Characterization of NixFe1-x(0.01<x<0.95) electrodeposition from a family of sulfamate chloride electrolytes, *Journal of the Electrochemical Society*, 1999, 146(4), pp. 1431-1435.

89. M. Paunovic, P.J. Bailey, P.G. Schad, and D.A. Smith, Electrochemically deposited diffusion-barriers, *Journal of the Electrochemical Society*, 1994, 141(7), pp. 1843-1850.

90. N.L. Burns, J.C. Clunie, and J.K. Baira, Diaphragm cell determination of the interdiffusion coefficients for aqueous-solutions of copper-sulfate, cobalt sulfate, and nickel sulfamate, *Journal of Physical Chemistry*, 1991, 95(9), pp. 3801-3804.

91. T.W. Tomaszewski, L.C. Tomaszewski, and H. Brown, Codeposition of finely dispersed particles with metals, *Plating*, 1969, 56, pp.1234-1239.

92. C.C. Lee, and C.C. Wan, A study of composite electrodeposition of copper with alumina powder, *Journal of the Electrochemical Society*, 1988, 135(8), pp. 1930-1933.

93. J.W. Dini, and H.R. Johnson, The influence of nickel sulfamate operating parameters on the impurity content and properties of electrodeposits, *Thin Solid Films*, 1978, 54(2), pp. 183-188.

94. W. Paatsch, Morphology and permeability of nickel electrodeposits, *Plating and Surface Finishing*, 1988, 75(8), pp. 52-55.

95. C.S. Lin, P.C. Hsu, K.C. Peng, L.W. Chang, and C.H. Chen, Annealing behavior of nickel electrodeposited from sulfamate bath at different temperatures, *Materials Transactions JIM*, 2001, 42(2), pp. 316-322.

96. C.S. Lin, K.C. Peng, P.C. Hsu, L.W. Chang, and C.H. Chen, Effect of bath temperature on microstructure of sulfamate nickel electrodeposits, *Materials Transactions JIM*, 2000, 41(7), pp. 777-782.

97. M. Verelst, J. P. Bonino, M. Brieu, and A. Rousset, Thermomechanical properties of Ni-Al_2O_3 metal matrix composites produced by electroforming, *Materials Science and Engineering A-Structural Materials Properties Microstructure and Processing*, 1995, 191(1-2), pp. 165-169.

98. M. Ghouse, Influence of heat treatment on the bond strength of codeposited Ni-SiC composite coatings, *Surface Technology*, 1984, 21(2), pp. 193-200.

99. J. Li, Y.Y. Wu, D.L. Wang, and X.G. Hu, The microstructure and wear resistance characteristics of electroformed nickel and partially stabilized zirconia

composite coatings, *Journal of Materials Science*, 2000, 35(7), pp. 1751-1758.

100. M. Nishira, and O. Takano, Friction and wear characteristics of electroless Ni-P-PTFE composite coatings, *Plating and Surface Finishing*, 1994, 81(1), pp. 48-50.
101. M. Ghouse, Wear Characteristics of sediment co-deposited nickel-SiC composite coatings, *Metal Finishing*, 1984, 82(3), pp. 33-37.
102. L. Robert, S. Basrour, M. Wery, and F. Sittler, The morphology and electrochemical behavior of electrodeposited Nickel onto metallized silicon, *Plating and Surface Finishing*, 2000, 87(5), pp. 153-159.
103. C.C. Hu, and C.M. Wu, Effects of deposition modes on the microstructure of copper deposits from an acidic sulfate bath, *Surface and Coatings Technology*, 2003, 176(1), pp. 75-83.
104. K. Yukimura, and T. Muraho, A two-switch mode pulse modulator for plasma-based ion implantation and deposition, *Nuclear Instruments and Methods in Physics Research B*, 2003, 206, pp. 791-793.
105. T. Szczurek, T. Rausch, M. Schlesinger, D.D. Snyder, and C.H. Olk, Induced crystallographic Orientations in electrodeposited Ni-Cu multilayers, *Journal of the Electrochemical Society*, 1999, 146(5), pp. 1777-1779.
106. X.Y. Wang, and D.Y. Li, Mechanical and electrochemical behavior of nanocrystalline surface of 304 stainless steel, *Electrochimica Acta*, 2002, 47(24), pp. 3939-3947.
107. S. Shriram, S. Mohan, N.G. Renganathan, and R. Venkatachalam,

Electrodeposition of nanocrystalline nickel- a brief review, T*ransactions of the Institute of Metal Finishing*, 2000, 78(5), pp. 194-197.

108. K. Saber, C.C. Koch, and P.S. Fedkiw, Pulse current electrodeposition of nanocrystalline zinc, *Materials Science and Engineering A-Structural Materials Properties Microstructure and Processing*, 2003, 341(1-2), pp. 174-181
109. D.K. Sarkar, X.J. Zhou, A. Tannous, and K.T. Leung, Growth mechanisms of copper nanocrystals on thin polypyrrole films by electrochemistry, *Journal of Physical Chemistry B*, 2003, 107(13), pp. 2879-2881.
110. S.C. Wang, and W.C.J. Wei, Characterization of electroplated Ni/SiC and Ni/Al2O3 composite coatings bearing nanoparticles, *Journal of Materials Research*, 2003, 18(7), pp. 1566-1574.
111. J.C. Puippe, “Pulse Plating versus DC Plating” in J.C. Puippe and F. Leaman eds., *Theory and Practice of Pulse Plating*, American Electroplaters and Surface Finishers Society, Orlando, Florida, pp. 531-554, 1986.
112. K.I. Popov, D.C. Totovski and M.D. Maksimovic, Fundamental aspects of pulsating current metal electrodeposition, *Surface Technology*, 1993, 19(2), pp. 181-185.
113. A.B. Vidrine, and E.J. Podlaha, Composite electrodeposition of ultrafine r-alumina particles in nickel matrices Part 1: Citrate and chloride electrolytes, *Journal of Applied Electrochemistry*, 2001, 31(4), pp. 461-468.
114. K.I. Popov, M.D. Maksimovic, and M.S. Simic, The effect of periodic reverse current on the surface roughness of metal deposits and the maximal deposition

rate periodic reverse current on the surface roughness of metal deposits and the maximal deposition rate, *Surface Technology*, 1982, 16(3), pp. 209-218.

115. F.Z. Yang, S.K. Xu, L. Huang, X. Zhang, and S. Zhou, A study on the effect of bath composition on the internal stress of a palladium electrodeposit, *Transactions of the Institute of Metal Finishing*, 1998, 76(6), pp. 238-240.
116. C. Kollia, and N. Spyrellis, Microhardness and rouoghness in nickel electrodeposition under pulse reverse current conditions, *Surface and Coatings Technology*, 1993, 58(2), pp. 101-105.
117. C. Kollia, and N. Spyrellis, Textural modification in nickel electrodeposition under pulse reversed current, *Surface and Coatings Technology*, 1993, 57(1), pp. 71-75.
118. M. Ghaemi, and L. Binder, Effects of direct and pulse current on electrodeposition of manganese dioxide, *Journal of Power Source*, 2002, 111(2), pp. 248-254.
119. R.T.C. Choo, J.M Toguri, A.M. El-Sherik, and U. Erb, Mass transfer and electrocrystallization analyses of nanocrystalline nickel production by pulse plating, *Journal of Applied Electrochemistry*, 1995, 25(4), pp. 384-403.
120. N.R.K. Vilambi, and D.T. Chin, Selective pulse plating from an acid copper-sulfate bath, *Plating and Surface Finishing*, 1988, 75(1), pp. 67-73.
121. K.R. Murali, and V. Swaminathan, Effect of pulse reversal on the properties of pulse plated CdSexTe1-x thin films, *Journal of Applied Electrochemistry*, 2002, 32(10), pp. 1151-1156.

122. E. BeltowskaLehman, P. Ozga, and E. Chassaing, Pulse electrodepositionof Ni-Cu-Mo alloys, *Surface and Coatings Technology*, 1996, 78(1-3), pp. 233-237.

123. H. Ashassi-Sorkhabi, A. Hagrah, N. Parvini-Ahmadi, and J. Manzoori, Zinc-nickel alloy coatings electrodeposited from a chloride bath using direct and pulse current, *Surface and Coatings Technology*, 2001,140(3), pp. 278-283.

124. A. Marlot, P. Kern, and D. Landolt, Pulse plating of Ni-Mo alloys from Ni-rich electrolytes, *Electrochimica Acta*, 2002, 48(1), pp. 29-36.

125. T. Nakanishi, M. Ozaki, H.S. Nam, T. Yokoshima, and T. Osaka, Pulsed electrodeposition of nanocrystalline CoNiFe soft magnetic thin films, *Journal of the Electrochemical Society*, 2001, 148 (9), pp. C627-C631.

126. K. R. Murali, V. Swaminathan, and D.C. Trivedi, Characteristics of nanocrystalline CdSe films, *Solar Energy Materials and Solar Cells*, 2004, 81(1), pp. 113-118.

127. S.M. Delphine, M. Jayachandran, and C. Sanjeeviraja, Pulse electrodeposition and characterisation of tungsten diselenide thin films, *Materials Chemistry and Physics*, 2003, 81, pp. 78-83.

128. F.Y. Ge, S.K. Xu, S.B. Yao, and S.M. Zhou, Study of the structures of pulse plating Zn-Fe deposits, *Surface and Coatings Technology*, 1997, 88(1-3), pp. 1-4

129. C.F. Chen, and K.C. Lin, Effect of pulse frequency on leveling and resistivity of copper coatings, *Japanese Journal of Applied Physics*, 2002, 41, pp. 2881-2885.

130. S.C. Chang, J.M. Shieh, B.T. Dai, and M.S. Feng, Investigations of pulse current electrodeposition for damasence copper metals, *Journal of Vacuum Science and*

Technology B, 2002, 20(6), pp. 2295-2298.

131. C. Muller, M. Sarret, and T. Andreu, Electrodeposition of ZnMn alloys using pulse plating, *Journal of the Electrochemical Society*, 2003, 150(11), pp. C772-C776.
132. B. Dacuna, J. Mira, M.C. Blanco, M.A. Lopez-Quintela, and J. Rivas, Preparation of CoAg electrodeposited films, *Journal of Magnetism and Magnetic Materials*, Sp. Iss., 1999, 203, pp. 123-125.
133. J.C. Puippe, and N. Ibl, Influence of charge and discharge of electric double layer in pulse plating, *Journal of Applied Electrochemistry*, 1980, 10(6), pp. 775-785.
134. N. Ibl, Some theoretical aspects of pulse electrolysis, *Surface Technology*, 1980, 10(2), pp. 81-104.
135. D.D. Shivagan, P.M. Shirage, N.V. Desai, L.A. Ekal, and S.H. Pawar, Studies on pulse electrodeposition of high T_c superconducting Hg-1212 thin films, *Materials Research Bulletin*, 2001, 36(3-4), pp. 607-615.
136. E. Chassaing, M. Joussellin, and R. Wiart, The kinetics of nickel electrodeposition- inhibition by adsorbed hydrogen and anions, *Journal of Electroanalytical Chemistry*, 1983, 157(1), pp. 75-88.
137. I. Epelboin, M. Joussellin, and R. Wiart, Impedance measurements for nickel deposition in sulfate and chloride electrolytes, *Journal of Electroanalytical Chemistry*, 1981, 119(1), pp. 61-71.
138. J.C. Puippe, “Qualitative Approach to Pulse Plating” in J.C. Puippe and F. Leaman eds., *Theory and Practice of Pulse Plating*, American Electroplaters and

Surface Finishers Society, Orlando, Florida, pp.1-15, 1986.

139. K.P. Wong, *Shaped Pulse Electroforming of Nickel*, PhD thesis, The Hong Kong Polytechnic University, 2002.

140. K.P. Wong, K.C. Chan, and T.M Yue, Influence of spike current in different shaped waveforms on the surface finish of nickel electroforms, *Surface and Coatings Technology*, 2001, 140(3), pp. 284-292.

141. K.P. Wong, K.C. Chan, and T.M. Yue. A study of surface finishing in pulse current electroforming of nickel by utilizing different shaped waveforms, *Surface and Coatings Technology*, 1999, 115(2-3), pp. 132-139.

142. K.P. Wong, K.C. Chan, and T.M. Yue, Modeling the effect of complex waveform on surface finishing in pulse current electroforming of nickel, *Surface and Coatings Technology*, 2000, 135(1), pp. 91-97.

143. K.P. Wong, K.C. Chan, and T.M. Yue, Influence of spike current in different shaped waveforms on the hardness and grain size of nickel electroforms, *Journal of Materials Processing Technology*, 2001, 117(1-2), pp. 97-104.

144. K.P. Wong, K.C. Chan, and T.M. Yue, Modeling of elecrocrystallization for pulse current electroforming of nickel, *Applied Surface Science*, 2001, 178(1-4), pp. 178-189.

145. K.P. Wong, K.C. Chan, and T.M. Yue, A study of hardness and grain size in pulse current electroforming of nickel using different shaped waveforms, *Journal of Applied Electrochemistry*, 2001, 31(1), pp. 25-34.

146. A. Chiba, T. Ogawa, and T. Yamashita, Magnetic field effects on the

electrodeposition of copper from copper sulphate in sulphuric acid, *Surface and Coatings Technology*, 1988, 34(4), pp. 455-462.

147. N. D. Nikolic, H. Wang, H. Cheng, C.A. Guerrero, and N. Garcia, Influence of the magnetic field and magnetoresistance on the electrodeposition of Ni nanocontacts in thin films and microwires, *Journal of Magnetism and Magnetic Materials*, 2004, 272(3), pp. 2436-2438.
148. X.P. Li, Z.J. Zhao, H.L. Seet, W.M. Heng, T.B. Oh, and J.Y. Lee, Magnetically controlled electroplating of NiFe/Cu composite wires, *Electrochemical and Solid State Letters*, 2004, 7(1), pp. C1-C3.
149. Z.H. Gu, and T.Z. Fahidy, On the effect of a horizontal magnetic field on the electrolytic deposition of thin Fe-Ni films. *Journal of Physics D-Applied Physics*, 2000, 33(19), pp. L113-L114.
150. A. Chiba, K. Kitamura and T. Ogawa, Magnetic field effects on the electrodeposition of nickel from a high pH watt’s bath, *Surface and Coatings Technology*, 1986, 27(1), pp. 83-88.
151. S. Mohanta, and T.Z. Fahidy, Effect of a uniform magnetic-field on mass-transfer in electrolysis, *Canadian Journal of Chemical Engineering*, 1972, 50(2), pp. 248-252.
152. K. Msellak, J.P. Chopart, O. Jbara, O. Aaboubi, and J. Amblard, Magnetic field effects on Ni-Fe alloys codeposition, *Journal of Magnetism and Magnetic Materials*, 2004, 281(2-3), pp.295-304
153. A.L. Danilyuk V.I. Kurmashev, and A.L. Matyushkov, Magnetostatic field

influence on electrodeposition of metal films, *Thin Solid Films*, 1990, 189(2), pp. 247-255.

154. P. Fricoteaux, A. Olivier, and R. Delmas, Study of the exchange current at the Cu^+/Cu interface by radiotracer: magnetic field effect, *Journal of the Electrochemical Society*, 1992, 139(4), pp. 1096-1099.
155. O. Devos, A. Olivier, J.P. Chopart, O. Aaboubi, and G. Maurin, Magnetic field effects on nickel electrodeposition, *Journal of the Electrochemical Society*, 1998, 145(2), pp. 4135-4139.
156. E. Brillas, J. Rambla, and J. Casado, Nickel electrowinning using a Pt catalysed hydrogen-diffusion anode, *Journal of Applied Electrochemistry*, 1999, 29(12), pp. 1367-1376.
157. L. Yang, Anodic behavior of aluminum and its alloys in sulfuric acid, *Journal of the Electrochemical Society*, 1954, 101, pp. 456-461.
158. O. Devos, A. Olivier, J.P. Chopart, O. Aaboubi, and G. Maurin, Magnetic field effects on nickel electrodeposition, *Journal of the Electrochemical Society*, 1998, 145(2), pp. 401-405.
159. O. Aaboubi, J. Amblard, J.P. Chopart, and A. Olivier, Magnetohydrodynamic analysis of silver electrocrystallization from a nitric and tartatic solution, *Journal of the Electrochemical Society*, 2004, 151(2), pp. C112-C118.
160. H. Matsushima, T. Nohira, I. Mogi, and Y. Ito, Effects of magnetic fields on iron electrodepositon, *Surface and Coatings Technology*, 2004, 179(2-3), pp.245-251.
161. H. Matsushima, T. Nohira, and Y. Ito, Improved deuterium separation factor for

the iron electrode prepared in a magnetic field, *Electrochimica Acta*, 2004, 49(24), pp. 4181-4187.

162. O. Devos, O. Aaboubi, J.P. Chopart, E. Merienne, A. Olivier, C. Gabrielli, and B. Tribollet, EIS investigation of zinc electrodeposition in basic media at low mass transfer rates induced by a magnetic field, *Journal of Physical Chemistry B*, 1999, 103(3), pp. 496-501.
163. N.D. Nikolic, H. Wang, H. Cheng, C. Cuerrero, E.V. Ponizovskaya, G.H. Pan, and N. Garcia, Magneroresistance controls of arborous bead-dendritic growth of magnetic electrodeposits, *Journal of the Electrochemical Society*, 2004, 151(9), pp. C577-C584.
164. S. Bodea, R. Ballou, and P. Molho, Electrochemical growth of iron and cobalt arborescences under a magnetic field, *Physical Review E*, 2004, 69(2), pp. No. 021605.
165. R.A. Tacken, and L.J.J. Janssen, Applications of magnetoelectrolysis, *Journal of Applied Electrochemistry*, 1995, 25(1), pp. 1-5.
166. S. Legeai, M. Chatelut, O. Vittori, J. P. Chopart, and O. Aaboubi, Magnetic field in influence on mass transport phenomena, *Electrochimica Acta*, 2004, 50(1), pp. 51-57.
167. E.J. Kelly, Magnetic field effects on electrochemical reactions occurring at metal/flowing-electrolyte interfaces, *Journal of the Electrochemical Society*, 1977, 124 (7), pp. 987-994.
168. G. Hinds, J.M.D. Coey, and M.E.G. Lyons, Influence of magnetic forces on

electrochemical mass transport, *Electrochemistry Communications*, 2001, 3(5), pp.215-218.

169. P. Nowak, R.P. Socha, M. Kaisheva, J. Fransaer, J.P. Celis, and Z. Stoinov, Electrochemical investigation of the codeposition of SiC and SiO_2 particles with nickel, *Journal of Applied Electrochemistry,* 2000, 30(4), pp. 429-437.
170. S.W. Banovic, K. Barmak, and A.R. Marder, Characterization of single and discretely-stepped electro-composite coatings of nickel-alumina, *Journal of Materials Science*, 1999, 34(13), pp. 3203-3211.
171. J. Steinbach, and H. Ferkel, Nanostructured Ni-Al_2O_3 films prepared by DC and pulsed DC electroplating, *Scripta Materialia*, 2001, 44(8-9), pp. 1813-1816.
172. A.F. Zimmerman, G. Palumbo, K.T. Aust, and U. Erb, Mechanical properties of nickel silicon carbide nanocomposites, *Materials Science and Engineering A-Structural Materials Properties Microstructure and Processing*, 2002, 328(1-2), pp. 137-146.
173. N. Guglielmi, Kinetics of the deposition of inert particles from electrolytic baths, *Journal of the Electrochemical Society*, 1972, 119(8), pp. 1009–1012
174. J.C. Puippe, and F. Leaman, *Theory and Practice of Pulse Plating*, American Electroplaters and Surface Finishers Society, Orlando, Florida, 1986.
175. K.C. Chan, N.S. Qu, and D. Zhu, Fabrication of graded nickel-quasicrytal composite by electrodeposition, *Transactions of the Institute of Metal Finishing*, 2002, 80(6), pp. 210-213.
176. W.L. Dan, and J.S. Liu, Theoretical analysis of the influence of pulse

energization parameters on collecting efficiency, *Journal of Southern Institute Metallurgy*, 1996, 17, pp. 71-80 (in Chinese).

177. W.C. Tsai, C.C. Wan, and Y.Y. Wang, Mechanism of copper electrodeposition by pulse current and its relation to current efficiency, *Journal of Applied Electrochemistry*, 2002, 32(12), pp. 1371-1378.
178. S.A. Watson, and A.C. Hart, Electoforming-a largely unrecognized but expanding vital industry, *Transactions of the Institute of Metal Finishing*, 1997, 75(4), pp. 84-88.
179. S.W. Watson, and P.R. Walters, The effect of chromium particles on nickel electrodeposition, *Journal of the Electrochemical Society*, 1991, 138(12), pp. 3633-3637.
180. S.H. Yeh, and C.C. Wan, A study of SiC/Ni composite plating in the Watts bath, *Plating and Surface Finishing*, 1997, 84(3), pp. 54-58.
181. R.P. Socha, P. Nowak, K. Laajalehto, and J. Vayrynen, Particle-electrode surface interaction during nickel electrodeposition from suspensions containing SiC and SiO_2 particles, *Colloids and Surfaces A-Physicochemical and Engineering Aspects*, 2004, 235(1-3), pp. 45-55.
182. R.P. Socha, K. Laajalehto, and P. Nowak, Oxidation of silicon carbide surface in Watts' plating bath, *Surface and Interface Analysis*, 2002, 34(1), pp. 413-417.
183. D.R. Franceschetti, and J.R. Macdonald, Electrode-kinetics, equivalent-circuits, and system characterization-small-single conditions, *Journal of Electroanalytical Chemistry*, 1977, 82(1-2), pp. 271-301.

184. J.R. Macdonald, *Impedance Spectroscopy: Emphasizing Solid Materials and Systems*, New York, Wiley, 1987.

185. D.T. Chin, and D. Balamurugan, An experimental study on metal distribution in pulse plating, *Electrochimica Acta*, 1992, 37(11), pp. 1927-1934.

186. G. Holmbom, and B.E. Jacobson, Nucleation and initial growth of pulse-plated gold on crystalline and amorphous substrates, *Journal of the Electrochemical Society*, 1988, 135(11), pp. 2720-2725.

187. L.E. Fratila-Apachitei, J. Duszczyk, and L. Katgerman, AlSi(Cu) anodic oxide layers formed in H_2SO_4 at low temperature using different current waveforms, *Surface and Coatings Technology*, 2003, 165(3), pp. 232-240..

188. W.C. Tsai, C.C. Wan, and Y.Y. Wang, Frequency effect of pulse plating on the uniformity of copper deposition in plated through holes, J*ournal of the Electrochemical Society*, 2003, 150(5), pp. C267-C272.

189. W.H. Lee, S.C. Tang, and K.C. Chung, Effects of direct current and pulse-plating on the co-deposition of nickel and nanometer diamond powder, *Surface and Coatings Technology*, 1999, 121, pp. 607-611.

190. Y. Liu, and M. Pritzker, Effect of pulse plating on composition of Sn-Pb coatings deposited in fluoroborate solutions, *Journal of Applied Electrochemistry*, 2003, 33(12), pp. 1143-1153.

191. K. Lu, X.D. Liu, and Z.Q. Hu, The Hall-Petch relation in nanocrystalline materials, *Chinese Journal of Materials Research*, 1994, 8(5), pp. 385-391 (in Chinese).

192. W.C. Oliver, and G.M. Pharr, An improved technique for determining hardness and elastic modulus using load and displacement sensing indentation experiments, *Journal of Materials Research*, 1992, 7(6), pp. 1564-1583.

193. R.C. Cammarata, T.E. Schlesinger, C. Kim, S.B. Qadri, and A.S. Edelstein, Nanoindentation study of the mechanical properties of copper-nickel multilayered thin films, *Applied Physics Letters*, 1990, 56(19), pp. 1862-1864.

194. Y.M. Yeh, G.C. Tu, and T.H. Fang, Nanomechanical properties of nanocrystalline Ni-Fe mold insert, *Journal of Alloys and Compounds*, 2004, 372(1-2), pp. 224-230.

195. A. Chiba, T. Niimi, H. Kitayama, and T. Ogawa, Inhibition by magnetic fields of the growth of zinc dendrites from alkaline zincate baths, *Surface and Coatings Technology*, 1986, 29(4), pp. 347-355.

196. S.N. Vinogradov, G.N. Maltseva, and N.A. Gulyaeva, Electrodeposition of a Palladium-Copper alloy in non-steady-state electrolysis, *Russian Journal of Electrochemistry*, 2001, 37(7), pp. 715-717.

197. T.Z. Fahidy, Reviews of applied electrochemistry. 8. Magnetoelectrolysis, *Journal of Applied Electrochemistry*, 1983, 13(5), pp. 553-563.

198. O. Aaboubi, J.P. Chopart, J. Douglade, A. Olivier, C. Gabrielli, and B. Tribollet, Magnetic field effects on mass transport, *Journal of the Electrochemical Society*, 1990, 137(6), pp. 1796-1804.

199. O. Wassef, and T.Z. Fahidy, Magnetoelectrolysis in the presence of bubble formation at the cathode, *Electrochimica Acta*, 1976, 21(10), pp. 727-730.

200. T.Z. Fahidy, Characteristics of surfaces produced via magnetoelectrolytic deposition, *Progress in Surface Science*, 2001, 68(4-6), pp. 155-188.
201. J.P. Chopart, J. Douglade, P. Fricoteaux, and A. Olivier, Electrodeposition and electrodissolution of copper with a magnetic field: dynamic and stationary invertigations, *Electrochimica Acta*, 1991, 36(3-4), pp. 459-463.
202. H. Matsushima, T. Nohira, and Y.Ito, Magnetic field effects on the crystal orientation and surface morphology of electrodeposited iron films, *Journal of Solid State Eletrochemistry*, 2004, 8(3), pp.195-200.
203. C. O’Reilly, G.. Hinds, and J.M.D. Coey, Effect of a magnetic field on electrodeposition chronoamperometry of Ag, Cu, Zn, and Bi, *Journal of the Electrochemical Society*, 2001, 148(10), pp. C674-C678.
204. G. Hinds, F.E. Spada, and J.M.D. Coey, T.R. Ni Mhiochain, and M.E.G. Lyons, Magnetic field effects on copper electrolysis, *Journal of Physical Chemistry B*, 2001, 105(39), pp. 9487-9502.
205. K.C. Chan, N.S. Qu, and D. Zhu, Quantitative texture analysis in pulse reverse current electroforming of nickel, *Surface and Coatings Technology*, 1998, 99(1-2), pp.69-73.